Manipulating light and matter with photonic structures:
Numerical investigations on photonic crystals and optical forces

by

Peng Zhang

A dissertation submitted to the graduate faculty

in partial fulfillment of the requirements for the degree of

DOCTOR OF PHILOSOPHY

Major: Condensed Matter Physics

Program of Study Committee:
Costas M. Soukoulis, Major Professor
James Vary
Jigang Wang
Jiming Song
Kai-Ming Ho
Thomas Koschny

The student author, whose presentation of the scholarship herein was approved by the program of study committee, is solely responsible for the content of this dissertation. The Graduate College will ensure this dissertation is globally accessible and will not permit alterations after a degree is conferred.

Iowa State University

Ames, Iowa

2017

DEDICATION

To my dear parents.

TABLE OF CONTENTS

LIST OF TABLES

LIST OF FIGURES

ACKNOWLEDGEMENTS

I would like to express my sincere gratitude to all those who have been supporting me during the past six years. This thesis cannot be completed without their help.

First and foremost, I would like to express my special thanks to my advisor, Dr. Costas Soukoulis, not only for his insight of physics to keep us on the most interesting topics and frontiers of research, but also the unlimited freedom he gives us to pursue whatever we want to do. His guidance, his patience, his encouragement and support have ensured the completion of my whole PhD life.

I would like to thank Dr. Thomas Koschny for providing great guidance during my research. He is the most knowledgeable person, and his desire to make everything perfect, his principle of always starting from the simple has and will benefit me all the time.

I would like to thank my committee: Dr. James Vary, Dr. Jigang Wang, Dr. Jiming Song, and Dr. Kai-Ming Ho. I really appreciate their time and help all throughout my PhD life. Without them, I cannot finish this work.

I would like to express my gratitude for all the other group members, the past and the present: Dr. Nianhai Shen, Dr. Lei Zhang, Dr. Babak Dastmalchi, Dr. Aditya Jain, Dr. Philippe Tassin, Dr. Chris Fietz, Dr. Ming Fang, Dr. Qian Zhao, Dr. Yuancheng Fan, Dr. Hao Zhang, Dr. Wenyao Liang, Dr. Yihang Chen, Dr. Yihao Yang, Dr. Weina Cui. All of them help me a lot and working with them in the same group is a great joy. I would also like to thank my friends, Dr. Junlong Kou, Dr. Daixiang Mou, Dr. Li Cheng, Dr. Yun Wu, Dr. Yang Sun, and Dr. Chen Liu. Though we are not working on the same topic, frequent fruitful discussion with them have opened my eyes and enlightened my passion for science all the time.

Last but not least, I want to thank my parents, for their unconditional love will always drive me forward.

ABSTRACT

The highly developed nano-fabrication techniques allow light to be modulated with photonic structures in a more intensive way. These photonic structures involve photonic crystals, metals supporting surface plasmon polaritons, metamaterials, etc. In this thesis work, three different ways for light manipulation are numerically investigated. First, the light propagation is modulated using a photonic crystal with Dirac cones. It is demonstrated that the zero-index behavior of this photonic crystal which happens for normal incident waves, is lost at oblique incidence. A new method combining complex-k band calculations and absorbing boundary conditions for Bloch modes is developed to analyze the Bloch mode interaction in details. Second, the mechanic states of graphene are modulated through the optical gradient force. This force is induced by the coupled surface plasmons on the double graphene sheets and is greatly enhanced in comparison to the regular waveguides. By applying different strengths of forces in accordance to the input power, the mechanic state transition is made possible, accompanied by an abrupt change in the transmission and reflection spectra. Third, the helicity/chirality of light is studied to modulate the lateral force on a small particle. A left-hand material slab which supports coherent TE ad TM plasmons simultaneously is introduced. By mixing the TE and TM surface plasmons with different relative phases, the lateral force on a chiral particle can be changed, which will be beneficial for chiral particle sorting.

CHAPTER 1. INTRODUCTION

1.1 Concepts and a historical survey of manipulating light

Light is a gift from nature. It shines the darkness in the old days, and is used to transport information nowadays. It travels fast as its speed in the free space reaches approximately 3×10^8 m/s, which is considered the upper limit of all objects under current theoretical frames. A true understanding of light takes a long history tracing back to thousand years ago when the ancient people first made fires to lighten up their surroundings, while from the modern view, it is interpreted as the incoherent radiation from spontaneous emission of atoms. Newton and Hygens are the two giants who made great steps by revealing a lot of intrinsic properties of light, such as dispersion, interference and so on. Their completely opposite opinions of interpreting light as "particles" or "waves" brought the academia into centuries' debate. After summarizing the brilliant work by Ampire, Hertz, Faraday and other scientists, Maxwell raised a set of partial differential equations, now well known as Maxwell equations, and first unified the laws that govern electromagnetic waves. His theory lays the foundation of classic electromagnetism and can explain well how light interacts with different forms of matter in a classical sense. Decades later, Einstein pushed one step further, realizing that light could behave like a particle, and the quanta of light referred to as photons, carry the smallest amount of energy. After the building-up of quantum mechanics, generations of scientists have pushed their understanding of light into a quantum era. The theory of quantum electrodynamics(QED) starts by quantizing the spin-1 field (photons) and reaches a full

agreement between quantum mechanics and Einstein's theory of special relativity. It is such a beautiful frame that predicts light matter interaction very accurately.

Accompanying the deeper understanding of light is the application by modulating light. The interaction between light and mirrors and lenses offers great freedom to manipulate reflection and transmission to build a whole geometric optical system. Interactions with electrons in materials lead to the discovery of waveguides, laying the fundamental elements of all modern optical communication systems, and nano-photonic devices. In general, the ideas of manipulating light falls into two branches – we either make new materials, or build new structures. For example, the discovery of graphene show its promise in photonic applications in a wide range. The plamon frequency of graphene is much lower than the noble metals and thus greatly expand the plasmon application into mid-infrared region. However, the discovery of a new useful material does not always happen, and there are always limitations that natural materials can never overcome such as negative refractive index. Therefore, artificial materials – new structures with present materials – are invented to achieve those unusual properties. In the interested range of wavelength, these artificial materials are usually built up from micro- and nano-meter scales, and the fast developing modern nano-technology makes it possible to operate matter in such scales and boost the field of nano-photonics. A few subfields in nano-photonics are shown in blue boxes of Fig. 1.1, with some examples of theoretical and numerical methods in green and commonly taken packages in orange. Below is the a brief introduction of some.

1.1.1 Photonic Crystals

The semiconductor industry have completely changed the world since almost all modern technology relies on the invention of transistors. Semiconductors are useful due to its cystalline structure being able to tailor the electronic response of materials and thus modulate the flow of electrons [1]. Analogically, photonic crystalline structures are made in

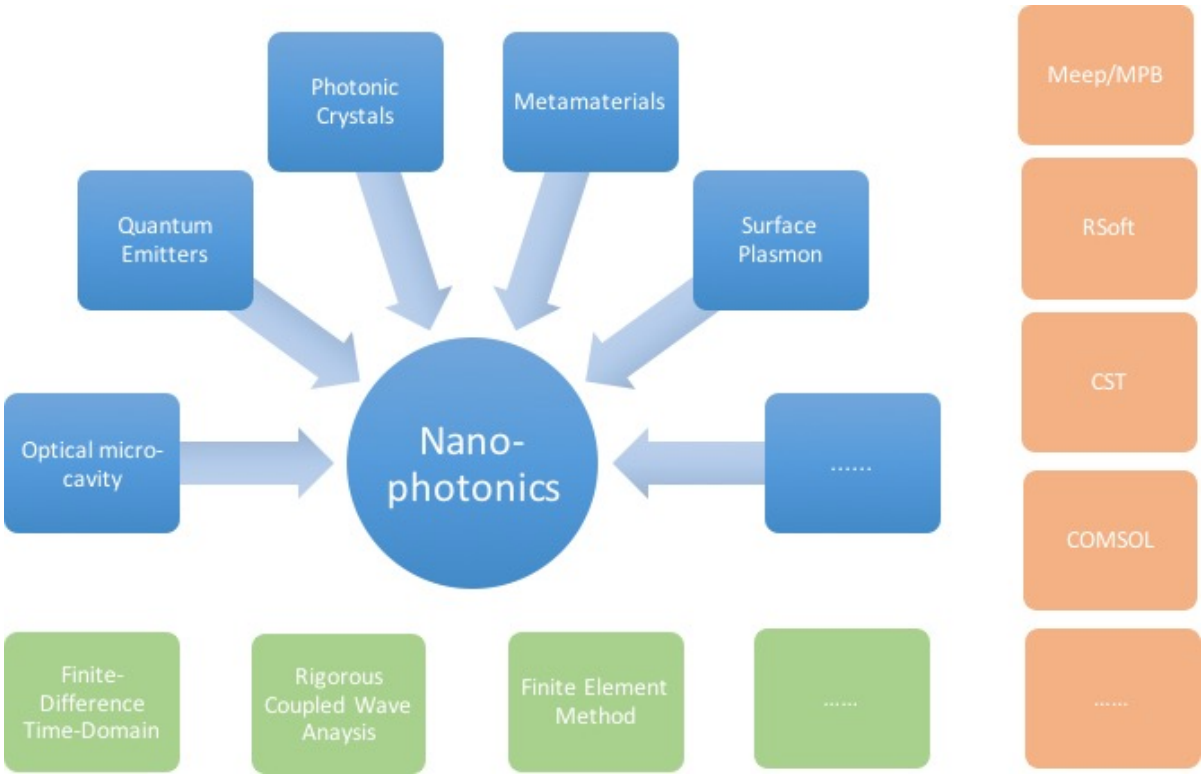

Figure 1.1 Some examples of the nano-photonics sub-fields (blue), theoretical/numerical methods (green), and commonly utilized packages (orange).

which composites with certain permittivity and permeability are arranged periodically. Photons propagating in such artificial materials will experience periodic potentials as electrons do in semiconductors, mapping a photonic counterpart from solid state physics such as Bloch theoremt. One of the most significant properties for semiconductors is the formulation of electronic band diagram due to periodicity, and so is it for the photonic crystals. In 1987, E. Yabnovitch [2] and S. Johnson [3] found that such periodic photonic crystals can localize modes and can be used to suppress spontaneous emission resulting from photonic bandgaps. These are the most initial ideas for the so-called photonic crystals.

In a PhC where only permittivity is periodically arranged, the Maxwell equation can

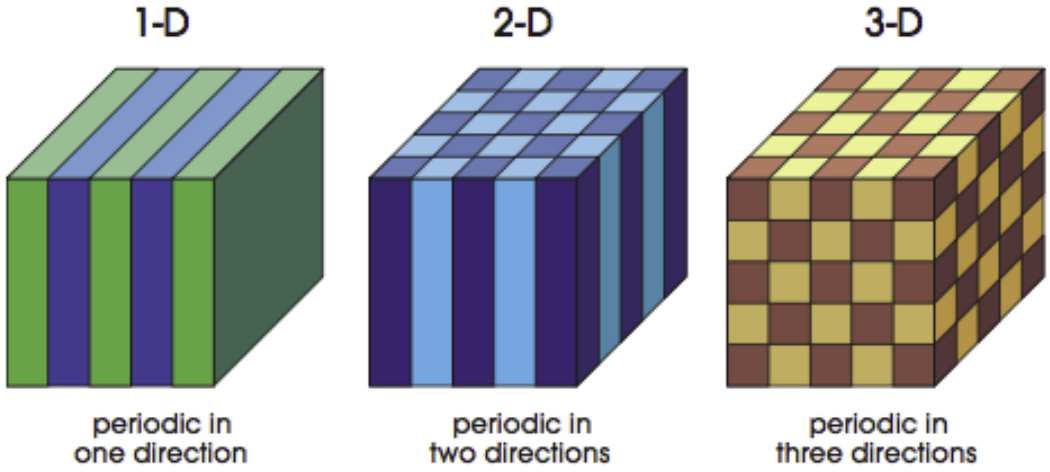

Figure 1.2 A sketch of 1D, 2D and 3D photonic crystals. Taken from Ref. [4].

be transformed into the wave equation form under harmonic oscillation written as:

$$L_H \vec{H}(\vec{r}) = (\frac{\omega}{c})^2 \vec{H}(\vec{r}), \tag{1.1}$$

where L_H is an Hermitian operator reading:

$$L_H = \nabla \times \frac{1}{\epsilon(\vec{r})} \nabla \times . \tag{1.2}$$

It turns out to be a standard eigenvalue problem. By combining the Bloch theorem that the field in a periodic potential can be the multiplication of a periodic function and a plane wave envelop:

$$\begin{aligned} \vec{H}(\vec{r}) &= \vec{u}_{\vec{k}n}(\vec{r}) e^{i\vec{k}\cdot\vec{r}}, \\ \vec{u}_{\vec{k}n}(\vec{r}+\vec{a}) &= \vec{u}_{\vec{k}n}(\vec{r}), \end{aligned} \tag{1.3}$$

and a Fourier expansion:

$$\begin{aligned} \vec{E}_{\vec{k}n}(\vec{r}) &= \sum_{\vec{K}} \vec{E}_{\vec{k}n}(\vec{K}) e^{i(\vec{k}+\vec{K})\cdot\vec{r}}, \\ \frac{1}{\epsilon(\vec{r})} &= \sum_{\vec{K}} \xi(\vec{K}) e^{i\vec{K}\cdot\vec{r}}. \end{aligned} \tag{1.4}$$

We get a set of eigenvalue equations where a pair of $(\vec{k}, n)$ corresponds to an eigen-frequency ω associated with an eiqen field $\vec{E}$. This set of eigen-solutions make a band diagram for PhCs. Figure 1.2 sketches photonic crystals of different dimensions, and Fig. 1.3 gives an example of the band diagram of a one dimensional photonic crystal. There is a gap as shadowed in yellow and no propagating photonic modes are allow within this range.

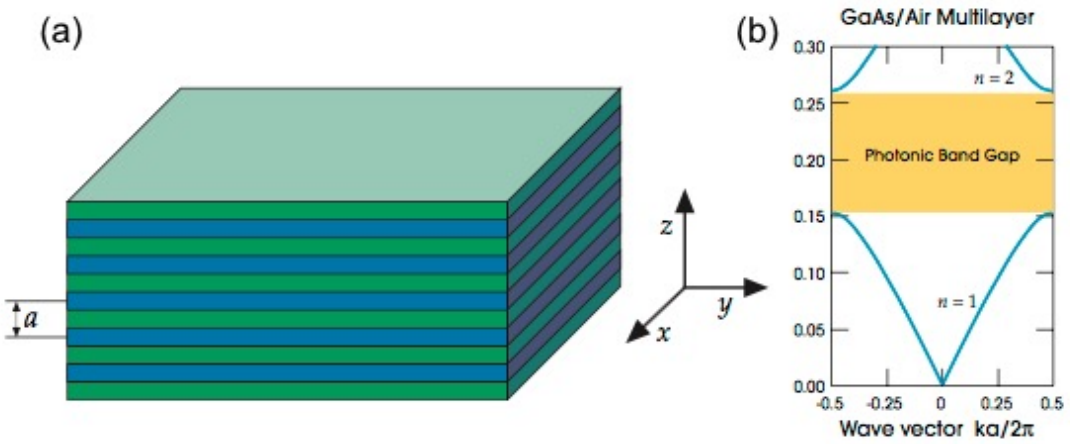

Figure 1.3 (a) A sketch of a 1D photonic crystal. (b) The photonic band diagram with a forbidden band inside. Taken from Ref. [4].

Due to its special photonic band diagram, PhCs can be almost used wherever needed to manipulate and control light. By introducing a point defect, one can easily make high-Q cavity higher than 10^6. By introducing a line defect, one can make PhC fibers or waveguides which can well confine and transmit light with little loss. By getting the frequency of light close to the flat edge of the band gap, one can greatly enhance the light-matter interaction since the light has a slow group velocity.

Table 1.1 summarizes the similarities between electrons in crystals and photons in PhCs. A more detailed table can be found in Ref. [4].

Table 1.1 Comparison between electrons in crystals and photons in PhCs

Crystals	PhC with periodic ϵ
Periodic $V(\vec{r}) = V(\vec{r}+\vec{a})$	Periodic $\epsilon(\vec{r}) = \epsilon(\vec{r}+\vec{a})$
Wave function Ψ	Magnetic field $\vec{H}$
$\Psi(\vec{r}) = u(\vec{r}+\vec{a})e^{i\vec{k}\cdot\vec{r}}$	$\vec{H}(\vec{r}) = \vec{u}(\vec{r}+\vec{a})e^{i\vec{k}\cdot\vec{r}}$
$H\Psi(\vec{r}) = E\Psi(\vec{r})$	$L_H\vec{H}(\vec{r} = (\frac{\omega}{c})^2\vec{H}(\vec{r})$

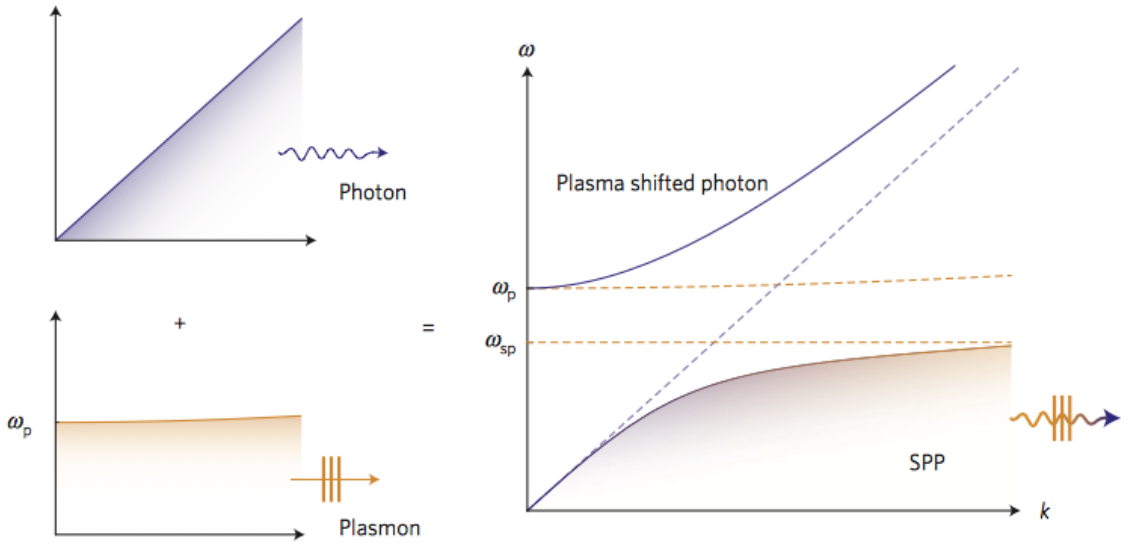

Figure 1.4 The coupling between a photon and a plamon gives rise to the surface plasmon polariton. Taken from Ref. [5]

1.1.2 Surface Plasmon Polariton

Plasmon is a quasi-particle, and it is the collective oscillation of free electron densities, while surface plasmons are those confined on the surface of certain materials, which in general are noble metals [6]. When the light couples with the plasmon, a polariton is formed and is referred to as surface plasmon polaritons (SPPs) shown in Fig. 1.4.

While studying the interaction of photons and plasmons, the Drude Model is most

commonly used to describe the electric response of metals. In the Drude Model, free electrons in metal are driven by an external field as:

$$\frac{\partial^2}{\partial t^2}\vec{r} + \gamma\frac{\partial}{\partial t}\vec{r} = -\frac{e\vec{E}}{m}e^{-i\omega t}, \tag{1.5}$$

where e is the charge of an electron, m is the mass, γ describes the damping due to loss which is the inverse of relaxation time. By taking $\vec{P} = -ne\vec{r}$ and $\vec{P} = (\epsilon - 1)\epsilon_0\vec{E}$, the Drude permittivity can be easily derived:

$$\epsilon(\omega) = 1 - \frac{\omega_p^2}{\omega^2 + i\gamma\omega}, \tag{1.6}$$

where $\omega_p = (ne^2/(m\epsilon_0))^{1/2}$ is the plasma frequency and n is the electron density. In higher frequencies, an interband transition term needs to be appended. The Drude model predicts and explains noble metals with free electrons having a negative permittivity under certain range of frequencies and it is the prerequisite for a TM SPP to exist.

Considering two materials with ϵ_1, μ_1 and ϵ_2, μ_2, each filling a half space of $y > 0$ and $y < 0$ respectively, one eigen-mode which propagates along x-direction have the transverse magnetic field:

$$H_z = \begin{cases} Ae^{-\kappa_1 y}e^{i\beta x} & \in I \\ Be^{\kappa_2 y}e^{i\beta x} & \in II \end{cases} \tag{1.7}$$

where β is the propagation constant and κ_i is the decaying factor defined as $\kappa_i = (\beta^2 - \epsilon_i\mu_i k_0^2)^{1/2}$. Substituting into $\nabla \times \vec{H} = -i\omega\epsilon_i\vec{E}$, we can get the components of electric fields:

$$E_x = \begin{cases} \frac{\kappa_1}{i\omega\epsilon_1}Ae^{-\kappa_1 y}e^{i\beta x} & \in I \\ -\frac{\kappa_2}{i\omega\epsilon_2}Be^{\kappa_2 y}e^{i\beta x} & \in II \end{cases}, \qquad E_y = \begin{cases} \frac{\beta}{\omega\epsilon_1}Ae^{-\kappa_1 y}e^{i\beta x} & \in I \\ \frac{\beta}{\omega\epsilon_2}Be^{\kappa_2 y}e^{i\beta x} & \in II \end{cases}. \tag{1.8}$$

By matching the continuity for both H_z and E_x, we are able to get the necessary conditions and dispersion relations for such a TM SPP:

$$\begin{aligned} &\frac{\kappa_1}{\epsilon_1} + \frac{\kappa_2}{\epsilon_2} = 0, \\ &\beta = k_0\sqrt{\frac{\epsilon_1\epsilon_2}{\epsilon_1 + \epsilon_2}\frac{\mu_1\epsilon_2 - \mu_2\epsilon_1}{\epsilon_2 - \epsilon_1}}. \end{aligned} \tag{1.9}$$

Since for a evanescent wave, κ_i should be a positive number, the signs of ϵ_i should be opposite for the two materials.

Due to the high reactive response from electrons, the surface plasmon polariton exhibits deep subwavelength features. This results in (1) a strong confinement of the field around the surface and (2) a strong enhancement of near field. These properties of SPP makes it superior in the near field optical applications including near field transducer [7], enhanced Raman spectrum [8], surface plasmon sensors [9] and so on.

1.1.3 Others

Besides the photonic crystals and plasmonics which are most relevant to this thesis work, there are a lot more ways to manipulate light-matter interaction, such as making metamaterials [10, 11], metasurfaces [12], quantum emitters [13] and so on.

Metamaterials are also a type of artificial metamaterials with periodic composites. Different from photonic crystals, the periodicity of metamaterials is much smaller than the wavelength of interest and the effective medium theory can be applied. Also metamaterials are usually resonant while photonic crystals are not. The composites are tailored by making different small resonators. The responses of all resonators towards external fields contribute to the overall macroscopic material properties such as the permittivity and permeability.

One of the most important applications of metamaterials is to make the left-handed materials, in which the permittivity and permeability are simultaneously negative leading to a negative refractive index. Phenomenologically, the permittivity and permeability under certain resonance can be written as:

$$\begin{aligned} \epsilon(\omega) &= 1 - \frac{\omega_p^2}{\omega^2 + i\gamma_e\omega}, \\ \mu(\omega) &= 1 + \frac{F\omega^2}{\omega^2 - \omega_0^2 + i\gamma_m\omega}. \end{aligned} \tag{1.10}$$

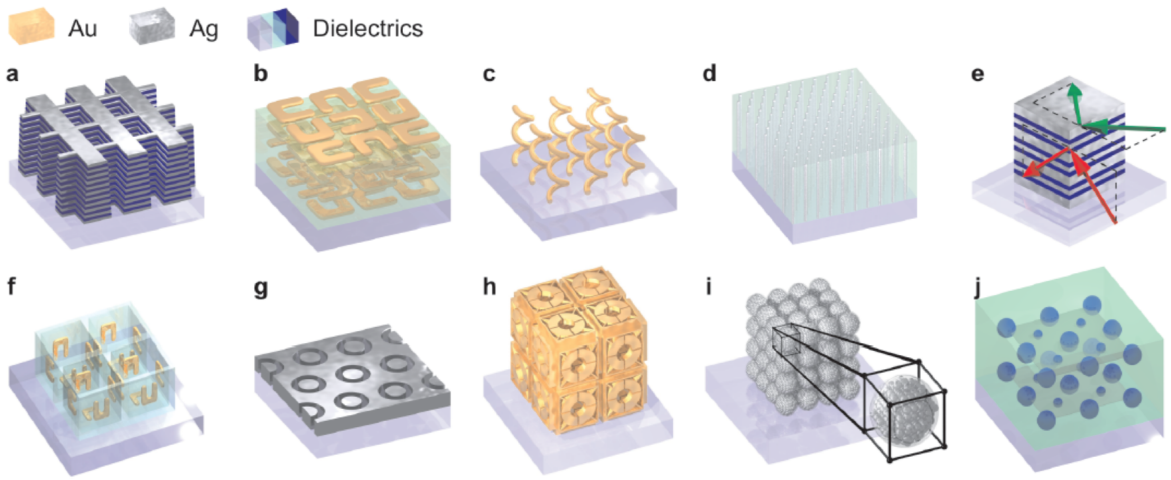

Figure 1.5 A few common designs for three dimensional metamaterials. Taken from Ref. [14].

By making structures in which the electric resonance and magnetic resonance are close to each other, one may essentially achieve a simultaneous negative ϵ and μ. Fig. 1.5 shows some common metamaterial designs taken from literature.

Metasurfaces are a special category of metamaterials, where they have very thin thickness. They are also made of resonant units. When light hits the surface, either their phases or polarizations would be tailored.

Quantum emitters are confined systems. When the size of the structure becomes smaller and smaller, quantum effects have to be taken into account. A photon energy matching the energy difference between two electronic states, resonances may occur, the electron will be excited, and stimulated emission could happen. There are a few common types of quantum emitters, such as dye molecules, quantum dots in semiconductors and so on. Quantum emitters are very useful – they can act as point dipoles since their size is really small; they can be applied into micro detectors and sensors since their intrinsic properties rely on the local fields; they can find ways in a lot of other state-of-the-art fields, such as quantum plasmonics, quantum information and so on.

1.2 Outline of this thesis

In this thesis, numerical studies on manipulating light-matter interactions, expecially on photonic crystals, plasmonics, and optical forces, are presented. It is organized as follows:

In Chapter 2, I have a systematic study on a photonic crystal structure with Dirac cones. This type of PhC was proposed with a zero-index behavior, while further work shows that this behavior will be lost at oblique incidence due to the excitation of the flat band modes. A new method by combining complex-k band calculation and absorbing boundary conditions for Bloch modes under the frame of COMSOL Multiphysics is also developed, and is brought to a detailed research on Bloch mode interaction inside the PhC slab.

In Chapter 3, I explore the posibilities of using graphene as opto-mechanical devices. I first theoretically study the optical gradient force arising from the coupling of surface plasmon modes on parallel graphene sheets. It is found to be orders' stronger than that between regular dielectric waveguides. I also calculate the deformation of graphene sheets under such gradient force by building an energy functional model, and demonstrate the mechanical state transitions of graphene sheets. This transition is accompanied by abrupt changes in transmission and reflection spectra, and can be used for optical actuators and sensors.

In Chapter 4, the research on a novel optical force called the lateral force is carried out. This force is a higher order effect and will be strongly enhanced in evanescent fields due to its relation with the spin angular momentum of light, and is closely related to the handness of particles. I first systematically study how this force arises in the interaction between plane waves/evanescent waves and achiral/chiral particles. Further more, I propose that the TE and TM surface plasmon can coexist on slabs made of left-handed materials, and changes of each mode can tune the lateral force on the particles,

which enhances the selectivity of chiral particle sortings.

In Chapter 5, I make a summary of my work.

CHAPTER 2. PHOTONIC CRYSTALS WITH DIRAC CONES

2.1 Novel photonic crystals with Dirac cones

Dirac cones are named after Dirac equations which governs the motion of elections in a relativistic frame, with a linear solution of energy E with respect to the wavenumber k. Usually electrons near the edge of a band has a parabolic feature since its energy is proportional to the square of velocity: $H = \hbar^2 k^2 / 2m^*$ with m^* to be the effective mass of electrons taking into account its interaction with lattices. However, there are special cases that the dispersion is linear and the electron behaves like a massless particle governed by the Dirac equation. In this sense, the neighborhood of the linear dispersion in the band structure is named the Dirac cone, and the degeneracy/intersection between two linear branches is named the Dirac point. Near the Dirac point, electrons show various extraordinary transport properties, such as quantum Hall effects.

Similarly, photonic crystals (PhCs), known as the semiconductors of electromagnetic waves, have been shown to exhibit a variety of novel properties and promising applications [4, 15, 16, 17, 18]. Their most notable features lie in the band structures shown in Chapter 1, which is closely related to the symmetry of the reciprocal lattice, and the interaction between photons and scatterers. Though photons in free space are massless, the interaction between photonic modes and the lattice will bring in an effective mass and thus the parabolic feature in the dispersion as well. However, there are also special cases where a Dirac cone could appear in PhCs.

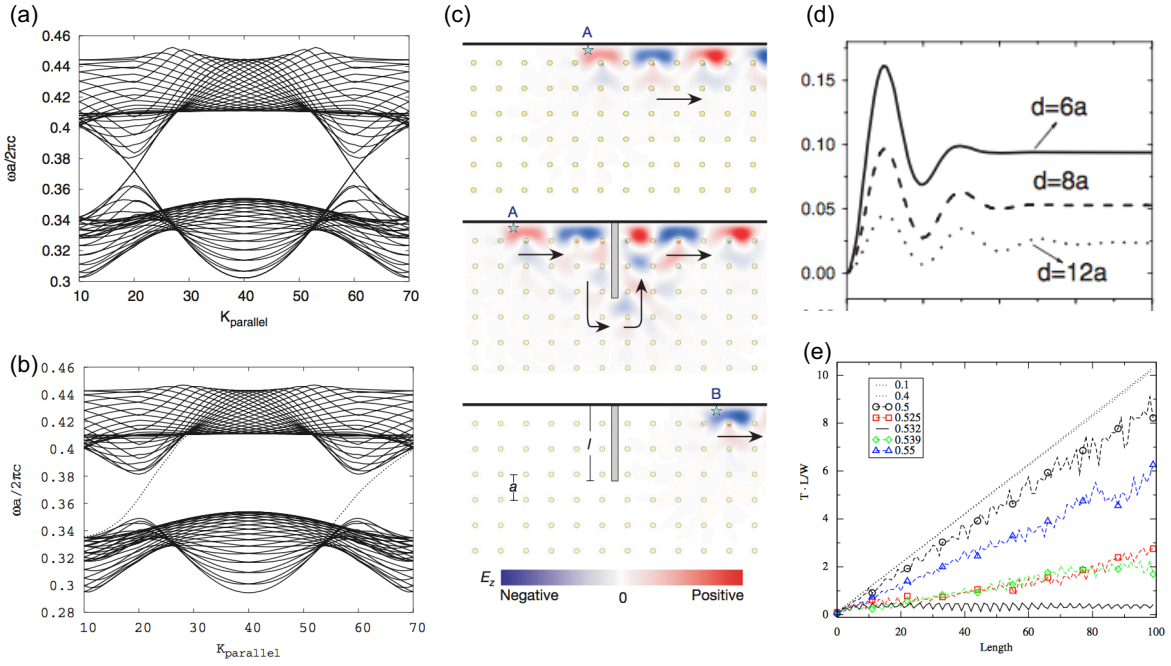

Figure 2.1 Dirac cone photonic crystal examples from literature. (a) Band diagrams of a hexagonal PhC with Dirac cones. (b) Degeneracy of the Dirac cone is broken by breaking the time reversal symmetry. A gap is opened and a unidirectional state bridging the upper and lower bands appears. Taken from [19]. (c) Experimental realization in Ref. [20]. The edge state is unidirectional and is robust against any defects. (d) Photonic oscillations over time, which features the *Zitterbewegung* motion, where d is width of the injected gaussian beam and a the periodicity of the PhC with dirac cones. Taken from Ref. [21]. (e) Pseudo-diffusive transport behavior. Different lines denotes incident waves with different frequencies. The lowest black wiggling solid line represents the Dirac frequency while all others are bias from that. The Dirac frequency line is mostly around a constant, showing that the tranmittance is inversely proportional to the thickness. Figure taken from Ref. [22]

In 2008, F. Haldane and S. Raghu [19] first theoretically demonstrated the analogs of quantum Hall effects in a two dimensional PhC. While a PhC with triangular lattices can preserve a Dirac-point doublet at the boundary of the Brillouin Zone, breaking the time reversal symmetry by using opto-magneto materials can perturb the degeneracy and a unidirectional edge state is guaranteed to appear, bridging the whole gap. The number and the direction of these unidirectional states may be derived from the Chern number difference between the upper band and the lower band. Their ideas were realized

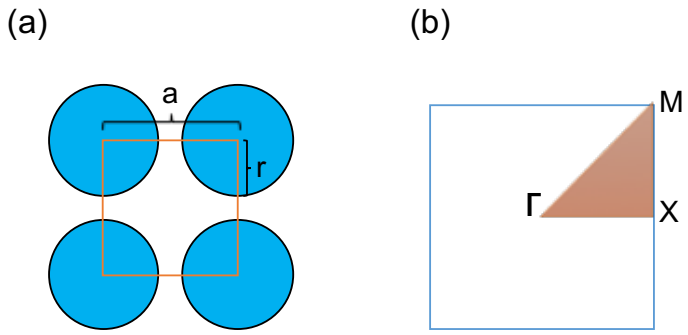

Figure 2.2 (a) The real lattice of the PhC. The embedded rods are made of alumina, with $\epsilon = 9.8$, $\mu = 1$. The radius of the cylinder is $r = 1.59$mm, and the lattice constant is $a = 4.66153r$ for the Dirac cone to appear. (b) The reciprocal lattice of the PhC.

experimentally by Z. Wang *et al.* in 2009 [20]. Their works laid the foundation of the booming field of topological photonics, and later novel properties of PhCs with Dirac cones were intensively studied. In 2008, X. Zhang [21] demonstrated the existence of the *Zitterbewegung* motion of photons in a two dimensional PhC with Dirac points, which was first predicted by Schrodinger originating from the interference between the positive and negative energy states, but very hard to be observed in an electronic system. In 2010, M. Diem *et al.* [22] proposed a pseudo-diffusive transport behavior in which the

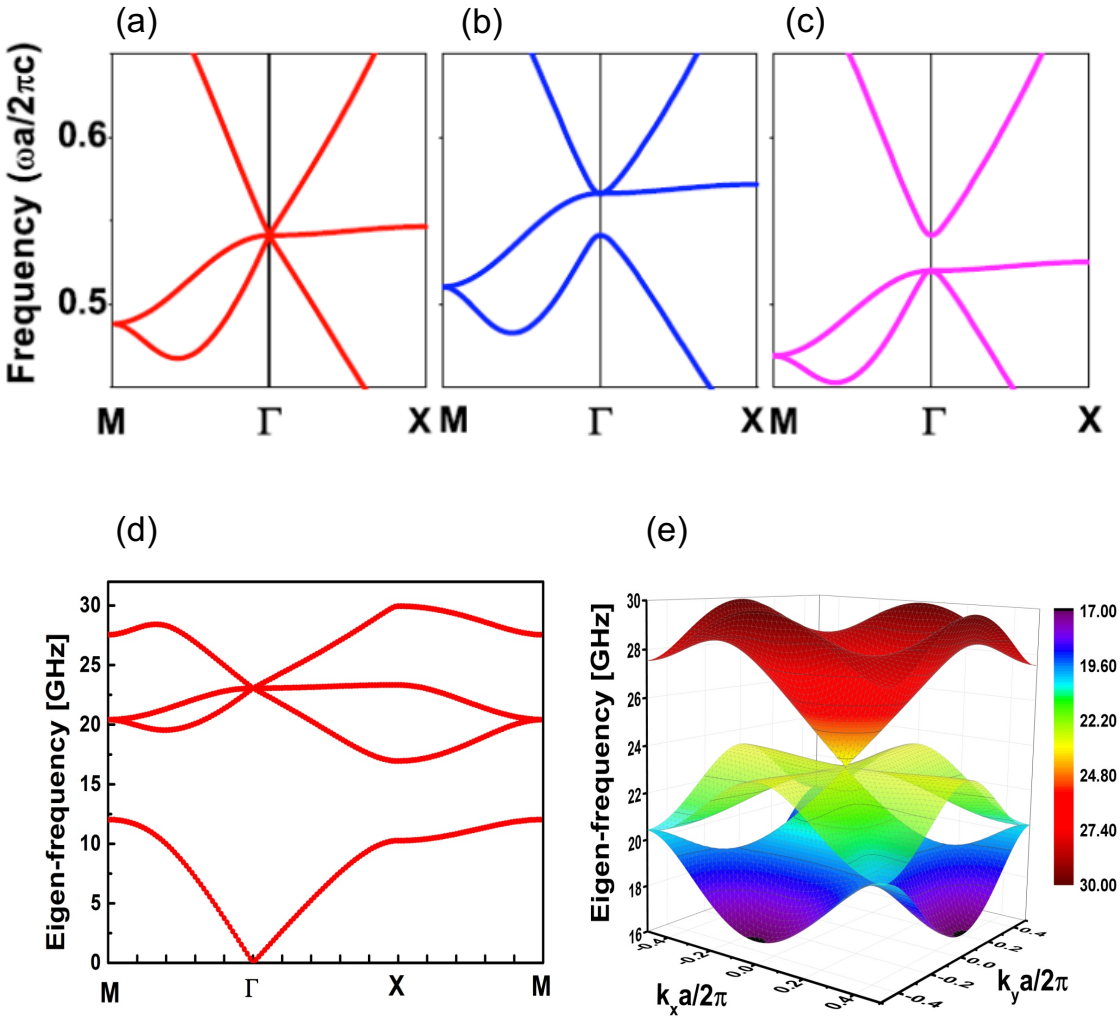

Figure 2.3 The normalized band structure for TE modes (taken from Ref. [23]) when the ratio a/r is (a) equal to (b) smaller (c) larger than 4.66153. (d) & (e) The complete band diagram with a/r=4.66153. There is a triple degeneracy at the Γ point and the Dirac frequency is 23.05161 GHz.

transmittance near the Dirac point of a two dimensional hexagonal PhC is inversely proportional to the thickness of the PhC. In 2011, X. Huang *et al.* [23] proposed a PhC structure with a square lattice. By modulating the lattice parameters, they found Dirac cones at the center of the Brillouin zone and, at the Dirac point, the PhC behaves

similarly to a zero-index material. However, due to the symmetry of the lattice, a flat band crossing the Dirac point corresponding to magnetic longitudinal modes inevitably appears, and it is known that off-normal incident waves can excite modes from this flat band.

Work on this chapter is based on their findings and a thorough study on the flat band Bloch modes using a newly developed method is carried out. In this chapter, the complex-k band diagram is first calculated and a numerical demonstration is shown later how the flat band contributes to the behavior of the PhC, which results in the deviations from the the zero-index medium response when illuminated by a wave with a non-zero k_y (wave vector component parallel to the interface). Then by implementing an absorbing boundary condition for Bloch waves, a semi-analytic formulation is built to explain the flat band modes couple and contribute to the transmission spectrum features. The origin of the different line-shape features of the resonances and how they are affected by material losses are discussed as well.

2.2 2D photonic crystals with Dirac cones at Γ-point

2.2.1 Accidental degeneracy on the center of Brillouin zone

A detailed numerical study of the PhC with Dirac cones following Ref. [23] are first presented. Noting that there have been different conventions to define polarizations in the photonic area, and for clarity the TE mode as used throughout this chapter, is denoted whose electrical field parallel to the rod axis (out of plane). In the simulation, a square lattice in which alumina rods are periodically surrounded by vacuum is taken (see Fig. 2.2). The permittivity and permeability of the alumina rods are chosen as ϵ=9.8 and μ=1, respectively. By changing the filling ratio of the rods, the band gap between the doubly degenerated branches representing the dipolar modes, and the single monopole mode branch will change accordingly. Details are shown in Fig. 2.3. Figure 2.3 (b) and

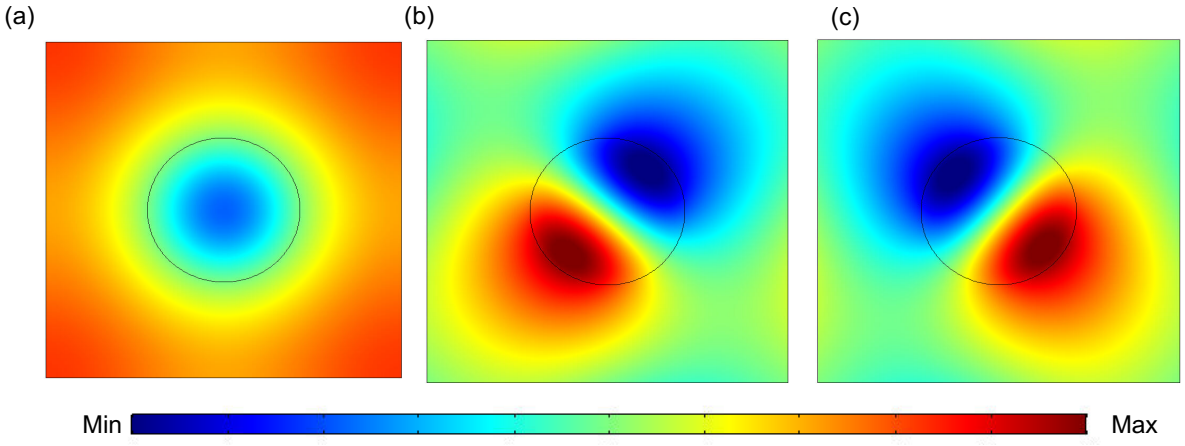

Figure 2.4 Normalized E_z field distribution of the eigen-modes at the Dirac point. The triple degeneracy contains one monopole mode and two dipole modes.

(c) show the band diagram for $r/a < 4.66153$ and $r/a > 4.66153$ respectively, while Fig. 2.3 (a) represents that with $r/a = 4.66153$. It is apparent that at a specific filling ratio (radius of the cylindrical rods), the gap closes and a triple degeneracy appears. This degeneracy at the center of the Brillouin zone of the reciprocal lattice, formed by two linear branches (Dirac cone) and a third flat band, merely resulting from the geometrical parameter modulation, is called accidental degeneracy. In our configuration, it happens at $a = 4.66153r$. A complete band diagram showing the Dirac cone is plotted in Fig. 2.3 (d) and (e). Figure 2.4 shows the normalized field distribution (E_z) with monopole and dipole profiles at the Dirac frequency.

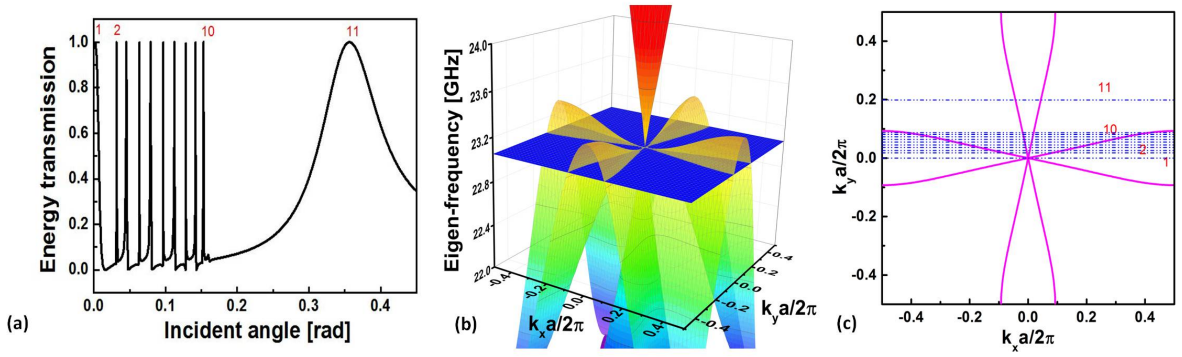

Figure 2.5 (a) The transmission spectrum versus the incident angle. The PhC is finite in the propagation direction (x direction), in which 11 rows are present (refer to Fig. 4 for a visual sketch). (b) A cut-plane of the Dirac frequency over the full band. There are intersections with the middle band. (c) A top view of the cut-plane and the intersections. Each blue horizontal straight dash line indicates a certain k_y (component of the wave vector parallel to the interface between the air and PhC), or the incident angle. Numbers of the horizontal straight lines correspond to peaks in (a). It is shown that peak 1 corresponds to the zero-index mode with $k_x = k_y = 0$, due to the coupling with the linear branch. Peak 2 to 10 indicate there are 2 propagating modes with their reflective counterparts in the PhC, while peak 11 corresponds to only 1 propagating mode and its reflective counterpart, both due to the coupling with the flat band.

2.2.2 Zero-index and loss of zero index behavior

This PhC with Dirac cone at the center of Brilliouin zone (k=0) behaves similarly to an homogeneous zero-index material. Figure 2.6 is extracted from Ref. [23]. It shows that at normal incidence to the interface, all phases inside the medium will flat out. For the propagation phase of a monochromatic wave simply satisfies $\theta = nk_0l$ where n is

the effective index, k_0 is the free space wavenumber, and l is the distance that the wave propagates, a zero-index medium accumulates no phase change for certain waves and the outgoing phase front will be subject to the shape of the interface. It is worth noting that although the periodicity of the PhC is usually comparable to the free space wavelength where the effective medium theory fails, it is still valid to describe the whole media by an effective index near the Dirac cone, where the effective wavelength is ideally infinity.

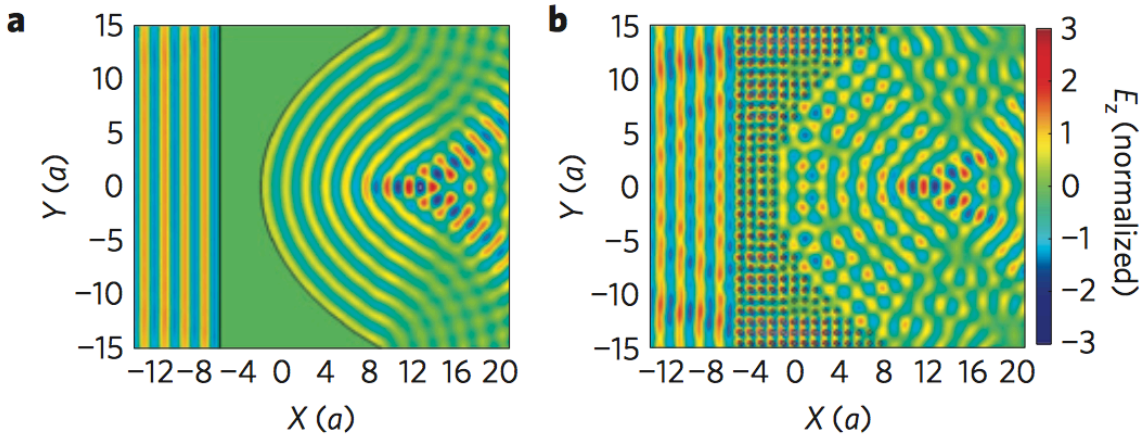

Figure 2.6 Field plots of zero-index behavior taken from Ref. [23]. (a) A plane wave is normally incident on a homogeneous impedence matched zero index material. Phases in the medium are the same everywhere, and the outgoing wave front is subject to the shape of the interface between the medium and air. (b) A plane wave at the Dirac frequency is normally incident on the PhC. The PhC behaves as an impedence matched zero index medium and the outgoing wave front is subject to the interface between the PhC and the air too.

The classical Fresnel law $n_i sin(\theta_i) = n_t sin(\theta_t)$ tells us that at the interface of two media with n_i=1 and n_t=0 respectively, all waves with oblique incident angles will be totally reflected. In addition, the reflation between impedance and reflection $r = (Z - 1)/(Z+1)$ tells that even for normal incidence, only an impedance matched media can let the waves pass through. However, in this PhC, electromagnetic waves are still allowed to transmit at oblique incidence and its angular transmission spectrum is featured by a few

Fabry-Perot-like peaks [see Fig. 2.5 (a)]. This is an indication that modes with a non-zero k_y are excited. Figure 2.5 (b) is a cut-plane of the Dirac frequency over the complete band diagram. Figure 2.5 (c) is a top view of the cut-plane and the intersections. Each blue dashed line represents incident waves with a certain k_y (the incident angle). It is clear that the normal incidence line (k_y=0) intersects only at the center where k_x is 0. However, the oblique incidence lines ($k_y \neq 0$) intersect with the band more than once at $k_x \neq 0$. This indicates that either one or two propagating modes are excited, with their reflective counterparts. In the following sections, results from further investigation on these modes are presented and how these resonances are formed is explored, by building up our own numerical methods.

2.3 Bloch modes interaction

For a full understanding of the middle flat band mode excitated by the oblique incident waves, and the interaction between different Bloch modes inside the PhC slab, a new computational technique using the commercial electromagnetics package COMSOL Multiphysics is implemented, by combining the complex-k band calculations and absorbing boundary conditions for Bloch modes. This method takes some advantages over the traditional ones. Traditional methods employed for the study of PhCs include band calculations and reflection/transmission spectra measurements [24]. However, band calculations only give information on the number of Bloch modes and on the eigen-field. Scattering measurements describes the finite slab in a macroscopic way and treat it as a "black box" missing information on the details, such as how different modes interact and how each mode gets coupled into the radiated waves. In the new method presented, the complex-k band calculations will give information of both propagating and evanescent modes under excitation with certain frequencies and incident angles, while the absorbing boundary conditions eliminates the back-reflection from the other end of a slab, and help

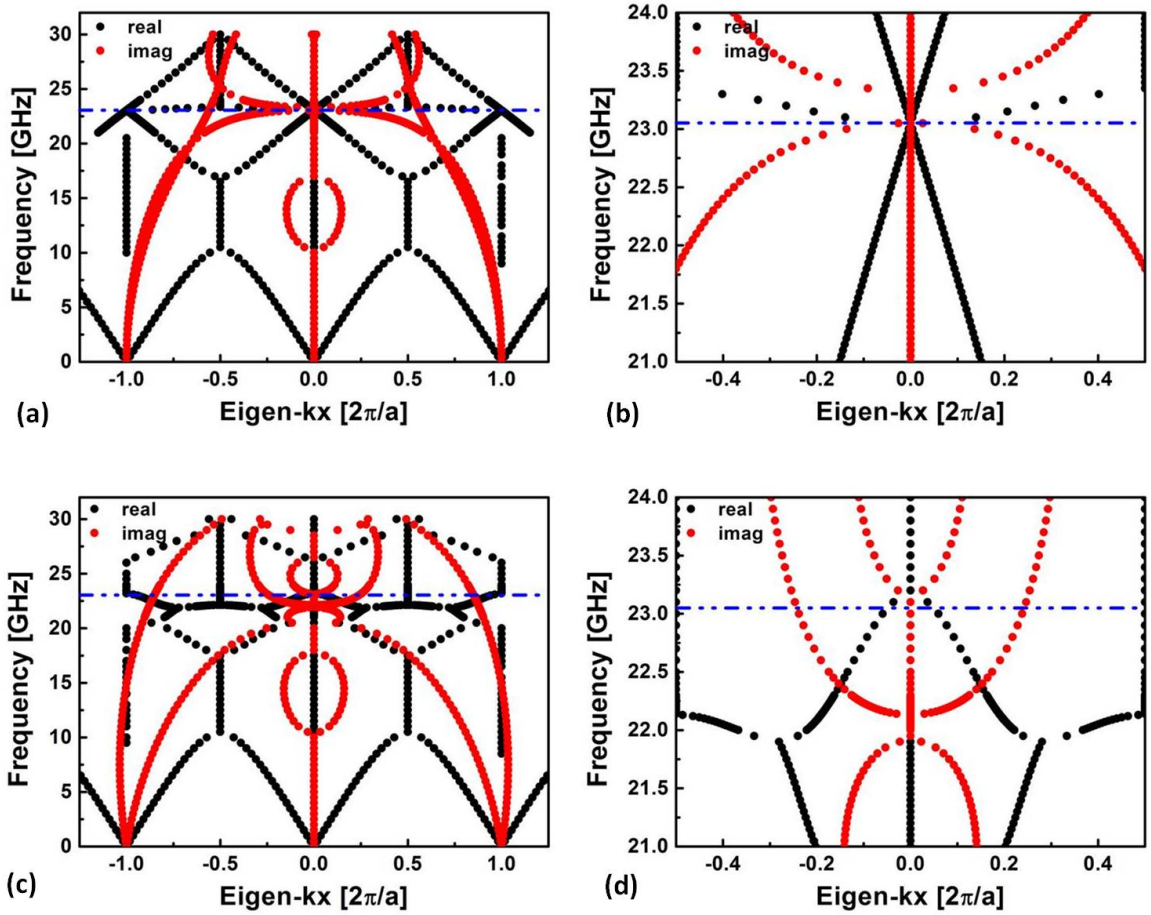

Figure 2.7 Complex-k band diagram. x-axis: the eigenvalue of the propagating constant. y-axis: frequency of the EM wave. The black dots denote the real part of the eigen-k_x, and the red dots denote the imaginary part of the eigen-k_x. The blue dash shows where the Dirac frequency lies. (a)&(b): Complex-k band structure for normal incidence ($k_y = 0$) at different ranges of frequencies. (c)&(d): Complex-k band structure for the incident angle of 0.4 rad ($k_y = 188\,\mathrm{m}^{-1}$) at different ranges of frequencies. From (a) and (c), we plot the extended Brillouin zone, from which we can see the periodicity for the real part of k_x.

us gain the coupling efficiency between Bloch modes and planewaves across the PhC-air interface.

2.3.1 Complex-k band diagram and eigen-wavevector calculation

Generally the eigenfrequencies of a PhC are calculated at given Bloch vectors as shown in the last section. However there are many cases in which knowing the eigenvalues of wave vectors at a given frequency is more helpful. In this case, the shape of modes and their interaction at a given frequency (the Dirac frequency) and a given incident angle are of more interest. Thus a so-called comlex-k-band calculation is needed. This section shows how this information can be obtained from simulations with the package COMSOL Multiphysics, by specifying the field equations in their weak form module.

In view of the Bloch theorem, the electric field in a periodic photonic structure can be written as the product of a periodic function and a plane wave envelope function:

$$\vec{E}(\vec{r}) = u(\vec{r})e^{-i\vec{k}\cdot\vec{r}}\hat{E}, \qquad u(\vec{r}) = u(\vec{r}+\vec{a}) \tag{2.1}$$

For the TE wave (the electric field parallel to the rod axis), the vectorial wave equation is reduced to a scalar one:

$$\nabla\cdot(\frac{1}{\mu}\nabla E_z) + \epsilon\frac{\omega^2}{c^2}E_z = 0 \tag{2.2}$$

Replacing E_z by its Bloch form, it becomes:

$$\nabla^2 u - i\nabla\cdot(u\vec{k}) - i\vec{k}\cdot\nabla u - k^2 u = -\epsilon\frac{\omega^2}{c^2}u \tag{2.3}$$

Taking the method in Ref. [25], integral of the weak expression by multiplying a test function v on both sides and integrating by parts in one unit cell lead to:

$$\begin{aligned} 0 &= \int \mathrm{d}\Omega[-\frac{k^2}{\mu}vu - \frac{iv}{\mu}\vec{k}\cdot\nabla u + \frac{iu}{\mu}(\nabla v)\cdot\vec{k} - (\nabla v)\cdot\frac{\nabla u}{\mu} + \frac{\epsilon\omega^2}{c^2}vu] \\ &= \int \mathrm{d}\Omega\cdot W \end{aligned} \tag{2.4}$$

where v is the test function of u. Since only the in-plane (xy plane) wave vector is considered, there are three degrees of freedom in the weak expression, k_x, k_y and ω, where k_y and ω are conserved over the air/PhC boundary. To calculate the eigenvalues of k_x, the other two need to be prescribed. Frequencies are scanned within a large range containing the Dirac frequency for both normal ($k_y = 0$) and oblique ($k_y = 188\text{m}^{-1}$) incidence, and results are plot in Fig. 2.7. All black dots denote the real part of eigen-k_x, while all red dots denote the imaginary part. Figure 2.7(a) & (b) are calculated at k_y=0 implying normal incidence, while Fig. 2.7(c) & (d) are calculated at k_y=188 m^{-1} implying oblique incidence. It is clearly seen that for the normal incidence, there is a triple degeneracy at $f = 23.05161\text{GHz}$ with eigenvalues $k_x = 0$ (black dots). Therefore, the Bloch wave is reduced to the periodic function $u(x, y)$, and the Bloch phase term turns into a constant independent of the propagation distance. Around the degeneracy, the frequency is linear to the wave number, as expected for that near the Dirac cone. However, the photonic crystal's behavior is quite different when a non-zero k_y is presented. Figure 2.7(c) and Fig. 2.7(d) show that at $k_y = 188\text{m}^{-1}$, the Dirac cone and the zero-index mode disappear. Instead, more Bloch modes appear—the mode with vanishing $\text{Im}(k_y)$ is a propagating mode with propagation constant $k_x = 41.27\text{m}^{-1}$ (or 0.0487 in units of $2\pi/a$); the others with non-zero $\text{Im}(k_y)$ are attenuated modes.

2.3.2 Monomodal and multimodal resonances in the PhC slab

In the preceding sections, the eigenmodes with a given frequency and one component of the wave vector are analyzed, and it leads to the conclusion that when k_y is nonzero, there will be propagating Bloch modes inside the PhC. Therefore, these Bloch modes are likely to be reflected and transmitted multiple times at the PhC-air interface as plane waves in a homogeneous dielectric slab. It is hypothesize to be the reason for the peaks appearing in the angular transmission spectrum. To prove this, two sets of simulations are performed. In one set, the amplitudes and phases of both incoming and outgoing

plane waves were measured [Fig. 2.8 (a)]. From $E_{\text{out}} = M_{\text{full}} E_{\text{in}}$, the transfer function M_{full} was calculated. In the other set, the transfer function under the assumption of multiple reflections should satisfy:

$$\begin{aligned} M_{\text{FP}} &= \mathbf{t}_{\text{pa}} \cdot \mathbf{A} \cdot \mathbf{t}_{\text{ap}} + \mathbf{t}_{\text{pa}} \cdot (\mathbf{A} \cdot \mathbf{r}_{\text{pa}} \cdot \mathbf{A} \cdot \mathbf{r}_{\text{pa}}) \cdot \mathbf{A} \cdot \mathbf{t}_{\text{ap}} \\ &\quad + \mathbf{t}_{\text{pa}} \cdot (\mathbf{A} \cdot \mathbf{r}_{\text{pa}} \cdot \mathbf{A} \cdot \mathbf{r}_{\text{pa}})^2 \cdot \mathbf{A} \cdot \mathbf{t}_{\text{ap}} + \cdots\cdots \\ &= \mathbf{t}_{\text{pa}} \cdot (\mathbf{I} - \mathbf{A} \cdot \mathbf{r}_{\text{pa}} \cdot \mathbf{A} \cdot \mathbf{r}_{\text{pa}})^{-1} \cdot \mathbf{A} \cdot \mathbf{t}_{\text{ap}} \end{aligned} \tag{2.5}$$

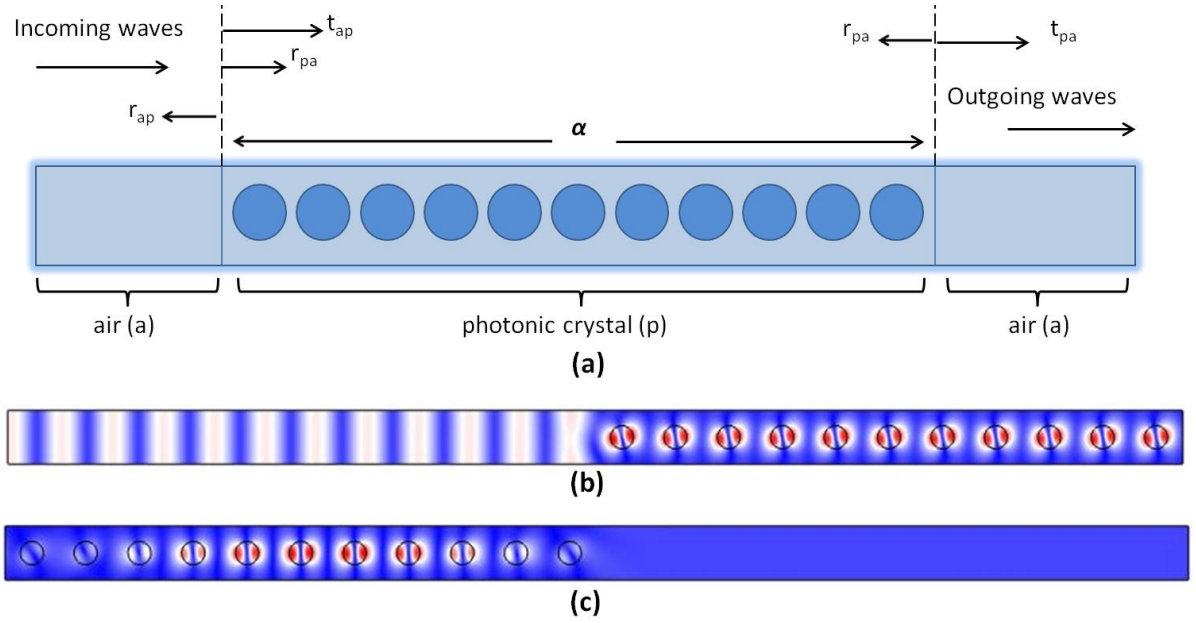

Figure 2.8 (a) A sketch for multiple reflections in the PhC. The incoming and outgoing waves are plane waves. The field inside the PhC is the superposition of a set of Bloch waves. In the propagating direction (x direction), 11 rows of rods are present. In (b) and (c), $|E|$ is plotted, with $f = 23.05161$GHz and $k_y = 188\text{m}^{-1}$. (b) Plane waves are excited and absorbed at the leftmost boundary, and the relevant Bloch modes are absorbed at the rightmost boundary. (c) One Bloch mode is excited and its reflective counterpart is absorbed at the leftmost boundary; plane waves are absorbed at the right.

The subscript "p" denotes PhC and "a" denotes air. $\mathbf{t}$ and $\mathbf{r}$ refer to the transmission and reflection coefficients at the PhC-air interface, and $\mathbf{A}$ denotes the phase change of the Bloch mode traveling from one end of the PhC to the other end. Generally, all variables

in the equation should be a matrix, and the dimension of the matrix equals the number of the eigenmodes. The total field inside the PhC could be expanded into a complete linear combination of all Bloch modes, including both propagating and evanescent modes, while if the PhC waveguide is long enough, the effect of the evanescent modes can be neglected. Therefore the resonant behavior of a long PhC slab is determined by the propagating waves to a high degree of accuracy.

Figure 2.3 shows the traditional band structure consisting of only the propagating modes. Figure 2.5 (c) shows that peak 2 to 10 correspond to double propagating modes in the PhC, while peak 11 corresponds to a single propagating mode. In the monomodal case (peak 11), the matrix is reduced to a scalar, while in the bimodal cases (peak 2 to 10),

$$\begin{aligned} \mathbf{t}_{\mathrm{ap}} &= \begin{bmatrix} t_{\mathrm{ap}}^{1} \\ t_{\mathrm{ap}}^{2} \end{bmatrix}, & \mathbf{r}_{\mathrm{pa}} &= \begin{bmatrix} r_{\mathrm{pa}}^{11} & r_{\mathrm{pa}}^{12} \\ r_{\mathrm{pa}}^{21} & r_{\mathrm{pa}}^{22} \end{bmatrix}, \\ \mathbf{A} &= \begin{bmatrix} e^{-ik_{x1}x} & 0 \\ 0 & e^{-ik_{x2}x} \end{bmatrix}, & \mathbf{t}_{\mathrm{pa}} &= \begin{pmatrix} t_{\mathrm{pa}}^{1} & t_{\mathrm{pa}}^{2}. \end{pmatrix} \end{aligned} \tag{2.6}$$

The superscripts "1" and "2" denote different eigenmodes. The off-diagonal terms of the reflection matrix do not necessarily disappear, since there might be coupling between the two Bloch modes, or in other words, there might be transitions between different eigenmodes in the presence of a pertubation. Then the problem of measuring the transfer matrix turns into the problem of measuring the reflection and transmission coefficients at each interface. To resolve this, a port that can perfectly excite and absorb Bloch waves was developed. The port boundary condition is based on an orthogonality relation of the eigenmodes of the PhC. We again implement this via the weak form specification in the COMSOL package.

The weak expression for a general frequency domain EM problem can be separated into a domain and a boundary part [26], and the boundary term can be simplified as:

$$W_b = \vec{v} \cdot [\hat{n} \times (\frac{1}{\mu} \nabla \times \vec{E})] = \pm i \frac{\omega}{c} v H_y \tag{2.7}$$

Here, we choose $\hat{n} = -\hat{x}$ at the input side (left) and $\hat{n} = \hat{x}$ at the output side (right). This constraint at the boundary allows us to define a port that can excite or absorb any mode, as long as we can expand it into a linear superposition of all known eigenmodes [(Eqn. (11.1) in [27]], and retrieve each component by taking the inner product between the partial field and the total field, as long as a valid orthogonality relation is utilized. Note that, in a lossless system, we shall take Eqn. (6) in [28] as the orthogonality relation, while in a lossy case, a generalized form is essential [Eqn. (4) in [26]]. For a succinct summary, the field H_y of the Bloch modes that we need to excite or absorb reads

$$H_y = \sum_n |n><n|H_y> = \sum_n h_{\mathrm{yn}} \frac{\int \mathrm{d}y (e^*_{\mathrm{zn}} H_y + E_z h^*_{\mathrm{yn}})}{\int \mathrm{d}y (e^*_{\mathrm{zn}} h_{\mathrm{yn}} + e_{\mathrm{zn}} h^*_{\mathrm{yn}})}, \tag{2.8}$$

where e_{zn} and h_{yn} are the z component of the electric field and the y component of the magnetic field for the eigen-modes that we import from the calculations discussed in Section 2.

Figure 2.8 shows the setup. We truncate the air/PhC/air system into different sections. In Fig. 2.8 (b), a plane wave with a given k_y is excited at the left and the corresponding Bloch wave is absorbed by the right port. From this simulation, we can determine t_{ap}. In Fig. 2.8 (c), we import the eigen-field obtained from the complex-k band calculation, and then this Bloch mode is excited and its reflective counterpart is absorbed. From the latter simulation, r_{pa} and t_{pa} can be obtained.

Figure 2.9 (a) and Fig. 2.9 (b) show a comparison between the energy transmission calculated from a full simulation and the multiple-scattering assumption. Both results are in excellent agreement, except for the smallest angles due to numerical precision limitations. Since the Q-factor is very high, the spectrum contains some extremely narrow peaks for low incident angles which are difficult to resolve accurately. By adding

loss into the system (setting $\epsilon = 9.8 + 6.8 \times 10^{-4}i$ for the alumina rods), those peaks are effectively lowered and broadened. In this way, results from both methods coincide perfectly in Fig. 2.9(c) and Fig. 2.9(d).

All these resonances can be classified into three categories. Peak 1 results from the excitation of an impedance-matched zero-index mode, which is the mode of interest in [23]. Peak 11 has a symmetric line shape, which is due to the multiple reflections and transmissions of a single Bloch mode in the PhC slab, and is the lowest-order resonance for the steep-slope mode in Fig. 2.5(c). The other peaks at small incident angles are of more interest. Their asymmetric, or Fano-like features indicate that at least two different modes contribute to the spectrum simultaneously, with one playing the discrete resonant role, and the other working as the continuous background process [29]. As a first-order approximation, the coupling (the off-diagonal term in r_{pa}) between two eigen-modes are ignored, and the transfer matrix of each mode is calculated separately. Results are displayed in Fig. 2.10 (a). The red resonant curve corresponds to the small-slope mode in Fig. 2.10 (c). Its Fabry-Perot resonance origin preserves the symmetric line shape. The blue curve shows a continuous non-resonant feature, contributed by the steep-slope mode, and modifies the total transmission from symmetric to asymmetric. For a more rigorous analysis, one needs to diagonalized the matrix and take superposition of the two eigen-Bloch modes to find the exact resonant and background modes, so that the coupling effects are taken into account. However, it's apparent that the small-slope mode dominates the bimodal resonance.

One might also have found that the small loss added into the system has a much more significant impact on the bi-modal resonance than the monomodal one, suppressing the peak into less than half of its original. This can be understood from the dispersion relations. Figure. 2.10 (b) plots the dispersion relations for two incident angles. The blue curve corresponds to the eigenmode with larger incident angle of 0.356 rad (peak 11), while the red curve corresponds to the bi-eigen-modes with smaller incident angle

of 0.112 rad (peak 7). The resonant mode has a much smaller slope (group velocity) in the bimodal case than that in the monomodal case (approximately 2.7 times smaller in Fig. 2.10 (b)). This slow light effect implies the existence of a higher density of states, making the field enhancement stronger and the Q-factor larger in a lossless system. However on the other side, these high Q-factor peaks will also be more sensitive to system losses, since a slower light is more readily absorbed when propagating.

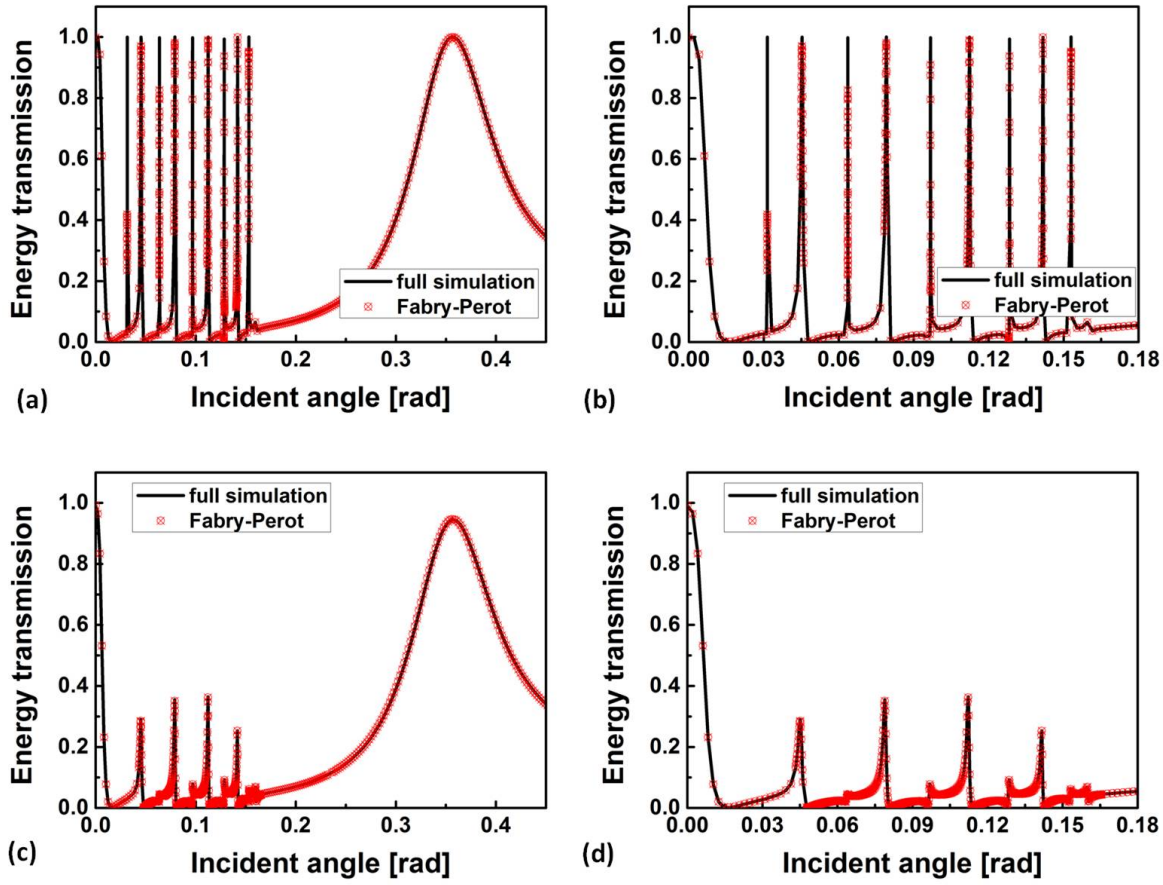

Figure 2.9 Energy transmission($|M|^2$) vs. incident angle. The black lines denote the transfer function M which comes from the direct measurement of a full simulation in the air/PhC/air system. The red dots denote the transfer function M determined from the multiple reflection assumption. (a) and (b) correspond to a lossless system, where the alumina rods have $\epsilon = 9.8$. (c) and (d) correspond to a lossy system, where the alumina rods have $\epsilon = 9.8 + 6.8 \times 10^{-4} i$.

In addition, since these peaks are the result of Fabry-Perot resonances, the number of the peaks is related to the number of unit cells in the normal direction. As the slab grows thicker (the number of unit cells in the normal direction increases), the slab will be able to accommodate more resonant modes, and thus the number of sharp peaks will increase. The positions of the peaks will shift too. However, there is no one-to-one correspondence between the number of peaks and the number of unit cells. Recalling that the resonant wavelengths of a Fabry-Perot cavity are typically functions of the size of the cavity, i.e, for a perfect Fabry-Perot cavity, a strict standing wave boundary condition has to be met, a similar situation happens to the monomodal resonance at large incident angles. When there is only one propagating Bloch mode excited, the denominator of the the transfer matrix is commutable and reduces to $[1 - r_{\mathrm{pa}}^2 \exp(-2jk_x d)]^{-1}$. Therefore the position of the monomodal resonance could be estimated as $k_x d \sim n\pi$, due to the non-zero phase at the boundary and on condition that no higher-order diffraction happens. In the bimodal case, the simulation becomes more complicated, since there will be no simple standing-wave conditions. However, one can always find the resonant positions by performing a numerical study of the denominator as is shown here.

2.4 Conclusion

In this chapter, a numerical study of the flat band Bloch modes in a photonic crystal with Dirac cones is reported. It is proved numerically that the non-zero k_y gives rise to non-zero index medium behavior. Furthermore, to understand how modes propagate and interact in the PhCs, the weak expressions are derived and the complex-k band and transmission calculations are performed. Though the explanation of the spectral features turns out to be multiple reflections of the eigenmodes, the simulation method offers us a way to separate the coupled Bloch modes in a PhC slab and manipulate each with great freedom. This method is used to explain the physical origins of the different line-shape

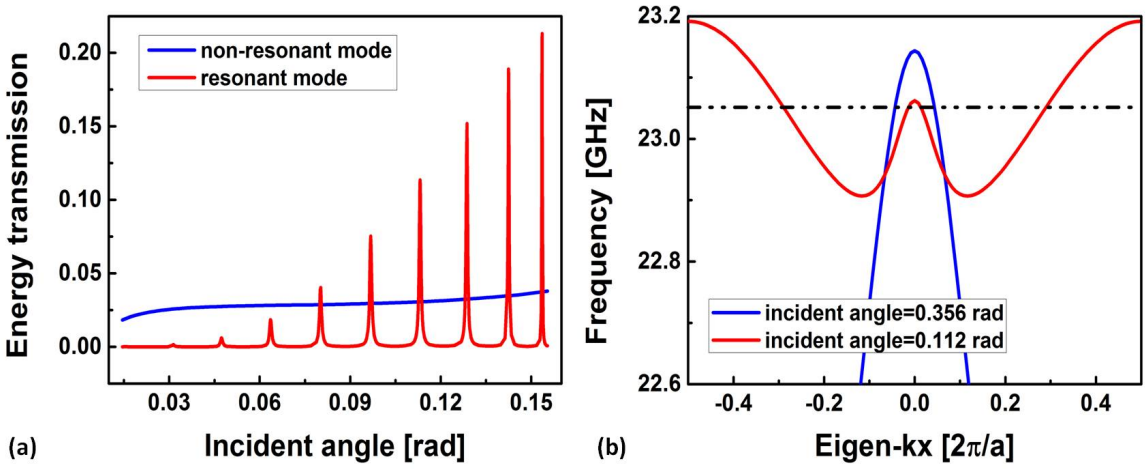

Figure 2.10 (a) Energy transmission of both Bloch modes in the small incident angle regime, ignoring the coupling between them. The blue curve corresponds to the steep-slope mode in Fig. 2.5 (c), while the red curve corresponds to the small-slope mode. (b) Dispersion relations of two excited modes with different incident angles. The black dashed-dot line marks the excitation frequency of 23.05161 GHz. Its intersection with the blue curve shows the propagating and counterpropagating Bloch waves excited at peak 11 in Fig. 2.5 (a). The intersection with the red curve shows the two Bloch modes and their counterpropagating parts at small incident angle with respect to peak 7 in Fig. 2.5 (a).

features in the transmission spectrum. In addition, our method allows to study the surface scattering of a truncated PhC by eliminating the back reflection, and will prove beneficial to understand the scattering properties of more complicated photonic crystal structure of final extent.

CHAPTER 3. OPTICAL FORCES INDUCED BY COUPLING OF SURFACE PLASMON POLARITONS OF GRAPHENE SHEETS

3.1 Introduction

Light-matter interactions exist in various forms and optical force is one of the most intuitive representations. Recently, researchers have been exploring the possibilities of utilizing optical force in micro- and nano-systems for a variety of practical applications, such as optical tweezers [30], controlling photonic circuits [31], etc. However, under many circumstances, the opto-mechanical effects are fairly inconspicuous due to weak light-matter interactions. Therefore, many efforts have been taken towards the enhancement of optical forces [32, 33, 34].

In this chapter, I first investigate the interaction (optical gradient force) between two graphene sheets, which may be adopted in micro- and nano-mechanic systems, and reveal such force originating from the coupled surface-plasmon-polariton (SPP) modes of graphene layers can be greatly enhanced with several orders stronger than that of regular parallel-waveguide system. Then in a cavity-like system with pre-curved graphene sheets, the potential configurations of deformation−mechanical states−under certain bending energy are explored. Arising from the strongly enhanced gradient force between graphene layers, the phenomena of mechanical state transitions are demonstrated, accompanied by abrupt changes in reflection and transmission spectra of the system.

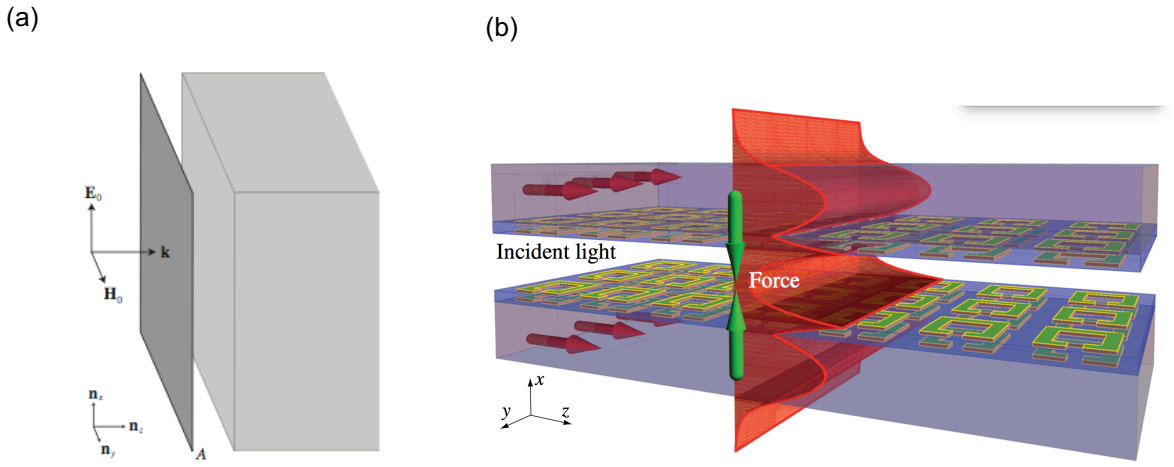

Figure 3.1 A sketch of the radiational force and the gradient force. (a) Light is reflected by the medium. The change in its wave vector results in radiational forces. Taken from Ref. [13] (b) Photons can transit between two adjacent waveguides, resulting in an attractive for repulsive force between the two waveguides. The direction of the force is the same as the energy gradient. Taken from Ref. [32]

3.1.1 Optical forces and Maxwell stress tensor

Forces come from momentum exchange. Depending on whether the transferred momentum is parallel or perpendicular to the wave propagation, one can divide the optical force into two categories: the radiational or scattering force, and the gradient force [13]. The radiational force is directly associated with the wave-vector of light and is interpreted as the momentum interchange between light and matter when the propagation path is altered due to the inhomogeneity of the space [35, 36]. The optical gradient force essentially refers to the gradient of field energy, which plays an important role in integrated optics, and has been intensively studied in coupled waveguide systems [31, 37, 38, 39, 40, 41, 42, 43, 44, 32]. Figure 3.1 (a) and (b) show the difference between the radiational force and gradient force.

Here I give a brief introduction how the optical forces can be calculated. Starting from the Lorentz force density that:

$$\vec{f} = \rho\vec{E} + \vec{J} \times \vec{B}, \tag{3.1}$$

and replacing ρ and $\vec{J}$ by the Maxwell equations, a symmetric form can be got as:

$$\vec{f} = \epsilon_0(\nabla \cdot \vec{E})\vec{E} + \frac{1}{\mu_0}(\nabla \cdot \vec{B})\vec{B} + \frac{1}{\mu_0}(\nabla \times \vec{B}) \times \vec{B} + \epsilon_0(\nabla \times \vec{E}) \times \vec{E} - \epsilon_0\frac{\partial}{\partial t}(\vec{E} \times \vec{B}). \tag{3.2}$$

Since for any vector $\vec{A}$, there is

$$\begin{aligned} &(\nabla \cdot \vec{A})\vec{A} + (\nabla \times \vec{A}) \times \vec{A} \\ =&(\nabla \cdot \vec{A})\vec{A} + (\vec{A} \cdot \nabla)\vec{A} - \frac{1}{2}\nabla A^2 \\ =&\nabla \cdot (\vec{A}\vec{A} - \frac{1}{2}\overleftrightarrow{I} A^2), \end{aligned} \tag{3.3}$$

where $\overleftrightarrow{I}$ is the unit rank-2 tensor. By substituting E and B, we finally reach:

$$\vec{f} + \frac{\partial}{\partial t}\vec{g} = \nabla \cdot \overleftrightarrow{T}, \tag{3.4}$$

where

$$\begin{aligned} \vec{g} &= \epsilon_0\vec{E} \times \vec{B}, \\ \overleftrightarrow{T} &= \epsilon_0\vec{E}\vec{E} + \frac{1}{\mu_0}\vec{B}\vec{B} - \frac{1}{2}\overleftrightarrow{I}(\epsilon_0 E^2 + \frac{1}{\mu_0}B^2), \end{aligned} \tag{3.5}$$

$\vec{g}$ is the momentum density of the electromagnetic field, and $\overleftrightarrow{T}$ is called the Maxwell stress tensor. By integrating both sides, we have

$$\int \vec{f} dV + \frac{d}{dt}\int \vec{g} dV = \int \nabla \cdot \overleftrightarrow{T} dV = \oint \hat{n} \cdot \overleftrightarrow{T} dS. \tag{3.6}$$

If we choose one oscillatory circle, the second term goes to zero, and the time averaged force can be simply expressed as the surface integral of the Maxwell stress tensor.

3.1.2 Surface plasmons of graphene

Graphene, a two dimensional (2D) material composed of one layer of carbon atoms in a honey comb lattice, has attracted intensive attention due to its unique properties in various aspects [45, 46]. In particular, graphene provides a new platform for

a variety of intriguing optoelectronic and opto-mechanical effects. The highly reactive electric response of graphene results in strongly localized plasmons residing within deep subwavelength region, which leads to a prosperous subfield named graphene plasmonics with plenty of promising applications ranging from terahertz (THz) to the infrared regime [47, 48, 49, 50]. In fact, the low carrier density of graphene on one hand leads to a high kinetic inductance and thus a much higher confinement than metals at low frequencies. On the other hand, it makes the graphene more sensitive to carrier density changes and more tunable in the electromagnetic properties when doping or a gate voltage is applied [51].

From the single electron approximation, and considering low temperature cases where $E_F << k_BT$, the surface conductivity can be written in the intraband part and an interband part:

$$\begin{aligned} \sigma_{intra} &= \frac{e^2 E_F}{\pi\hbar^2(\gamma - i\omega)}, \\ \sigma_{inter} &= \frac{e^2}{4\hbar}[\theta(\hbar\omega - 2E_F) + \frac{1}{pi} ln|\frac{2E_F - \hbar\omega}{2E_f + \hbar\omega}|]. \end{aligned} \tag{3.7}$$

Considering different dopings or gate voltages, the graphene layer can support either a TM surface plasmon polariton, or a TE one. The dispersion relations read

$$\begin{cases} k_{spp}^{TM} &= k_0\sqrt{1 - \frac{4\epsilon_0^2 c^2}{\sigma_s^2}} \\ k_{spp}^{TE} &= k_0\sqrt{1 - \frac{\mu_0^2\sigma_s^2 c^2}{4}} \end{cases}. \tag{3.8}$$

Figure 3.2 shows that how the optical properties such as transmission and absorption are tuned by applying gate voltages.

3.2 Enhanced optical forces

For two dielectric slab waveguides (thickness t), settled in parallel with separation d_w as shown in Fig. 3.3 (b), the tails of fields for guided modes interact with each other, introducing a force perpendicular to the propagation direction. Mimicking the case of

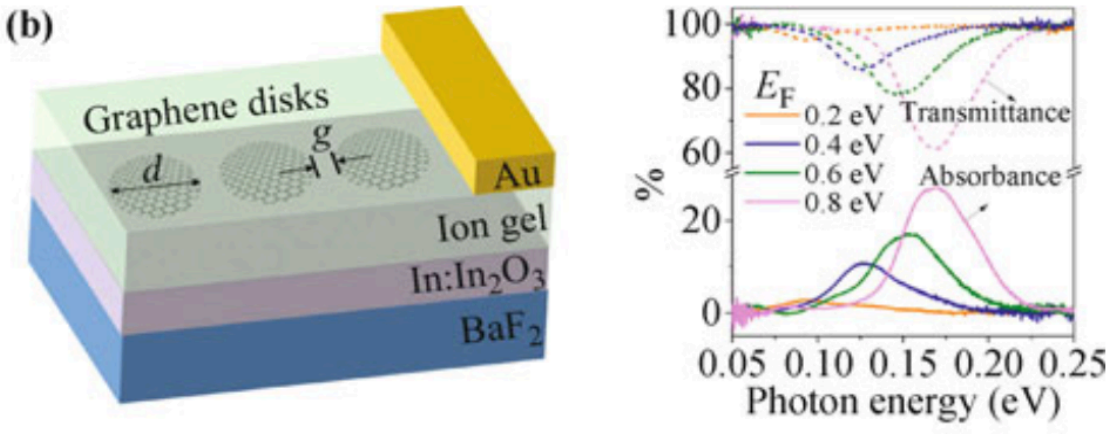

Figure 3.2 Applying different gate voltages on graphene, its opto-electronic properties can be tuned, giving rise to different absorption and transmission. Taken from Ref. [51].

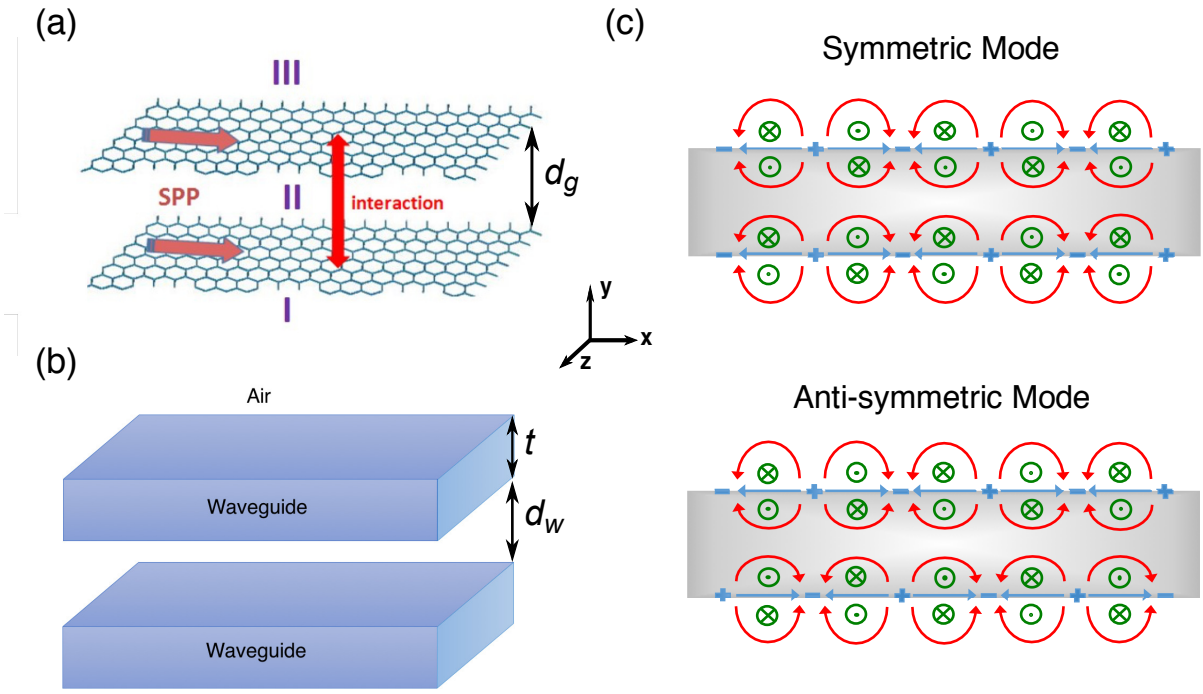

Figure 3.3 Schematic configurations of parallel graphene sheets (a) and parallel dielectric waveguides (b). Surface plasmons, propagating along x-direction either of symmetric or anti-symmetric mode (c), induce interaction between graphene sheets. Signs of "+" and "−" denote the oscillating surface charges. Straight and curved arrows show the directions of surface currents and electric fields, respectively. Circled cross and dot symbols indicate the magnetic fields.

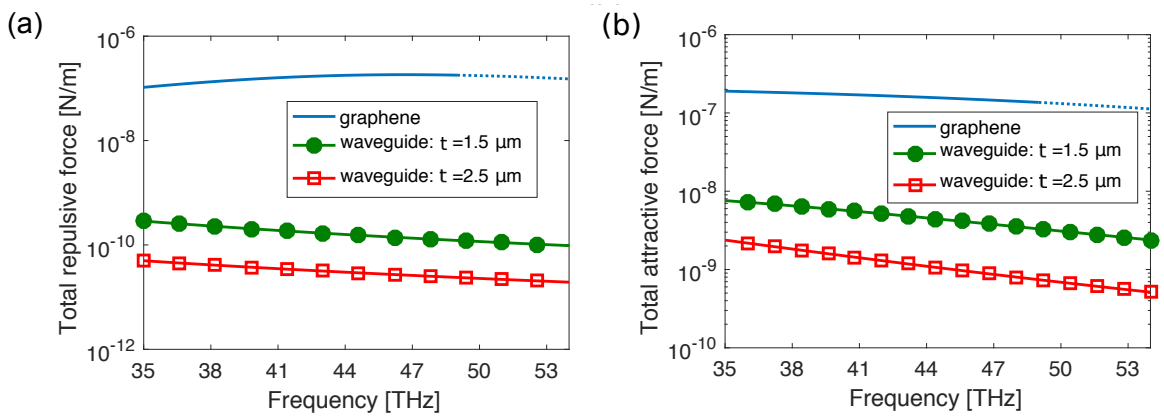

Figure 3.4 (a) Dispersion relations for SPP modes of parallel graphene sheets in comparison to TM modes of the parallel dielectric waveguides ($\epsilon_d = 3.8$) with $t = 1.5$ (left set in green) and 2.5 μm (right set in red). $d_g = d_w = 100$ nm. The case of light line (dash-dotted line) is set as reference. Solid (dashed) lines correspond to the symmetric (anti-symmetric) modes. The green (red) lines correspond to the modes in a pair of dielectric slabs with thickness of 1.5 μm (2.5 μm). (b) k_{SPP}-d_g dependency for parallel graphene sheets at 40.4 THz: symmetric (solid line) and anti-symmetric (dashed line) modes.

parallel-waveguide systems, here, the interaction between two graphene layers upon the excitation of SPP modes is considered, with the field decaying away from graphene at both sides [see Fig. 3.3 (a)]. It is noted that the coupled SPP modes can be classified as symmetric or antisymmetric, depending on the relative phase of surface currents or electromagnetic (EM) fields [see Fig. 3.3 (c)]. For uniform notation, the symmetry of the coupled SPP modes is denoted the same as surface currents throughout the paper, since the currents and fields may show opposite symmetry.

Figure 3.4 (a) shows the comparison of the dispersion relations for SPP modes of two coupled graphene sheets ($d_g = 100$ nm) and TM_0 modes (magnetic field H along z-direction) of two coupled slab waveguides ($d_w = 100$ nm) made from silicon with refractive index $n = 3.48$ [32]. For the parallel-waveguide configuration, two different thicknesses are considered, i.e., $t = 1.5$ and 2.5 μm, respectively. From Fig. 3.4 (a), the advantages of coupled graphene sheets mainly lie in two aspects: much better separated modes in dispersion relation imply a much stronger coupling effect between graphene

layers, and the settlement of modes much further away from the light line [dash-dotted line in Fig. 3.4 (a)] illustrates a stronger localization of SPPs, leading to a much larger field gradient in the ambient medium (air) and therefore the force as well. By setting the frequency 40.4 THz, it's shown in Fig. 3.4 (b) that the eigen values of the propagation constant of coupled SPP modes (k_{SPP}) dependent on the separation between graphene sheets d_g. When the two graphene layers are well separated, i.e., d_g is large enough, the coupling in-between can be neglected and correspondingly, the symmetric (solid line) and anti-symmetric (dashed line) modes are degenerate. As the separation d_g decreases, the interaction between graphene layers gets stronger and the degeneracy of SPP modes breaks eventually.

To provide an intuitive analysis to the gradient force in the aforementioned parallel-graphene-layer or parallel-waveguide system, both the graphene layers or waveguides as two adjacent finite potential wells are compared. Though light is confined on the graphene sheets or inside the waveguides, the quantum tunneling effect still allows the photons to transmit from one to the other, and it is such exchange of photons that leads to the gradient force. Assuming $U = N\hbar\omega$ representing the coupled EM field energy, where N is the number of photons, $\hbar$ the reduced Plank constant and ω the circular frequency of the EM wave, the induced gradient force can be expressed as follows [43]:

$$F = -\frac{\partial U}{\partial y} = -\frac{U}{\omega}\frac{\partial \omega}{\partial y}|_{k_{\mathrm{spp}}}. \tag{3.9}$$

It must be noted that ω, y and k_{SPP} are not independent, but tied with each other under the following dispersion relation of the coupled graphene SPPs (see Appendix C for detailed derivations):

$$\kappa(\pm e^{-\kappa d_g} - 1) = -i\frac{2\omega\epsilon_0}{\sigma_s}, \tag{3.10}$$

where $\kappa = (k_{\mathrm{spp}}^2 - k_0^2)^{1/2}$ denotes the decaying factor and σ_s is the surface conductivity of graphene. In the long wavelength and high doping limits under our consideration, the

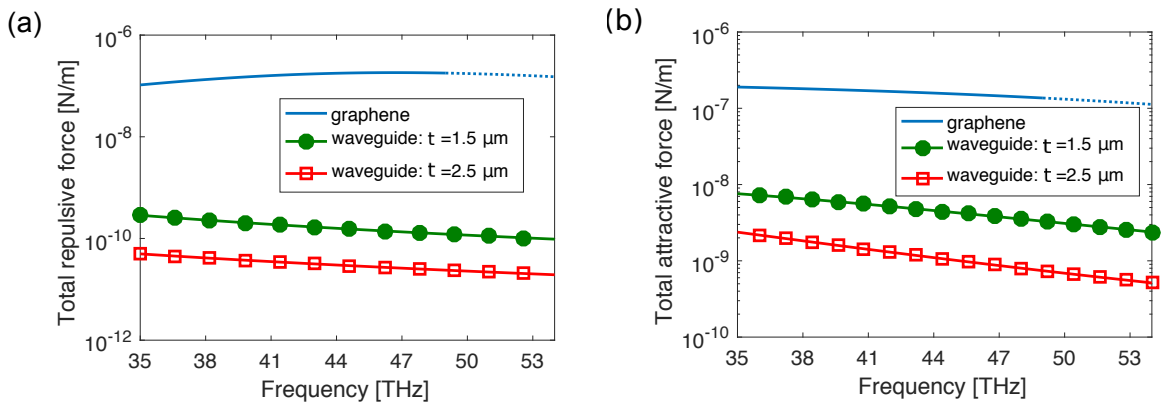

Figure 3.5 Comparisons of optical force for parallel-graphene-sheet and parallel-waveguide configurations with same separation 100 nm in-between: (a) repulsive force for symmetric mode; (b) attractive force for anti-symmetric mode. The input power is set as 1 W/m.

optical conductivity σ_s is dominated by the intra-band transitions, which follow the local Drude model expressed as [52]

$$\sigma_s(\omega) = \frac{e^2 E_F}{\pi\hbar^2(\tau^{-1} - i\omega)} = \frac{\alpha}{\gamma - i\omega}, \tag{3.11}$$

where e is electronic charge, E_F is doped Fermi level, $\gamma = \tau^{-1}$ is collision frequency with τ denoting the momentum relaxation time, and α so-called Drude weight. In our following calculations, we assume $\alpha = 7.6 \times 10^{10}$ $(\Omega s)^{-1}$ and $\gamma = 1.89$ THz as reported in Ref. [53].

From the implicit function theorem for differentiation of dependent variables [54], the gradient force F in Eqn. 3.9 can be rewritten in the form of

$$F = +\frac{U}{\omega}\frac{\partial\omega}{\partial k_{spp}}|_y \frac{\partial k_{spp}}{\partial y}|_\omega, \tag{3.12}$$

and qualitatively, it can be determined whether the force F is attractive (negative sign) or repulsive (positive sign) based on Fig. 3.4, i.e., antisymmetric (symmetric) mode corresponds to attractive (repulsive) force. We can also understand the nature of such a force in an intuitive view considering the oscillating charges. Take the symmetric-mode case as an example where both currents and charges are in phase, the in-phase currents

result in an attractive force while the charges with same sign will lead to a repulsive force. Therefore, a competition exists between the forces arising from the currents and charges, which determines the net force, and in our configuration of parallel graphene layers, the interaction of charges plays a dominant role.

Quantitatively, the time-averaged force between graphene layers can be calculated with Maxwell stress tensor $\overleftrightarrow{T}$ defined in Eqn. 3.5. Figure 3.5 shows the comparison of calculated forces (plotted with absolute values in log-scale) for the configurations of parallel graphene layers and parallel waveguides, where the separations in-between are set the same with $d_g = d_w = 100$ nm. Two different thicknesses, i.e., $t = 1.5$ and 2.5 μm, are considered for the parallel-waveguide case, and as expected, thinner slabs show a stronger force since the thicker the slabs, the stronger confinement of EM fields inside of waveguides but weaker fields outside leading to weaker interaction in between. From Fig. 3.5, the force between graphene layers can be several orders stronger than that is in the waveguide cases, and such a dramatic enhancement of interaction, originating from much larger field gradients in the ambient medium (see dispersion relations in Fig. 3.4 for a direct evidence), will be greatly beneficial for various practical applications in opto-mechanical systems. It also worth noting from Fig. 3.5 that the gradient optical force between graphene layers does not change monotonically with frequency. This can be understood qualitatively via the expression of the force $F \propto (\kappa^2/\omega^2)|B|^2 e^{-\kappa d_g}$, where B denotes the amplitude of the field between graphene layers (see Appendix C for detailed derivations). Therefore, the force is determined by two competitive aspects, i.e., κ, which represents the gradient of the field, and $|B|^2 e^{-\kappa d_g}$, which corresponds to the field strength at the evanescent tail. At low frequency side, the system has smaller k_{SPP} and correspondingly smaller κ [see Fig. 3.4 (a)], which means the EM field between layers is stronger but with lower gradient. Therefore, the strength of the field dominates over the gradient for the force at low frequencies. It is the opposite case for high frequencies, where the gradient of the field is large while with weak field strength. A trade-off does

exist leading to the strongest force. It is noted that the force of parallel graphene layers at frequencies over 50 THz are marked with dotted line in Fig. 3.5, since the actual force would be smaller due to extra losses induced by phonon-electron interactions.

3.3 Mechanical state transitions from the force

In the last section, it's been demonstrated that a SPP-induced significant force enhancement between parallel graphene layers in the infrared regime, i.e., several orders stronger than that is between parallel waveguides. In addition, graphene has been shown to possess superior mechanic properties, such as strong in-plane stiffness with measured Young's modulus as high as 1 TPa [55], several orders larger than that of conventional materials. Considering its extremely small mass density as a 2D material, graphene therefore provides a great opportunity in force sensing and many other practical applications [56, 57, 58, 59]. Therefore, the introduction of graphene in micro- or nano-systems is believed to bring various interesting opto-mechanic effects. As well known, from classical mechanics, a thin plate can be bent if a force or torque is exerted. In this Section, a conceptual configuration with two graphene layers settled closely with each other will be constructed and the deflections of graphene sheets even the possibilities of mechanic-state variations will be explored, for it shall provide solid physical foundations and guidances towards various practical applications in opto-mechanics.

3.3.1 Mechanical energy of graphene sheets

In classic elastic mechanics, Kirchhoff theory is the one being used to describe the bending of a thin plate. Under circumstances where only the transverse load is applied (no external in-plane forces), the deformation of this thin plate is governed by:

$$\nabla^2\nabla^2 w = -\frac{q}{D}, \tag{3.13}$$

where q is the distribution of transverse load, and D is a material-dependent parameter, called bending stiffness and is related to the bulk Young's modulus E, plate thickness h, and poisson ratio ν, represented as $D = 2Eh^3/3(1-\nu^2)$ [60]. The relation between D and E comes from the fact that during a pure bending where middle plane of the plate keeps its original length, the planes above and below the middle plane are stretched and compressed respectively. Figure 3.6 gives a sketch of the process. It is intuitive that when the elastic modulus of the plate is stronger, or when the thickness of the plate is larger, the bending energy under certain deflection will be larger, making it harder to bend.

In contrast, graphene, as a 2D material, has no well-defined thickness, and there is no well-defined middle plane. Therefore there is a different origin of rigidity corresponding to free bending of graphene sheets, i.e., instead of any stretch or compression. In presence, the bending energy of graphene arises from the rotation of C-C bonds since the sp^2 hybridization tends to keep the carbon atoms in plane, and accordingly, the Kirchhoff theory for classical thin plates no longer holds [61]. Theoretically, the bending modulus D can be obtained from $ab-initio$ calculations, and the most commonly taken value is 0.192 nN $\cdot$ nm [62, 63, 56, 64, 65, 66]. In this work, a phenomenological model is adopted to investigate the bending of graphene sheets. Under small deformations, the linear model applies: $F = F_b + F_s$ with F_s in-plane stretch energy and the pure bending energy $F_b = \int \frac{1}{2} D\kappa^2 \, ds$ [61], respectively, where $\kappa \sim y''/(1+y'^2)^{3/2}$ denotes the curvature of the bent graphene sheet. By minimizing the total energy, one can get a stable y(x) – the deflection distribution along graphene.

3.3.2 Mechanical state transitions

Figure 3.7 shows the schematic setup, in which two graphene layers with the separation $d_g = 100$ nm are embedded in some dielectric medium (ϵ_d is taken as 3.8) at two sides. The distance between two side dielectric blocks, s, is 1 μm, while the length of

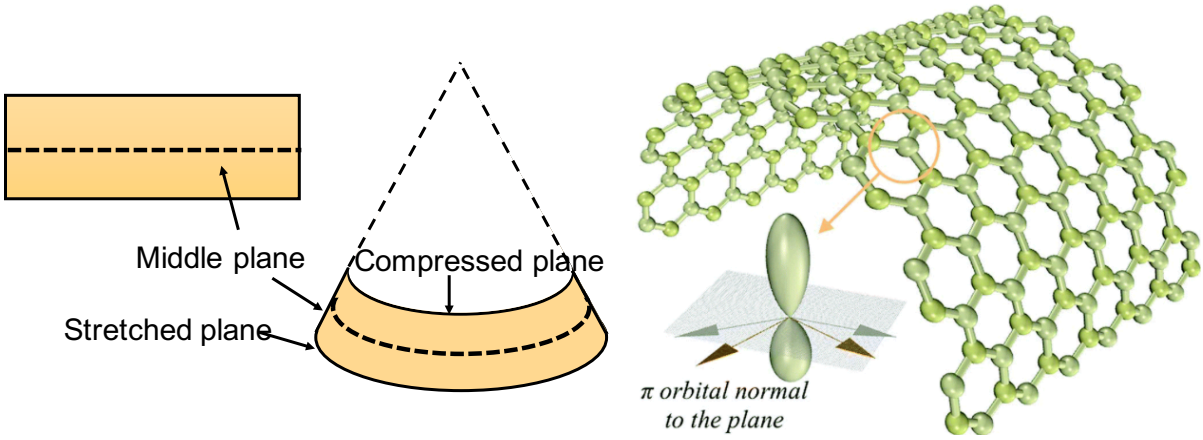

Figure 3.6 Schematic configuration (a) bent thin plate and (b) bent graphene sheet. The bending energy of the thin plate comes from the stretch and compression of planes with respect to the middle plane. The bending energy of graphene sheet origates from the chemical bonds between carbon-carbon atoms tending to keep everything in plane.

graphene sheets in-between is assumed to be 1.004 μm, so that the graphene layers are in curved status for demonstrating opto-mechanical deflections and different shapes of graphene sheets correspond to different mechanical energy states. Intuitively, the lowest state, denoted as ground state, should have a cosine-like shape with only one antinode, the first meta-stable state will correspond to a sine-like shape with two antinodes, and higher order states possess certain number of antinodes. Assuming the parallel graphene sheets sit at the ground state initially, they may be in either of concave [Fig. 3.7 (a)] and convex [Fig. 3.7 (b)] configurations, which are degenerate without external force. In case of some force being applied to the system, such a degeneracy will be broken and one configuration experiences lower energy than the other. Therefore, an optical-gradient-force-induced mechanical state transition may be achieved.

In Fig. 3.7 (a), the two graphene sheets are initially in the concave configuration, to which the symmetric SPP mode with certain power is injected from one side leading to a repulsive force between graphene sheets. Upon the increase of the input power, the force gets stronger accordingly, and at some threshold point, the graphene sheets get

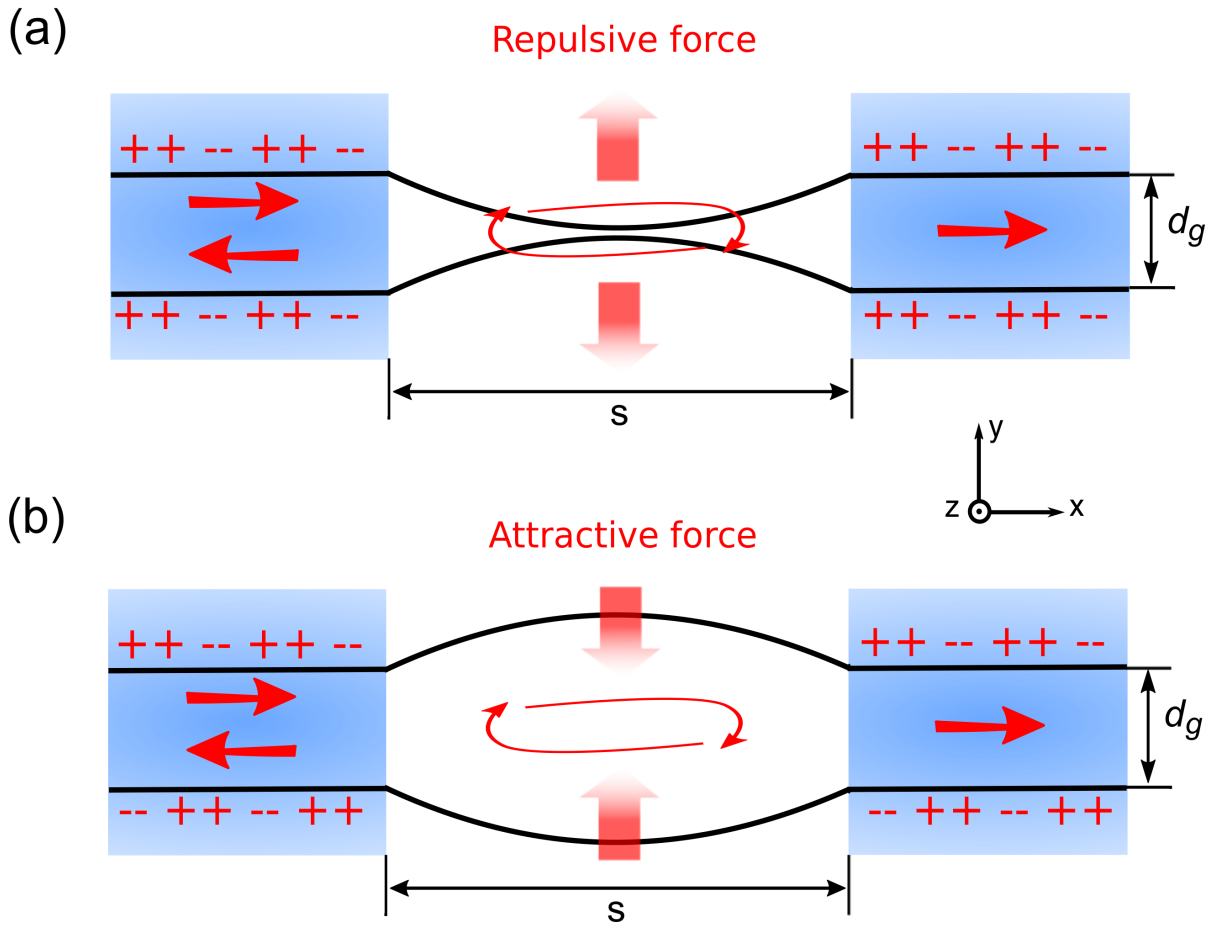

Figure 3.7 Schematic configuration of constructed system for demonstrating optical–force-induced mechanic state transitions of graphene sheets: (a) Initial state of concave configuration with symmetric mode injection; (b) Initial state of convex configuration with anti-symmetric mode injection. Graphene layers are embedded in dielectric medium at two sides ($s = 1$ μm) with pre-curved shape in between (length 1.004 μm).

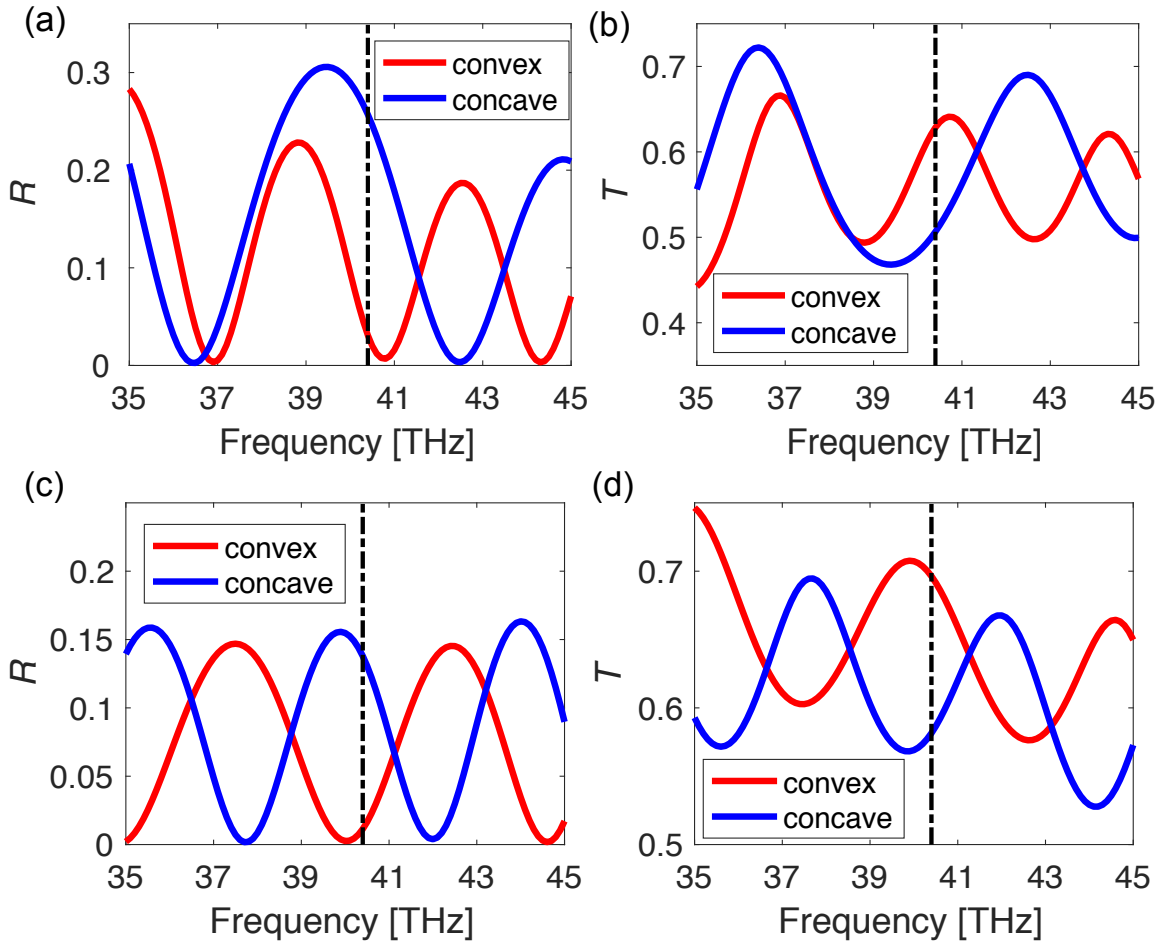

Figure 3.8 Calculated reflection (**R**) and transmission (**T**) spectra for concave (blue dark line) and convex (red light line) configurations of graphene sheets under symmetric [(a) and (b)] and anti-symmetric [(c) and (d)] SPP modes. Dash dotted lines correspond to the frequency 40.4 THz, where significant contrast in **R** and **T** exists between the concave and convex configurations.

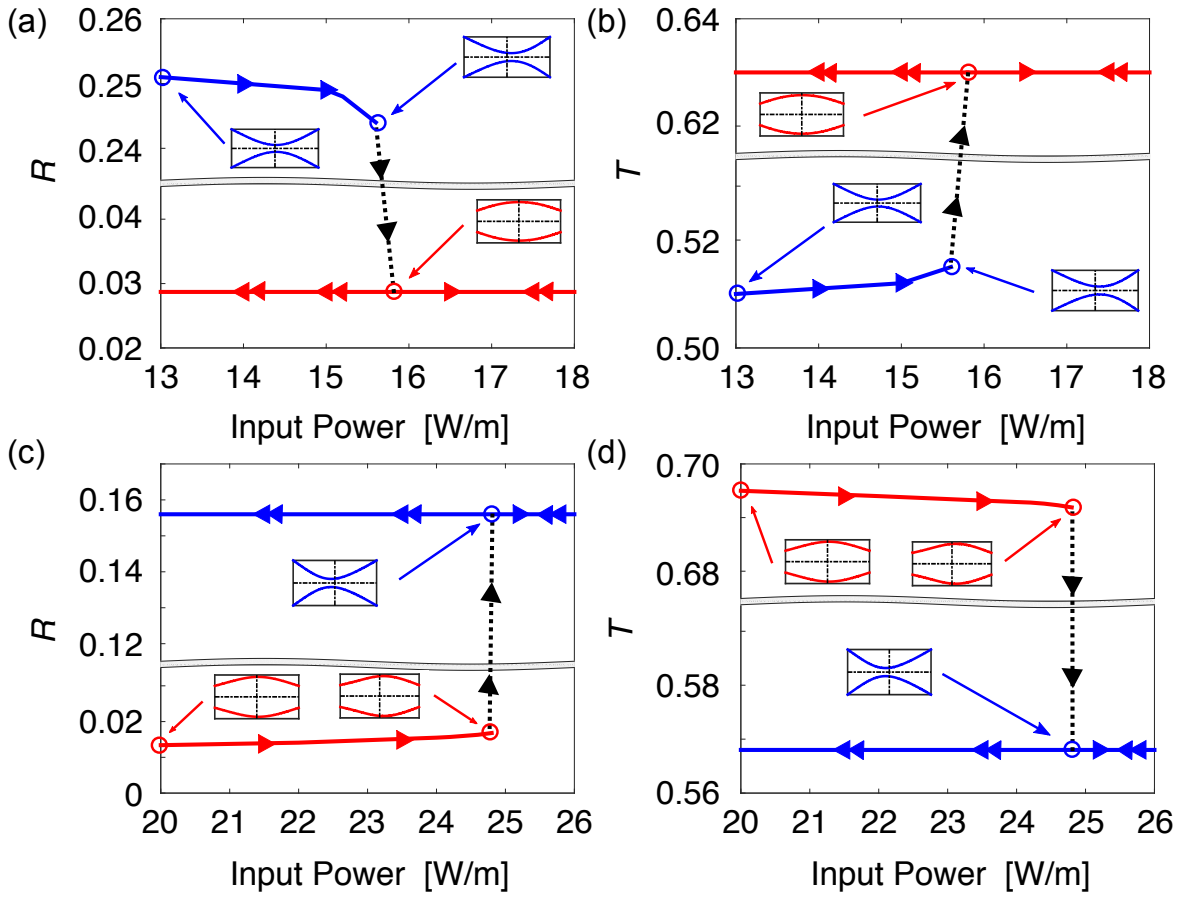

Figure 3.9 Monitored **R** and **T** dependent on the input power showing the processes of mechanic state transitions: (a) symmetric mode and (b) anti-symmetric mode. Single arrows mark the direction of the transition path from initial state towards final state upon the increase of input power, while double arrows indicate the final state does not vary when the input power gets decreased.

flipped and reach the state of convex configuration. It should be noted that, as long as the graphene sheets flip over, the effective gap in-between changes and the eigenvalue of the propagation constant of the coupled SPPs also changes accordingly. In the EM view, the two side dielectric blocks naturally form a Fabry-Pérot (FP) cavity in-between for SPP waves of graphene, and the transmission (**T**) and reflection (**R**) of the system may vary dramatically upon the shape change of graphene sheets, providing an excellent and straightforward strategy of monitoring the mechanical state transition macroscopically.

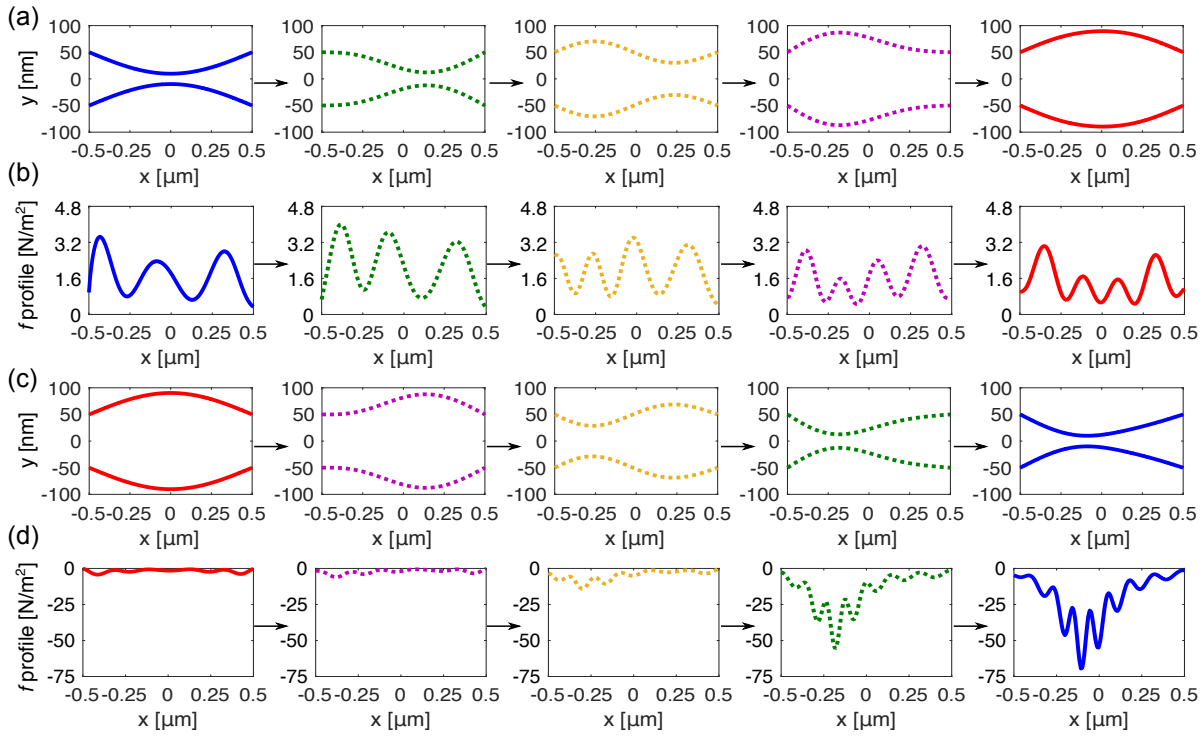

Figure 3.10 Variation of geometric-configuration and force-density profiles for graphene sheets from initial state to final state under symmetric mode [(a) and (b)] and anti-symmetric mode [(c) and (d)], respectively. The three intermediate cases (dotted lines) are not meta-stable states but only indicate the process of mechanic state transition being reached. The input power is taken with the threshold value, i.e., 15.8 W/m and 25 W/m for symmetric and anti-symmetric mode, respectively.

A self-consistent iterative method to find the corresponding deformations of the graphene sheets is applied. Considering the optical force is fairly small compared to the strong in-plane modulus of graphene, it is assumed that no in-plane stretch or compression happens, implying a constraint of the length of graphene sheets in the cavity being kept as 1.004 μm. Therefore, the problem of finding the shape configurations for graphene sheets turns out to be optimizing the energy function for local minimum under

the length constraint. Under external fields, the bending energy density function can be written as follows in the form of deformation:

$$\begin{aligned} F[w(x)] &= \int \frac{1}{2} D\kappa^2 \, ds - \int f_{\text{optical}} dx \\ &= \frac{1}{2} D \int dx \, [w''(x)^2 \, (1 + w'(x)^2)^{-\frac{5}{2}}] - \int dx \cdot \Delta w[x] \cdot f_{\text{optical}}[w(x)], \end{aligned} \tag{3.14}$$

where the energy density F, in unit of J/m, represents the total energy per unit length in z-direction of graphene, and $w[x]$ is the function of deformation with respect to the coordination along x-direction. Technically, to figure out the local minimum of the energy function, the "steepest decent" method [67] is utilized by performing Fourier expansions to the deformation function $w(x)$ and applying the optical force of the initial configuration. As long as a new configuration of deformation is reached, the corresponding optical gradient force of the graphene system is calculated and substituted into the energy function for another round of optimization. Iterations continue until the deformation configuration does not change reaching a converged and final state (see Appendix D for detailed information). A flow chart as in Fig. 3.11 can help understand the whole process.

As stated in the above, one can monitor the mechanical deformation of graphene sheets via the propagation properties of EM waves ($\mathbf{R}$ and $\mathbf{T}$) in the system. For a better contrast in $\mathbf{R}$ and $\mathbf{T}$ spectra between the concave and convex configurations (see Fig. 3.8), some demonstration frequency can be chosen accordingly and it it set to be 40.4 THz, at which, the concave (convex) configuration has $\mathbf{R} = 25.1\%$ (2.9%) and $\mathbf{T} = 51.0\%$ (63.0%) under symmetric SPP modes while $\mathbf{R} = 13.8\%$ (1.3%) and $\mathbf{T} = 58.0\%$ (69.4%) for anti-symmetric SPP modes, respectively.

Figure 3.9 shows the processes of mechanic state transitions with the dependence of input powers, calculated via the previously described iterative method. Figures 3.9 (a) and (b) correspond to the case with symmetric SPP modes injection in graphene sheets. For the initial state being the concave configuration, the increase of the input power (the path is marked with single arrows) leads to slight deformations initially, but abrupt

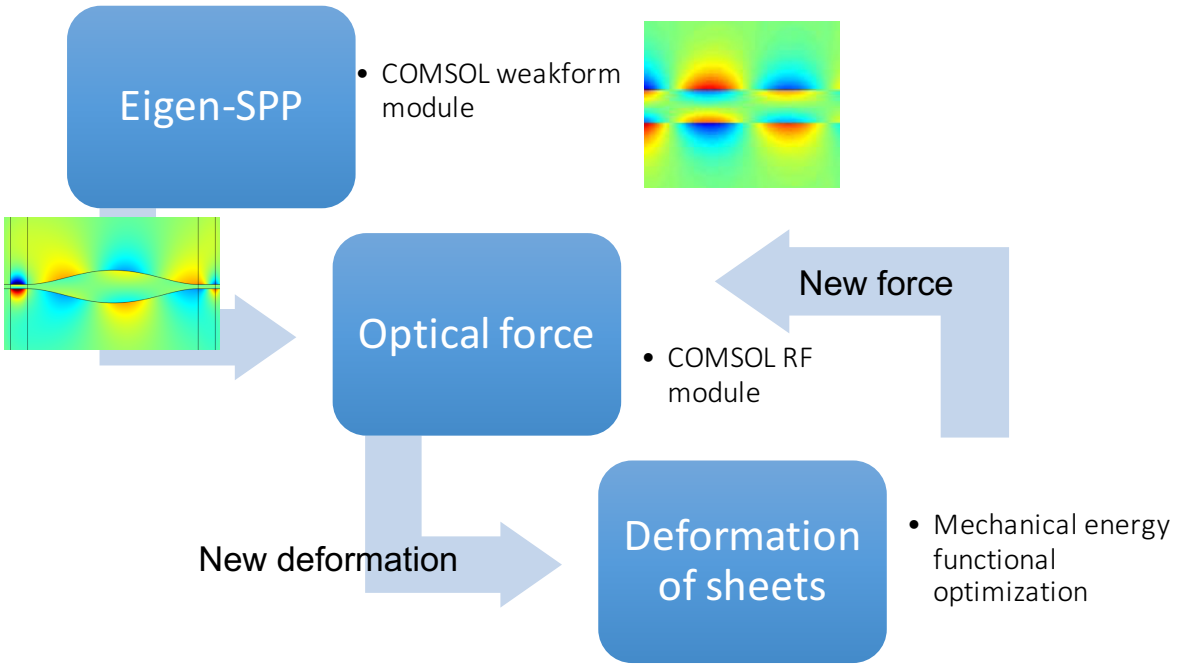

Figure 3.11 The flow chart of the self-consistent calculation. First, The eigen-mode of SPP (either symmetric or anti-symmetric) is calculated, and imported into the optical force simulation as the injected waves. Second, the optical force is calculate under certain injection and exported into the deformation calculation. The whole process of deforming is continously however we discretize that by monitoring deformation every few steps. Third, as long as the deformation of graphene sheets changes, the force in-between will also change, so we import the new deformation back into the optical force simulation and do that recursively until the final results converges.

changes in $\mathbf{R}$ and $\mathbf{T}$ spectra happen at the input power being 15.8 W/m, the threshold for the mechanical state transition, where the graphene sheets flip to the convex configuration. Upon the decrease of input power for the convex configuration, the repulsive force induced by symmetric SPP modes keeps the graphene configuration and there is no change in $\mathbf{R}$ or $\mathbf{T}$ [see Figs. 3.9 (a) and (b)], consistent with our intuitive expectations. Figures 3.9 (c) and (d) show the case of anti-symmetric SPP modes injection with attractive gradient force between graphene sheets: Starting from the convex configuration, the increase of input power (direction along single arrows) induces some slight deformations to graphene sheets initially, and the mechanic state transition occurs at 25.0 W/m, with

the evidence of abrupt changes in **R** and **T** spectra. It should be noted that **R** and **T** of the final state in Figs. 3.9 (c) and (d) are to-some-extent different from those values calculated for the concave ground state, which means such a final state is not exactly the ground state and may be called as a pseudo concave configuration. This will be further explained by working out the transition path and the corresponding force density profiles shown in Fig. 3.10. The same as the case of symmetric SPP modes, upon the decrease of input power from the pseudo concave configuration, the shape of graphene sheets does not change with constant **R** and **T**, marked with double arrows in Fig. 3.9 (c) and (d).

The geometric-deformation and force-density profiles in Figs. 3.10 (a) and (b) show how the mechanic state of the graphene sheets transits from the concave configuration to the convex one upon the threshold input power [transition window marked with dotted lines in Figs. 3.9 (a) and (b)]. The induced gradient force is stronger at the injection side (left), so the shape of graphene sheets starts changing from left and reaches the final state by experiencing two-antinode profiles. It is noted that the three middle profiles (marked in dotted lines) do not correspond to any meta-stable state, but are obtained in our iterative procedure only for illustrating the instant transition path near the threshold point. The mechanic transition for anti-symmetric SPP mode behaves similarly, whose geometric-deformation and force-density profiles neighboring the threshold are presented in Figs. 3.10 (c) and (d), i.e., the graphene sheets have their left parts dragged firstly due to stronger repulsive force induced at the injection side and transit to a final concave state experiencing some two-antinode profiles as well. However, due to the strong but asymmetric repulsive force, the final concave state is not symmetric but slightly bias to the left, showing **R** and **T** different from those are in the symmetric concave "ground state". In addition, it should be pointed out that, along the transition path (marked with single arrows in Fig. 3.9), any point on the solid lines corresponds to a meta-stable state, i.e., before reaching the transition point, switching-off the input power leads the

graphene sheets back to the initial state, and beyond the threshold, the release of the force will keep the configuration of graphene sheets staying as the new state.

3.4 Conclusion

In conclusion, this work showed a significant enhancement of optical gradient force between graphene sheets induced by coupled surface plasmon polaritons. Such a force can be several orders stronger than that exists between regular dielectric waveguides, and definitely will open up new avenues for efficient control of micro- and nano-components in opto-mechanical systems. As one of the fundamental phenomena, the optical-force-induced mechanic-state transitions for curved neighboring graphene sheets was demonstrated, can could be intuitively characterized via electromagnetic spectra measurements in a constructed cavity-like system. Therefore it will be greatly beneficial for the exploration of various new opto-mechanical devices integrated with graphene, such as force sensors, actuators, optical switches, etc.

CHAPTER 4. LATERAL FORCES ON CHIRAL PARTICLES ARISING FROM THE SPIN ANGULAR MOMENTUM OF LIGHT

4.1 Introduction

4.1.1 Spin angular momentum of light

Spin of electrons was first proven experimentally by the well known Stern-Galarch experiment, in which a beam of silver atoms bifurcate into two discrete lines on the reception screen while traveling through inhomogeneous magnetic fields, indicating the existence of an extra freedom of angular momenta. Spin is a pure quantum concept and an intrinsic property of particles without any classical counterparts. It is unrelated to spatial coordinates and the specific frame that is chosen, in contrast to the orbital angular momentum. The best mathematical tool to describe spin and angular momentum is the group theory, in which the spin of electrons is classified as the SU(2) group. Similarly to electrons, photons as bosons also possess spin angular momenta. In free space, they have spin eigen-values as $\pm\hbar$, while the 0 value is forbidden due to its massless nature. Large number of photons make up electromagnetic waves, in which the polarization plays a role similar to spin.

Considering an electromagnetic wave under Columb gauge $\nabla \cdot \vec{A} = 0$ where $\vec{A}$ is the vector potential, the electric and magnetic field can be expressed as:

$$\begin{aligned} \vec{E} &= -\frac{\partial}{\partial t}\vec{A}, \\ \vec{B} &= \nabla \times \vec{A}, \end{aligned} \tag{4.1}$$

and the linear momentum and total angular momentum densities are:

$$\begin{aligned} \vec{g} &= \vec{E} \times \vec{B}, \\ \vec{j} &= \vec{r} \times (\vec{E} \times \vec{B}). \end{aligned} \tag{4.2}$$

Then the total angular momentum will be:

$$\vec{J} = \int \vec{j} dV = \vec{L} + \vec{S}, \tag{4.3}$$

where

$$\begin{aligned} \vec{L} &= \int E_i (\vec{r} \times \nabla) A_i dV, \\ \vec{S} &= \int (\vec{E} \times \vec{A}) dV. \end{aligned} \tag{4.4}$$

The $\vec{L}$ term is coordinate dependent and $(\vec{r} \times \vec{\nabla})$ takes the same matrix representation as a spin-1 particle, while the $\vec{S}$ term is coordinate independent. For this reason, researchers associate $\vec{L}$ with the orbital part, while $\vec{S}$ with the spin part of the total angular momentum. Nevertheless it's of argument whether this separation is physical or not. It was first shown by S. Enk *et al* [68] and S. Barnett [69] that the separation of $\vec{J}$ into $\vec{L}$ and $\vec{S}$ can produce physically measurable quantities – in other words, both $\vec{L}$ and $\vec{L}$ are observables in a quantum mechanical sense. However, neither of them are true angular momenta since their quantized forms do not meet the general commutation rule as an angular momentum should be. Classically they are not generators of rotations as well. Further more, to satisfy electro-magnetic dual symmetry ($\vec{E} \to \vec{B}$ and $\vec{B} \to -\vec{E}$ makes Maxwell equations unchanged), S. Barnett suggested the spin part $\vec{S}$ should take the following form:

$$\vec{S} = \int \frac{1}{2}(\vec{E} \times \vec{A} + \vec{B} \times \vec{C})dV, \tag{4.5}$$

where $\vec{C}$ is a virtual vector potential for the electric field:

$$\begin{aligned} \vec{E} &= -\nabla \times \vec{C}, \\ \vec{B} &= -\frac{\partial}{\partial t}\vec{C}. \end{aligned} \tag{4.6}$$

In the monochromatic case, $\vec{E} = i\omega\vec{A}$ and $\vec{B} = i\omega\vec{C}$. Then the time averaged spin angular momentum can be redefined merely by the electric field and the magnetic field, which gives more computational convenience, reading as:

$$\begin{aligned} \vec{s} &= \vec{s}_e + \vec{s}_m, \\ < \vec{s}_e > &= \frac{1}{4\omega}\mathrm{Im}[\frac{1}{\mu}\vec{E}^* \times \vec{E}], \\ < \vec{s}_m > &= \frac{1}{4\omega}\mathrm{Im}[\frac{1}{\epsilon}\vec{H}^* \times \vec{H}]. \end{aligned} \tag{4.7}$$

In short, I put aside the argument of the naming the spin for a classical electromagnetic wave since it's beyond the main topic of this chapter, but just follow the historic convention and refer to $\vec{S}$ ($\vec{s}$) as the spin angular momentum (density) of light throughout the following text.

4.1.2 Transverse spin of evanescent waves

The spin angular momentum aforementioned though not a true angular momentum, can been seen as the rotation of the polarization, either in E-field or in H-field. Considering a plane wave propagating along the x-direction, there is:

$$\begin{aligned} \vec{E} &= (\hat{y} + m\hat{z})e^{ikx}, \\ \vec{s}_e &= \hat{x}\frac{\mathrm{Im}(m)}{2\omega}. \end{aligned} \tag{4.8}$$

For linear polarization, m is purely real, and $\vec{s}_e$=0. For circular or elliptical polarizations where Im(m) is non-zero, the spin angular momentum density is in the x-direction, parallel to the wavevector.

Now considering an evanescent wave, which propagates along the x-direction and decays in the z-direction:

$$\begin{aligned} \vec{E} &= (\hat{x} + m_y\hat{y} + m_z\hat{z})e^{ik_x x - \kappa z}, \\ \vec{s}_e &= \frac{1}{2\omega}[\mathrm{Im}(m_y^* m_z)\hat{x} - \mathrm{Im}(m_z)\hat{y} + \mathrm{Im}(m_y)\hat{z}]. \end{aligned} \tag{4.9}$$

It is apparent that as long as the m_z is not purely real, there will be a transverse direction of the spin angular momentum. And this is one of the reason that evanescent waves can couple with chiral particles and induce lateral forces. Figure 4.1 shows the field distribution H_z of a certain material. The black arrows denote the direction of the momentum density, which rotates in plane. The transverse spin points out of plane. A more complete analysis of the transverse spin of evanescent waves can be found in Ref. [70].

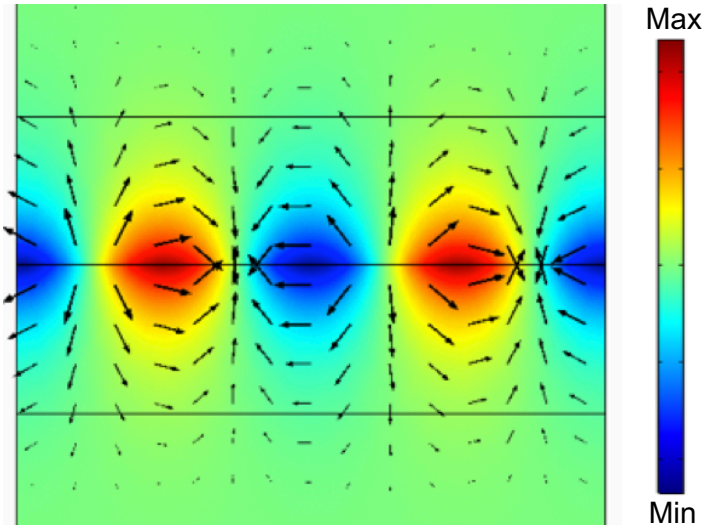

Figure 4.1 Magnetic field plot out of plane for a TM SPP. Black arrows denote the direction of linear momentum density.

4.1.3 Origin of the lateral force

In Chapter 3, it's been shown that the interaction between incoming electromagnetic waves and electrons (either free or bounded) in materials brings about the so called

optical forces. Under the dipole approximation, the force either comes from the transfer between kinetic momentum of the mono-electromagnetic waves (Poynting vector), or the gradient of the field intensity. Based on this difference in nature, they are classified into radiational (or scattering) force, and gradient force. However, the dipole approximation in Chapter 3 is actually a first-order approximation merely containing the interaction between external fields and the induced particle dipoles. By expanding the stress tensor with scattered field formulation, one can estimate the next order term, which is a dipole-dipole interaction.

Starting from the Maxwell stress tensor again,

$$< \vec{F} >= \int_S < \vec{T} > dS \tag{4.10}$$

where $< \vec{T} >$ is the time averaged normal component of the Maxwell stress tensor to the surface, defined as:

$$< \vec{T} >= \frac{1}{2}\mathrm{Re}[(\epsilon\vec{E}\cdot\hat{n})\vec{E}^* + (\mu\vec{H}\cdot\hat{n})\vec{H}^* - \frac{1}{2}(\epsilon|E|^2 + \mu|H|^2)\hat{n}]. \tag{4.11}$$

In a scattering problem, it is common that we write the total field in terms of a background field (incident wave) and a scattered field as $\vec{E} = \vec{E}_b + \vec{E}_{sc}$, and under the dipole approximation where the size of the scatterer is much smaller than the wavelength, the incident field can be expanded into a Taylor series:

$$\vec{E}_b(\vec{r}) = \vec{E}_b(0) + r(\hat{r}\cdot\nabla)\vec{E}_b + o(\vec{r}), \tag{4.12}$$

and the same for magnetic fields. Substituting into Eqn. 4.10 and noting that the scattered field $\vec{E}_{sc}$ is the radiational field by an electric dipole $\vec{p}$ and a magnetic dipole $\vec{m}$ whose form can be found in Ref. [71] as:

$$\begin{aligned}
\vec{E}_{sc}(\vec{r}) &= e^{ikr}\{[3\hat{r}(\hat{r}\cdot\vec{p}) - \vec{p}](\frac{1}{r^3} - \frac{ik}{r^2}) + \frac{k^2}{r}(\hat{r}\times\vec{p})\times\hat{r} - k^2(\hat{r}\times\vec{m})(\frac{1}{r} + \frac{i}{kr^2})\},\\
\vec{H}_{sc}(\vec{r}) &= e^{ikr}\{[3\hat{r}(\hat{r}\cdot\vec{m}) - \vec{m}](\frac{1}{r^3} - \frac{ik}{r^2}) + \frac{k^2}{r}(\hat{r}\times\vec{m})\times\hat{r} - k^2(\hat{r}\times\vec{p})(\frac{1}{r} + \frac{i}{kr^2})\}.
\end{aligned} \tag{4.13}$$

The total force will be the sum of three parts: $\vec{F} = \vec{F}^0 + \vec{F}^{mix} + \vec{F}^{pm}$. The first term $\vec{F}_0$ only contains the incident field with a surface integral to be zero. The second term is a mixture of the incident field and induced dipoles, written as:

$$F_i^{mix} = p_j \partial_i E_j^* + m_j \partial_i B_j^*. \tag{4.14}$$

This term is interpreted as the interaction between the external field and the particles. The traditional optical force, as mentioned, including the radiational force and gradient force can be further derived from the dipole-field interaction term. What's of interest is the last term, which involves the electrical dipole and magnetic dipole and takes form of:

$$F_i^{pm} = -\frac{k^4}{6\pi\epsilon_0 c}\epsilon_{ijk} p_j m_k^*. \tag{4.15}$$

This term indicates that an additional force appears due to the self interaction. When an electrical dipole and a magnetic dipole are induced simultaneously, their radiational field may interfere with each other and results in an asymmetric net far field pattern giving rise to a recoil force. This force may have a component, which is neither to the direction of the incoming poynting vector, nor to the direction of the energy gradient, and is thus referred to as lateral forces. This force is interesting because it is closely related to the chirality of the scatterer, and the spin angular momentum of the electromagnetic waves [72, 73, 74]. Exploring the lateral force promises people a bright future for chiral particle sorting using optical methods.

4.2 Laterial forces on particles

4.2.1 Interaction with non-chiral particles

Assuming a small particle is imposed under the illumination of an incident electromagnetic wave which propagates along the x-direction. According to the dipole-dipole interaction, the lateral force F_y might appear if an electric dipole p_z and a magnetic dipole m_x are excited simultaneously due to $\vec{F} \sim \vec{p} \times \vec{m}^*$. This could be achieved first

without introducing any chirality. Recalling the simplest split ring structure (SRR) lying parallel to the yz-plane [75], a plane wave propagates along x-direction and incides normal to the SRR. As shown in Fig. 4.2 (a), the SRR is made of gold, with permittivity $\epsilon = 3.7 - f_p^2/(f_0^2 - jf_0f_t)$, where f_p=2175 THz and f_t=6.5 THz. Since the real SRR has a finite thickness, it may have a current distribution along the edge resulting in some diamagnetic effects. To avoid this diamagnetic effect, a line current model is taken to simulate the real structure by shrinking the 50 nm thick SRR into a pure line sitting in the xz-plane as shown in Fig. 4.2 (b). The line conductivity is modeled from the bulk conductivity by multiplying the cross section area $\sigma_{\text{line}} = A_{\text{eff}} \cdot \sigma_{\text{bulk}}$.

Figure 4.2 (c) shows the lateral force calculation under the illumination of a z-polarized plane wave as $\vec{E} = \hat{z}E_0\exp(ik_x x)$. The red line is the numerical integration of the Maxwell stress tensor over an enclosed surface, while the blue dots are analytical results taking from the vectorial multiplication of electric dipoles and magnetic dipoles. Forces calculated are normalized by the time-averaged local energy flow density $1/2\text{Re}[\vec{E}(r_0) \times \vec{H}(r_0)]$. The electric dipole and magnetic dipole are taken from the simulation using the relations below:

$$\begin{aligned} \vec{p} &= \int (\vec{D} - \epsilon_0\vec{E})dV, \\ \vec{m} &= \frac{j\omega}{2}\int \vec{r} \times (\vec{D} - \epsilon_0\vec{E})dV. \end{aligned} \tag{4.16}$$

The peak of the lateral force around 53 THz is due to the excitation of the fundamental resonant mode of SRR, in which the current flows from one end of the gap to the other. The total current loop features a total effective electric dipole pointing in the z-direction, and a total effective magnetic dipole moment pointing in the x-direction. It is the self interaction between p_z and m_x that gives rise to the lateral force F_y. In this way, it can be concluded that an anisotropic particle could induce lateral force, though it might be small.

One may also notice the discrepancy between the analytic and the numerical results. Strictly, the definition of magnetic momentum in Eqn. 4.16 requires a continuity condi-

tion for current [76], while the existence of the gap of the SRR naturally breaks that. Thus it is not a pure/ideal magnetic momentum anymore. When the size of the gap becomes smaller, the disagreement between the numerical and analytic results will be relieved.

Figure 4.3 (a) & (b) plot the magnitude of calculated electric and magnetic dipole moments and Fig. 4.3 (c) & (d) plot the phases. As clearly shown, the z-component of the electric dipole and the x-component of the magnetic dipole makes a difference, and the magnetic dipole shifts $\pi/2$ in phase with respect to the electric dipole. Since this lateral force is non-related to any chirality, the helicity or chirality of the plane wave does not affect the total lateral force at all. Figure 4.4 (a) and (b) show that it's almost no difference under a left circularized plane wave illumination $\vec{E} = (\hat{y} - i\hat{z})E_0\exp(ik_x x)$, or a right circularized plane wave illumination $\vec{E} = (\hat{y} + i\hat{z})E_0\exp(ik_x x)$.

4.2.2 Interactions with chiral particles

In the last section, it's found that lateral forces can appear on an anisotropic structure, as long as electric dipoles and magnetic dipoles on desired directions can be excited. However, this lateral force is very small, approximately three orders' smaller than the regular scattering forces, and does not respond to the external field chirality. To enhance the tunability of lateral forces, scatterers made of isotropic chiral materials are studied.

Considering a reciprocal isotropic chiral materials, the constitutive relations are:

$$\begin{aligned} \vec{D} &= \epsilon_0\epsilon_r\vec{E} + \frac{i\kappa}{c}\vec{H}, \\ \vec{B} &= \frac{-i\kappa}{c}\vec{E} + \mu_0\mu_r\vec{H}, \end{aligned} \tag{4.17}$$

where c is the speed of light in vacuum, and κ is the chiral parameter. A regular value for κ lies in the smaller or the same order of the refractive index n, depending on the strength of the chirality. The chiral constitutive relations can also be written in terms

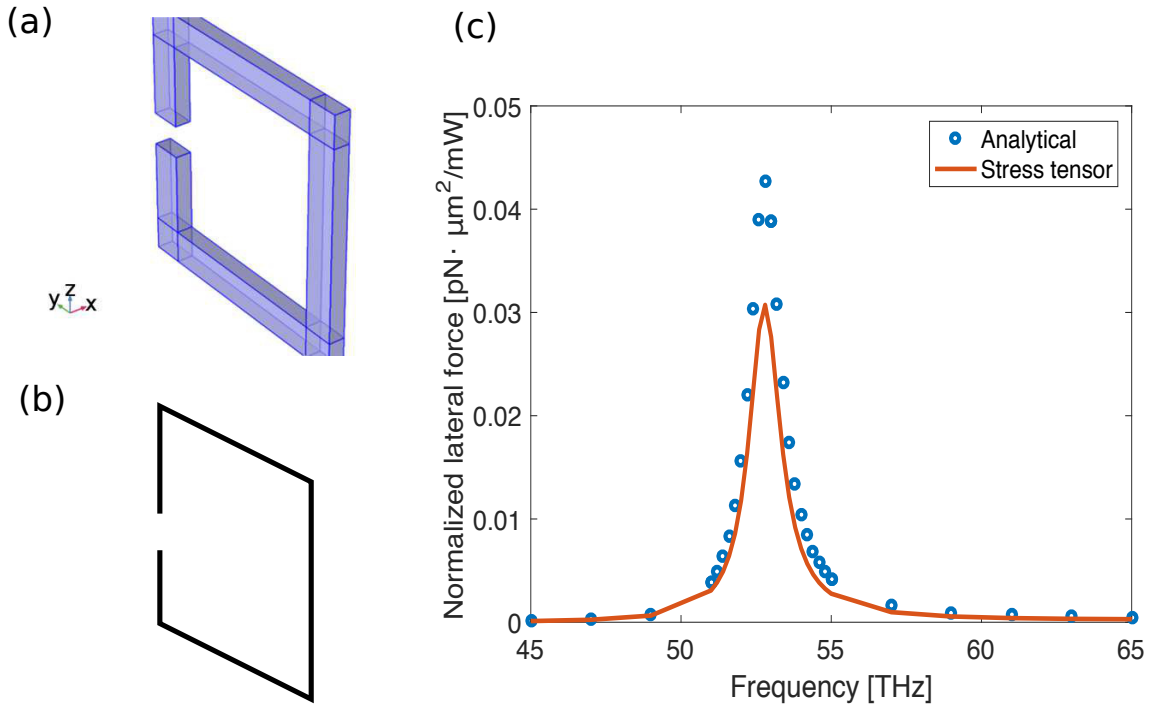

Figure 4.2 Lateral forces on a SRR structure. (a) Sketch of a real SRR made of gold. (b) Effective line current model used in simulations. The side length is 700 nm, while the gap is 50 nm. The effective line current conductivity $\sigma_{\text{line}} = \sigma_{\text{gold}} A_{\text{eff}}$, where A_{eff} is the cross section area of the real SRR in (a). (c) Normalized lateral force under plane wave illumination with linearized polarization E_z only. Analytical results meet well with numerical results calculated from Maxwell stress tensor. The discrepancy is due to the non-pure magnetic dipole.

of electric and magnetic dipoles moments as:

$$\begin{aligned} \vec{p} &= \alpha_e \vec{E} + i\chi\mu_0 \vec{H}, \\ \vec{m} &= -i\chi \vec{E} + \alpha_m \vec{H}, \end{aligned} \tag{4.18}$$

where α_e and α_m are electric and magnetic polarizabilities respectively, and χ is the electro-magnetic coupling coefficient, denoting the strength of chirality. In general all these coefficients are tensors, while in the isotropic case, they simply reduce to a scalar.

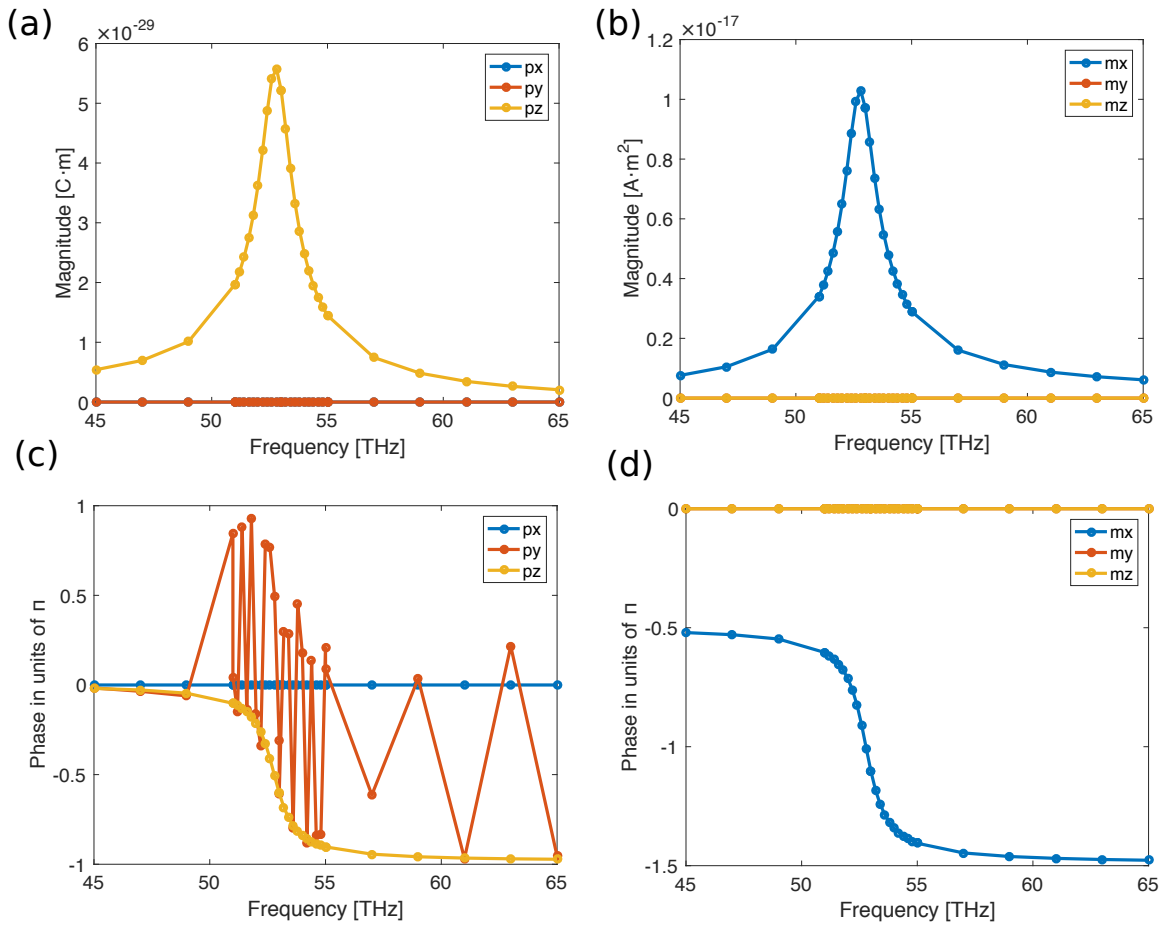

Figure 4.3 (a) Magnitude of induced electric dipole. (b) Magnitude of induced magnetic dipole. (c) Phase of the induced electric dipole. (d) Phase of the induced magnetic dipole.

By substituting Eqn. 4.18 into Eqn. 4.14, and taking the time-averaged force, we get:

$$\begin{aligned} < \vec{F}_{p-m} > &= \frac{1}{2}\mathrm{Re}[-\frac{k^4}{6\pi\epsilon_0 c}(\vec{p}\times\vec{m}^*)] \\ &= -\frac{k^4}{12\pi\epsilon_0 c}\mathrm{Re}[i\alpha_e\chi^*(\vec{E}\times\vec{E}^*) + i\chi\mu_0\alpha_m^*(\vec{H}\times\vec{H}^*) \\ &+ \alpha_e\alpha_m^*(\vec{E}\times\vec{H}^*) + |\chi|^2\mu_0(\vec{E}^*\times\vec{H})]. \end{aligned} \tag{4.19}$$

Recalling the definition for the spin angular momentum of light in Eqn. 4.7, one may notice the first term $< \vec{F}_{ee} > \sim \mathrm{Im}[\alpha_e\chi^*\vec{s}_e]$, the second term $< \vec{F}_{hh} > \sim \mathrm{Im}[\alpha_m^*\alpha_m^*\chi\vec{s}_m]$, the third and the fourth term correspond to the real and the imaginary part of Poynting vector density, or linear momentum density. It's apparent that the first two terms

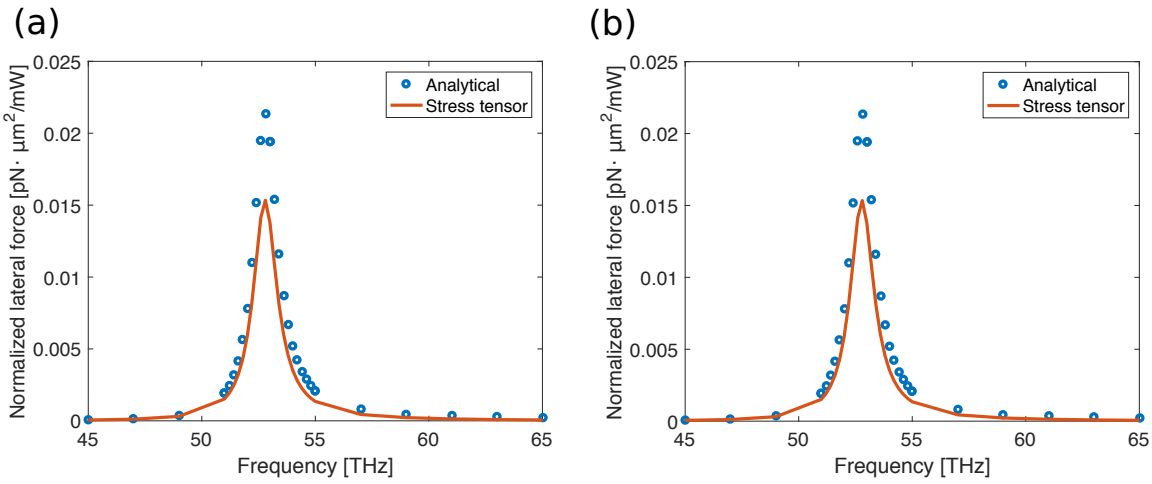

Figure 4.4 (a) Normalized lateral force under plane wave illumination with left circularized polarization ($E_z = -iE_y$). (b) Normalized lateral force under plane wave illumination with right circularized polarization ($E_z = iE_y$).

strongly reply on the chirality of this particle. When the chirality χ changes signs, the direction of the lateral force will also flip. However, there is a term which does not depend on the chirality at all. This indicates that an achiral isotropic particle is possible to feel lateral forces as well.

First a non-magnetic particle with $\alpha_m = 0$ is considered. A plane wave only have spin angular momentum and poynting vector along the propagation direction, so no terms would contribute to the lateral force. However, for an evanescent wave such as surface plasmon polaritons on a noble metal, $\vec{s}_e$ have an transverse part, and $\vec{F}_{ee}$ is proportional to the chirality of the particle. As in Fig. 4.5 (a), a point dipole is imposed 1500 nm above a material with $\epsilon = 2 + 0.2i$ and $\mu = 1$. For simplicity, it is modeled as: $\vec{p} = \alpha_e \vec{E}_0 + i\chi\mu_0 \vec{H}_0$ and $\vec{m} = -i\chi\vec{E}_0$, where $\alpha_e = 10^{-29} F \cdot m^2$, $\vec{E}_0$ and $\vec{H}_0$ is the background field, i.e. the evanescent field when no particle is presented. This model to describe a point dipole is simplified but is convenient to analyze how the evanescent waves can affect the lateral force on a chiral particle. However, if the dipole is too close to the surface, the coupling between the dipole and the surface plasmon will actually modify the local field. In that sense, the simplified force calculation will be inaccurate.

Figure 4.5 (b) shows normalized lateral forces from analytic and numerical calculations. When the chirality of the particle changes sign, the direction of the force will flip. In this way, chiral particle sorting can be realized. The discrepancy between the analytic and numerical results comes from the coupling between the dipole and SPP aforementioned. If the point is lifted farther away from the surface, the discrepancy will become smaller.

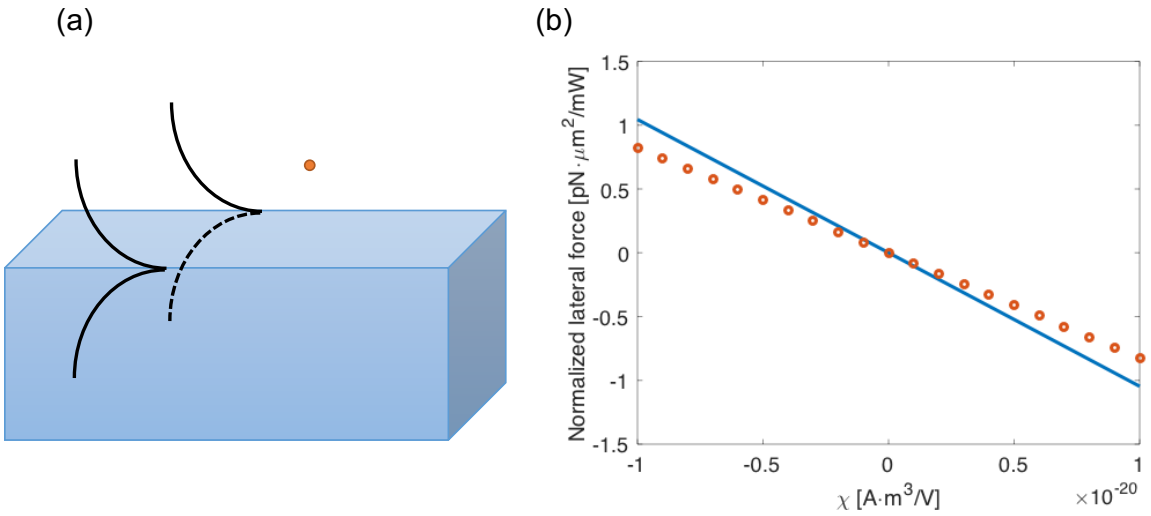

Figure 4.5 (a) A point dipole is placed 1500 nm above a material with $\epsilon = 2 + 0.2i$ and $\mu = 1$. A SPP is excited at 49 THz and propagating to the x-direction. (b) Normalized lateral force from analytic (red dots) and numerical (blue line) results.

4.3 Enhanced selectivity by mixing TE and TM SPP using LHM

4.3.1 Co-existence of TE and TM surface plamons

In Chapter 1, it is shown that the existence of a TM SPP on the interface of two half-infinite materials requires their perimittivity to be opposite signs. Similarly, for a TE SPP to exist, we need:

$$\begin{aligned} &\frac{\kappa_1}{\mu_1} + \frac{\kappa_2}{\mu_2} = 0, \\ &k_{\text{spp}} = k_0 \sqrt{\frac{\mu_1 \mu_2}{\mu_1 + \mu_2} \frac{\epsilon_1 \mu_2 - \epsilon_2 \mu_1}{\mu_2 - \mu_1}}, \end{aligned} \tag{4.20}$$

where κ_i is the decaying factor and has a positive real part on both sides, and μ_i is the permeability of each material. Though in nature, materials with notable negative permeablity do not exist, the development of metamaterials with carefully designed small resonant units bring this idea to reality. Therefore, to make a real chiral surface plasmon which mixes the transverse electric field and magnetic field with the same frequency and propagation constant, we need Eqn. 1.9 and Eqn. 4.21 to hold simultaneously, which actually results in:

$$\begin{aligned} \epsilon_1 + \epsilon_2 = 0, \\ \mu_1 + \mu_2 = 0. \end{aligned} \tag{4.21}$$

This constraint is too strong and also comes with a flat dispersion relation as shown in Fig. 4.6 (a), which is completely useless in reality. Figure 4.6 (b) shows a phase diagram for the existence area of TE and TM SPP modes, which is based on calculations when the whole space is filled by two different materials with their permittivity and permeability to be (ϵ_1, μ_1) and (ϵ_2, μ_2) respectively. Assuming that $\epsilon_2\mu_2 > \epsilon_1\mu_1$, the whole diagram then can be divided into several blocks depending on the relation of ϵ_1,ϵ_2 and μ_1,μ_2. The horizontal dashed line sits at ϵ_1/ϵ_2=-1, while the vertical dashed line sits at μ_1/μ_2=-1. The tilted dotted-dashed line in the third quadrant represents an impedence matched case that $\epsilon_1/\epsilon_2 = \mu_1/\mu_2$. The curved line in the third quadrant is actually hyperbolic and represents $\epsilon_1\epsilon_2/\mu_1\mu_2 = 1$.The area where TM SPP can exist is marked in blue and that for the TE SPP is in orange. The only intersection of all dashed lines is a point where $\epsilon_1 + \epsilon_2 = 0$ and $\mu_1 + \mu_2 = 0$ is where TE and TM SPPs can co-exist. Interestingly, I found the derivations different from some literature [77, 78].

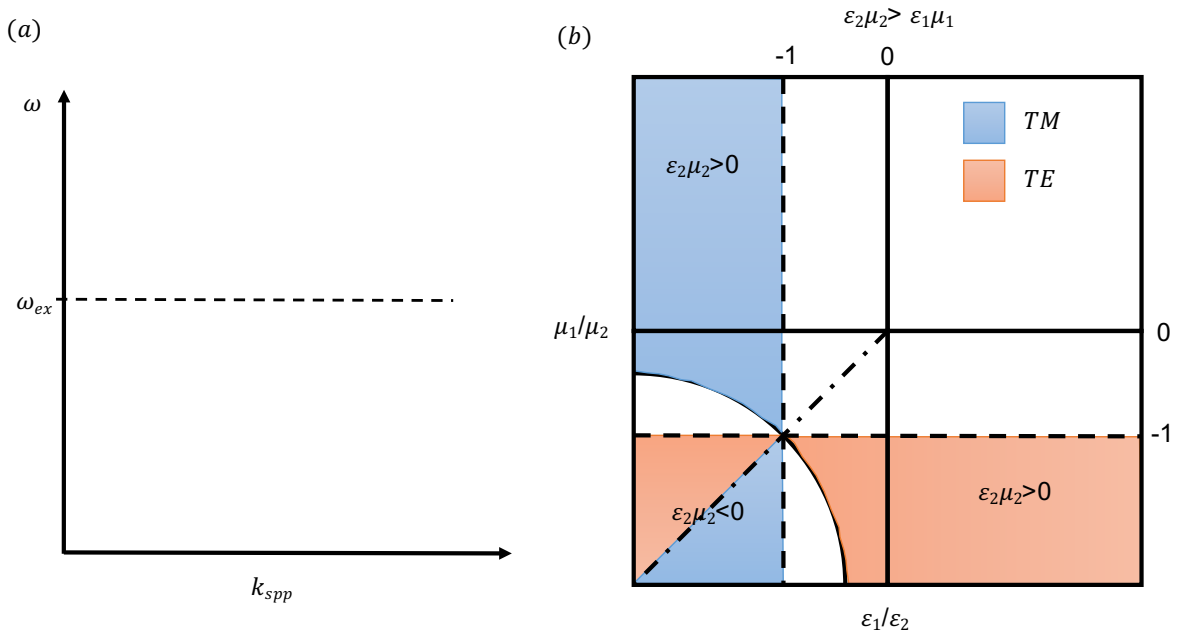

Figure 4.6 (a) In a impedence perfectly matched double negative material, the TE and TM SPP modes can co-exist, but constrained by a flat dispersion subject to the excitation frequency. (b) A phase diagram of TE and TM SPP existing area. The whole diagram is based on presumption that $\epsilon_2\mu_2 > \epsilon_1\mu_1$. The horizontal (vertical) dashed line sits at ϵ_1/ϵ_2=-1 (μ_1/μ_2). The tilted dotted–dashed line in the third quadrant represents $\epsilon_1/\epsilon_2 = \mu_1/\mu_2$. The curved line in the third quadrant represents $\epsilon_1\epsilon_2/\mu_1\mu_2 = 1$

4.3.2 Chiral surface plasmons modulation using LHM slab

While Fig. 4.6 (b) is a "static" phase diagram at a certain frequency, the real materials are usually dispersive in nature, especially when the realization of tailored ϵ and μ requires the usage of metamaterials which is intrinsically resonant. Supposing a material, whose electromagnetic properties are designed as follows:

$$\begin{aligned} \epsilon(\omega) &= 1 - \frac{\omega_p^2}{\omega^2}, \\ \mu(\omega) &= 1 - \frac{F\omega^2}{\omega^2 - \omega_m^2}, \end{aligned} \tag{4.22}$$

where F=0.56, $\omega_p = 5.14 \times 10^{14}$ rad/s, and $\omega_m = 2.06 \times 10^{14}$ rad/s. Figure 4.7 (b) plots the dispersion relation between the circular frequency ω and the propagation constant k_{spp} with the setup shown in Fig. 4.7 (a), where the titled black line is the light line, the

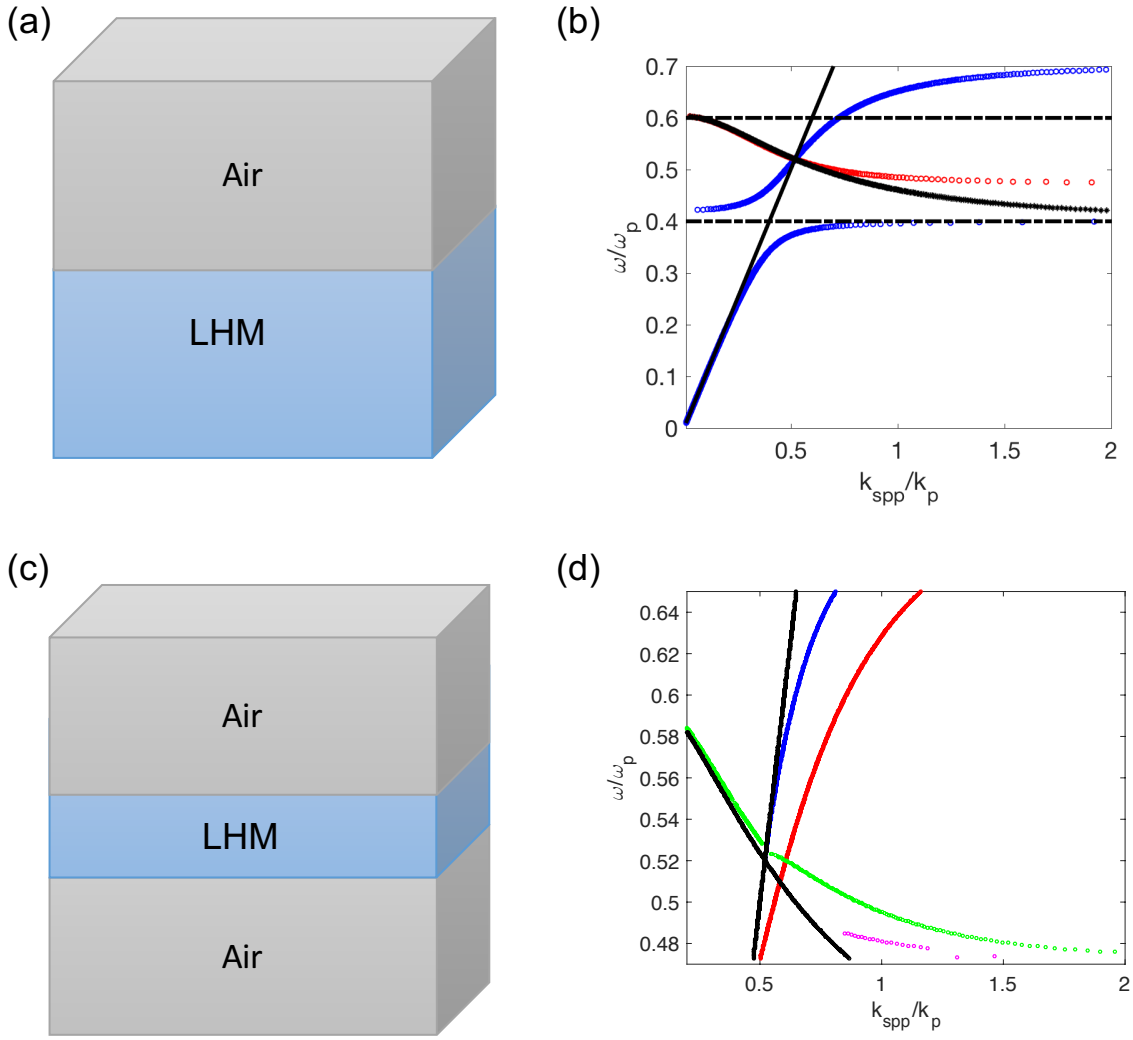

Figure 4.7 (a) The scheme of a semi-infinite left-handed material. (b) Dispersion relation of the SPP supported by the semi-infinite left-handed material. Blue lines indicate TM SPP while red lines indicate TE SPP. They intersect with each other on the light line. (c) The scheme of a LHM slab embeded in air. (d) The coupling between of interfaces of the slab breaks degeneracy and separate both TM and TE SPPs into a symmetric and anti-symmetric pair. Blue and red lines are symmetric and anti-symmetric TM modes with respect to H field, while green and magenta lines are symmetric and anti-symmetric TE modes with respect to E field. The intersection of the red and green line defines well confined anti-symmetric TM modes and symmetric TE modes. At this point, a coherent pair of TE and TM SPP with the same frequency and propagation constant can co-exist.

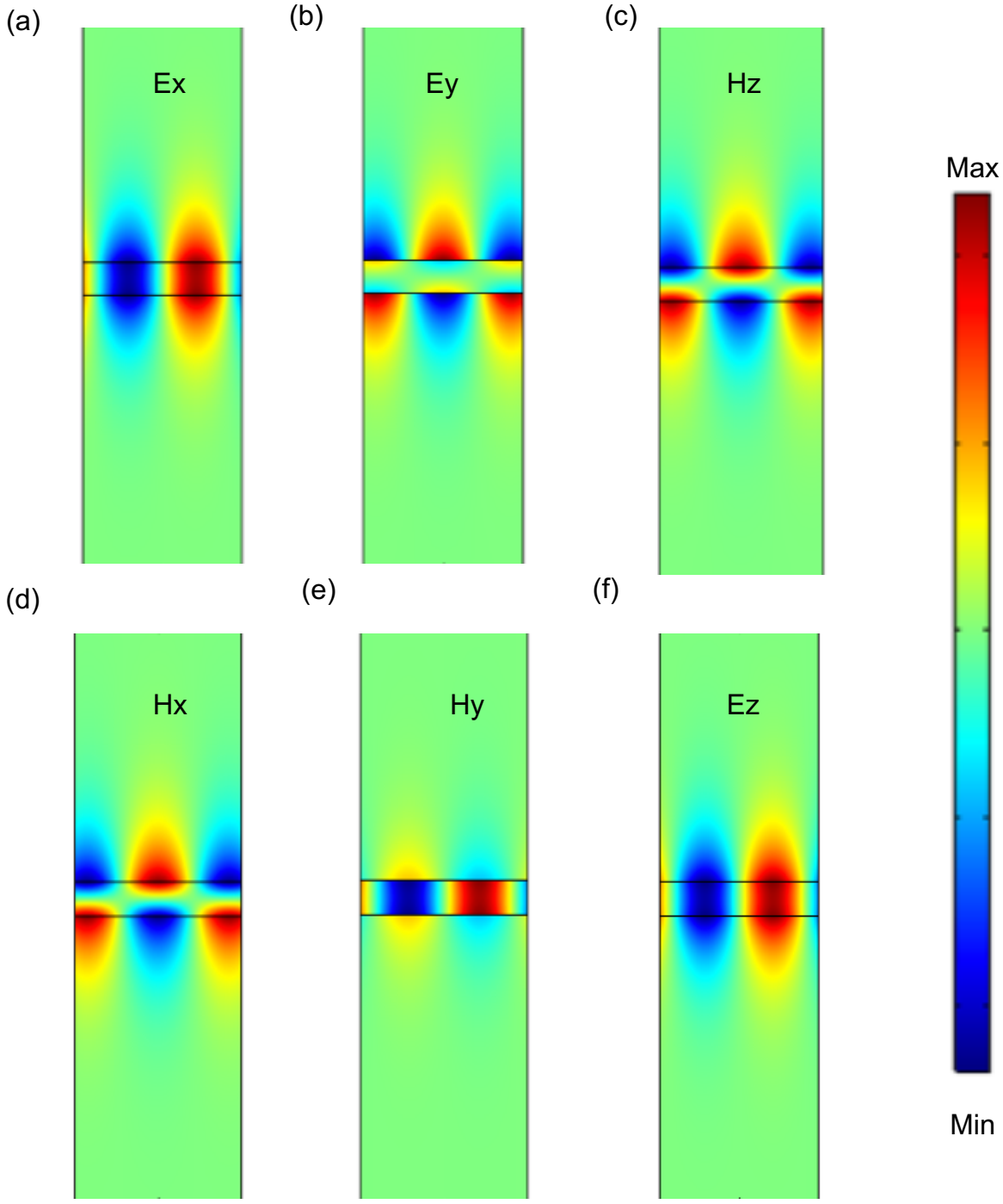

Figure 4.8 (a) & (b) & (c) are the E_x, E_y, H_z field distribution for the TM SPP. (d) & (e) & (f) are the H_x, H_y, E_z field distribution for the TE SPP. All fields are normalized by its own.

blue lines represent the TM SPP, and the red one represents the TE SPP. It shows that no intersection between the TE and TM SPP happens in the guided mode region, but right on the light line.

However, when a left-handed material slab with finite (small) thickness is present, the surface modes on the two interfaces may talk to each other. Their coupling will break the degeneracy and hence, each dispersion line will bifurcate into a symmetric and an anti-symmetric branch. By carefully designing the thickness of the LHM slab, the lower branch from the upper band may intersect with the higher branch of the lower band. In this way, the co-existence of both TE and TM SPP on the interface can be achieved. Figure 4.7 (c) & (d) show the setup and the dispersion relation. In Fig. 4.7 (a), a LHM slab with thickness $t = c/\omega_m = 1.46\mu m$ is sandwiched in air. In Fig. 4.7 (b), all modes around the intersection point are plotted. The blue and red lines represent symmetric and anti-symmetric TM modes with respect to the H-field, while the green and magenta lines represent symmetric and anti-symmetric TE modes with respect to the E-field. The intersection point has a TM and TE SPP at $\omega = 1.67 \times 10^{14}$ rad/s, and $k_{\text{spp}} = 1.04 \times 10^6 m^{-1}$.

Figure 4.8 gives field plots of all components, in which (a) to (c) represent E_x, E_z and H_y for the TM SPP, while (d) to (f) represent H_x, H_z and E_y for the TE SPP. The colorbar is normalized by its maximum.

Moreover, the closed form of the all fields for each polarization above the LHM slab read as follows: For TM and TE SPP respectively, there are:

$$\begin{cases} H_y = A_{TM} e^{-jk_{\text{spp}}x - \kappa z} \\ E_x = -\frac{\partial_z H_y}{j\omega\epsilon} = \frac{\kappa A_{TM}}{j\omega\epsilon} e^{-jk_{\text{spp}}x - \kappa z} \\ E_z = \frac{\partial_x H_y}{j\omega\epsilon} = -\frac{k_{\text{spp}} A_{TM}}{\omega\epsilon} e^{-jk_{\text{spp}}x - \kappa z} \end{cases} . \tag{4.23}$$

$$\begin{cases} E_y = A_{TE} e^{-jk_{\text{spp}}x-\kappa z} \\ E_x = -\frac{\partial_z E_y}{-j\omega\epsilon} = -\frac{\kappa A_{TE}}{j\omega\mu} e^{-jk_{\text{spp}}x-\kappa z} \\ E_z = \frac{\partial_x H_y}{j\omega\epsilon} = -\frac{k_{\text{spp}} A_{TE}}{\omega\mu} e^{-jk_{\text{spp}}x-\kappa z} \end{cases} . \tag{4.24}$$

It is obvious that the TE and TM SPP do not have an overlapped component. Thus it offers a great flexibility and convenience to tune the chirality of the surface waves by independently changing the either without affecting the other.

4.3.3 Enhanced selectivity

Considering either a pure TM SPP or a pure TE SPP possessing the field formulation in Eqn. 4.23 or Eqn. 4.24, it can be proved that the Poynting vector or linear momentum density only have its component along the propagation direction (x-direction), leaving P_y=0. However, the TE and TM modes are mixed with certain phase difference, the transverse P_y could be non-zero, leading to the lateral force. The transverse linear momentum appear when a chiral surface wave is present, and is referred to as "Belinfante spin momentum". It is a result of inhomogenuous distribution of the spin of light. I now show that the Belinfante spin momentum induced force can help enhance the ability to chiral particles sorting.

Considering a LHM slab setup as in Fig. 4.7, and a particle is settled 1500 nm above the slab. This particle is isotropic and chiral, with its constitutive relations defined in Eqn. 4.18. The electromagnetic parameters are chosen as $\alpha_e = 10^{-29}\text{F}\cdot\text{m}^2$, $\alpha_m = 10^{-18}\text{m}^3$, and $\chi = \pm 10^{-20}\text{A}\cdot\text{m}^3/\text{V}$. An extra phase factor is added to the TM SPP and swept from 0 to 2π. It's worth mentioning that for simplicity, the field taken in Eqn. 4.18 is the incident surface wave, and the point is set as an electric dipole and a magnetic dipole in COMSOL. This model is a perfect dipole model, and is clear to show how the surface waves itself impact the lateral force, but will be oversimplified if the local field is strongly modified by the coupling between the dipole and the surface waves.

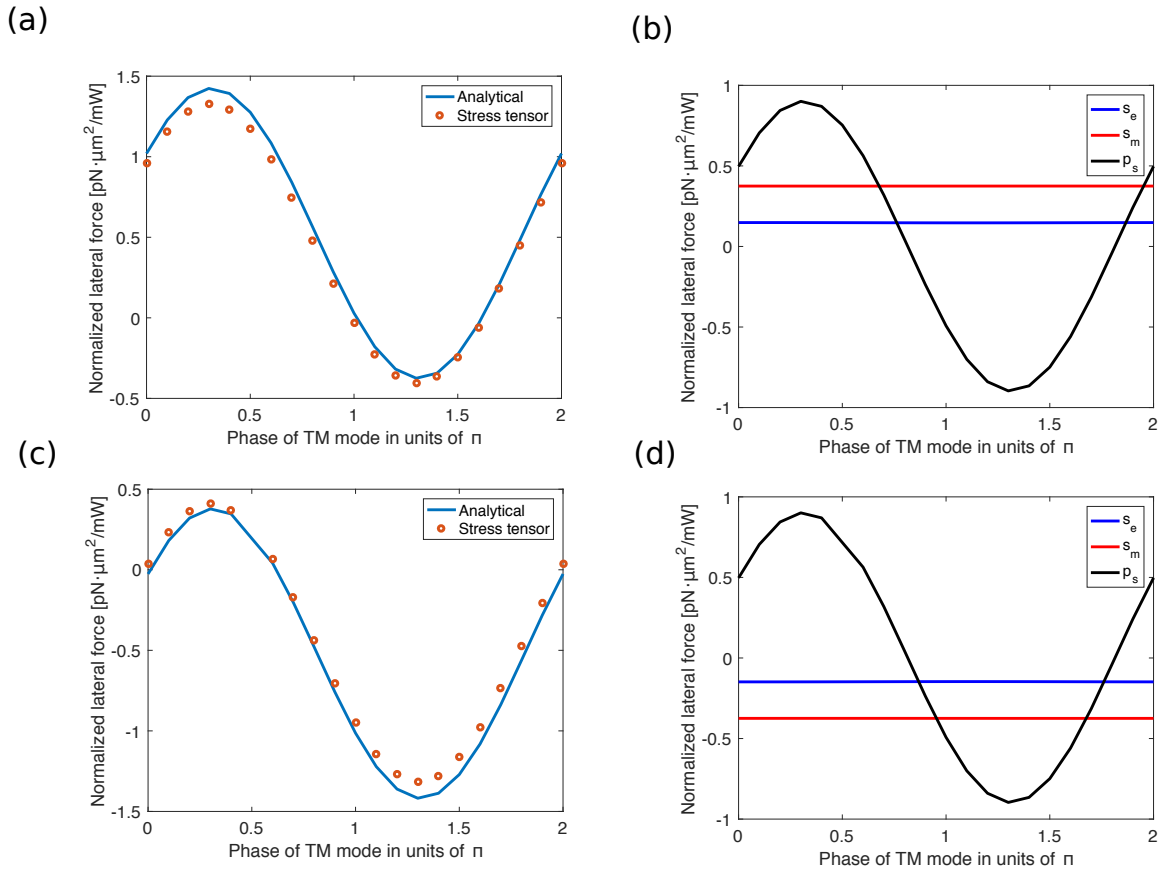

Figure 4.9 Normalized force modulation when the phase between TE and TM modes changes. (a) & (b) Total lateral forces for particles with $\alpha_e = 10^{-29} F \cdot m^2$, $\chi = -10^{-20} A \cdot m^3/V$, and $\alpha_m = 10^{-18} m^3$. Blue lines in (a) are calculated analytically using cross production of electric and magnetic dipoles, while red dots are got from Maxwell stress tensors. (b) Decomposition of the total lateral forces into contributions from spin part of electric field (blue), magnetic field (red), and berlinfante spin momentum (black). (c) & (d) Total lateral forces for particles with $\alpha_e = 10^{-29} F \cdot m^2$, $\chi = 10^{-20} A \cdot m^3/V$, and $\alpha_m = 10^{-18} m^3$. Blue lines in (c) are calculated analytically using cross production of electric and magnetic dipoles, while red dots are got from Maxwell stress tensors. (d) Decomposition of the total lateral forces into contributions from spin part of electric field (blue), magnetic field (red), and berlinfante spin momentum (black).

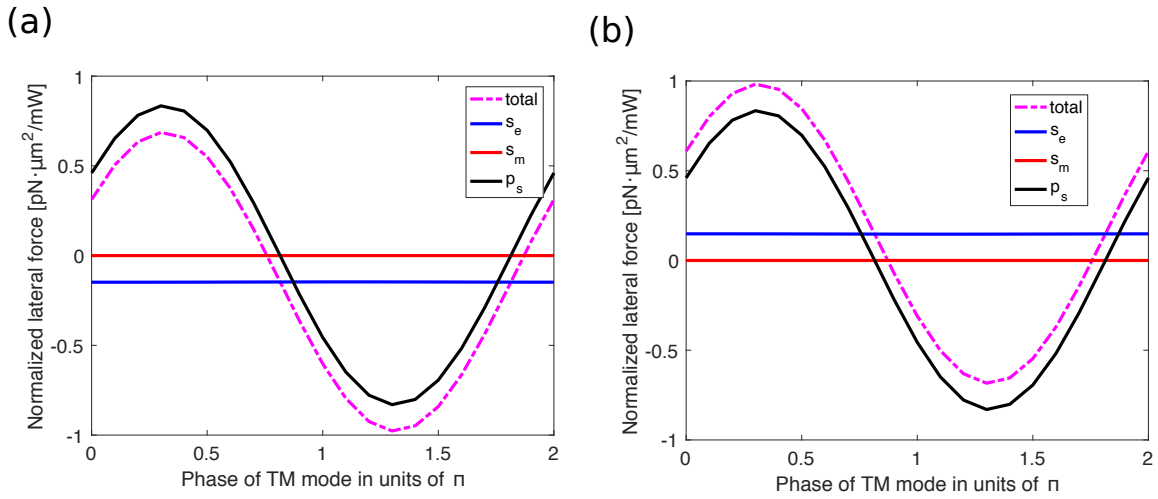

Figure 4.10 (a) Normalized lateral forces for particles with $\alpha_e = 10^{-29}F \cdot m^2$, $\chi = 10^{-20}A \cdot m^3/V$, and $\alpha_m = 0m^3$. Magenta dots denote the total lateral force while contributions from spin part of electric field, magnetic field, and berlinfante spin momentum are denoted in blue, red and black lines separately. (b) Normalized lateral forces for particles with $\alpha_e = 10^{-29}F \cdot m^2$, $\chi = -10^{-20}A \cdot m^3/V$, and $\alpha_m = 0m^3$. Magenta dots denote the total lateral force while contributions from spin part of electric field, magnetic field, and berlinfante spin momentum are denoted in blue, red and black lines separately.

Figure 4.9 (a) plot the total lateral force for $\chi > 0$, in which the blue line represents results by analytically calculating the dipole-dipole interaction term, and the red dots represent results from Maxwell stress tensors. Figure 4.9 (b) shows how the total lateral force is decomposed into contributions from the electric part of spin, the magnetic part of spin, and the Berlinfante spin momentum. Figure 4.9 (c) & (d) plot the same but for $\chi < 0$. It is clear that the spin of light $\vec{s}_e$ and $\vec{s}_m$ do not depend on the specific phase of the surface mode but on the chirality of the particles. To the contrary, the Berlinfante spin momentum, or the chirality of the wave itself rather than the chirality of the particles exerts more influence on the achiral lateral force, which is sensitive to the phase of each mode.

Figure 4.10 (a) & (b) show the total lateral force and its decomposition for non-magnetic particles with α_m=0, $\alpha_e = 10^{-29}F \cdot m^2$, $\chi = \pm 10^{-20}A \cdot m^3/V$ respectively. We

can see the spin of the magnetic part is decoupled from the total force.

In short, the total lateral force of a chiral particle may have two different origins. One comes from the coupling between the chirality of the particle and the spin angular momentum of light. The other comes from a non-chiral term, which is due to the Berlinfante spin momentum. By modulating the relative phase of the TM and TE SPP, we have better tunablity to modulate chiral particle sorting.

4.4 Conclusion

In conclusion, this work showed due to the dipole-dipole interaction, a lateral force appear. When the electric and magnetic dipole are simultaneously excited, their interference with each other will make the radiation non-symmetric, and thus exert a recoil force on itself. Lateral force under evanescent wave illumination may have two origins: one corresponds to the coupling between the chirality of the particle and the spin angular momentum of light, while the other is due to the helicity of light, regardless of the particle being chiral or not. Surface plasmons can make better usage of the incident power and confine the whole field in a relatively small region in contrast to the total internal reflection. By utilizing a left handed material slab, TE and TM surface plasmons can be excited simultaneously and independently. The modulation between their phases give us great flexability to modulate lateral forces, and thus pave the way for chiral particle sorting.

CHAPTER 5. CONCLUSION

Light matter interaction is a broad and historic topic, where people can manipulate light in different levels. The fast development of nano-technology makes it possible to control light in the micro- and nano-meter scale. Theories governing the interaction between light and these photonic structures may vary from classical to quantum. In some cases, the interaction is merely classical such as that in a bandgap photonic crystal where classical light is scattered by periodic embeddings, the wave equations can be reformulated similarly to an Hermitian Schrodinger equation, and thus a lot of ideas from the quantum mechanics and the electronic systems and be "borrowed" to describe the classic electromagnetic waves, such as band diagram, Bloch modes, etc. In other cases, such as the surface plasmon polariton, a quasi-particle representing the collective oscillations of electron densities, is quantum originated, but can still be analyzed from the classical Maxwell equations to a certain extent. There are also cases, though falling into the same category, may have different origins such as optical forces. Traditional forces including the radiational force and gradient force, are just the interaction of a electromagnetic wave on the electrons in the media, while the Casimir force is a result of quantum fluctuation, related to the zero-point energy of vacuum. In my thesis work, all problems, whether quantum or classical originated, can be resolved within the frame of Maxwell equations.

In Chapter 2, I studied how a photonic crystal with the Dirac cone on the center can be used to manipulate light. This kind of PhC behaves as an impedance matched zero-index material, which can do phase front modulation and cloaking. However, an oblique

incident wave will excite the middle flat band and thus the zero-index behavior is lost. By developing a method combining complex-k band calculation and absorbing boundary conditions for Bloch modes, the mode interaction is analyzed in details, and it leads to the conclusion that the multi-peak feature in the transmission spectrum originates from the multiple reflection of Bloch modes at the interface between the PhC slab and air.

In Chapter 3, I explored the possibility of using graphene as an opto-mechanical device. I first realized that the coupling of surface plasmon polaritons on the double graphene sheets can induce orders' stronger force than the regular slab waveguides. Using this enhanced gradient force, we can modulate the mechanic state of a pre-curved graphene sheet, and measured that by observing the total reflection and transmission.

In Chapter 4, I studied how the lateral force, originating from dipole-dipole self-interaction in addition to the traditional radiational and gradient forces, can be associated with the chirality of waves and the chirality of particles. I first revealed that lateral forces can appear under plane wave illumination on non-chiral particles. Then I showed how an evanescent wave can produce a chirality-related lateral force, which can be used for chiral particle sorting. By mixing TE and TM SPP using left-handed material slabs, we can modulate the lateral force, which would assist enhancing the selectivity of chiral particles.

This thesis work is still far from perfect and there are a lot more photonic structures that can modulate light, and even within the same type of structure it remains a lot to be done. For example, the discovery of Dirac cone of photonic crystals have pioneered a completely new field named topological photonics, where people introduce topology concepts into photonic systems. One of the most notable feature is the unidirectional states protected by topology and thus will be less scattered. Our developed method, especially absorbing the Bloch modes on the back side to eliminate back reflection may play a role in the edge state study. Surface plasmons on graphene can be reduced to a quantum level, in which Maxwell equations does not hold and a quantized theory needs

to be applied. Also single photons on graphene can induce non-linear effects, which can enrich the field of nonlinear optics and strong photon-matter interactions.

Finally, I'd like to end my thesis by quoting the words from Henry Augustus Rowland, which has inspired me since ten years ago:

"The whole universe is before us to study. The greatest labor of the greatest minds has only given us a few pearls; and yet the limitless ocean, with its hidden depths filled with diamonds and precious stones, is before us. The problem of the universe is yet unsolved, and the mystery involved in one single atom yet eludes us. The field of research only opens wider and wider as we advance, and our minds are lost in wonder astonishment at the grandeur and beauty unfolded before us. Shall we help in this grand work, or not? Shall our country do its share, or shall it still live in the almshouse of the world?"

BIBLIOGRAPHY

[1] N. W. Ashcroft and N. D. Mermin. *Solid State Physics*. Brooks Cole, 1976.

[2] E. Yablonovitch. Inhibited spontaneous emission in solid-state physics and electronics. *Phys. Rev. Lett.*, 58:2059–2062, May 1987.

[3] S. John. Strong localization of photons in certain disordered dielectric superlattices. *Phys. Rev. Lett.*, 58:2486–2489, Jun 1987.

[4] J. D. Joannopoulos, R. D. Meade, S. G. Johnson, and N. Joshua. *Photonic Crystals: Molding the Flow of Light*. Princeton University Press, 2011.

[5] M. S. Tame, K. R. McEnery, . K. Özdemir, J. Lee, S. A. Maier, and M. S. Kim. Quantum plasmonics. *Nat. Phys.*, 9(6):329–340, Jun 2013.

[6] S. A. Maier. *Plasmonics: Fundamentals and Applications*. Springer, 2007.

[7] A. Challener, C. Peng, V. Itagi, D. Karns, W. Peng, Y. Peng, X. Yang, X. Zhu, J. Gokemeijer, Y.-T. Hsia, G. Ju, R. Rottmayer, M. Seigler, and C. Gage. Heat-assisted magnetic recording by a near-field transducer with efficient optical energy transfer. *Nat Phot.*, 3(4):220–224, Apr 2009.

[8] S. Nie and S. R. Emory. Probing single molecules and single nanoparticles by surface-enhanced raman scattering. *Science*, 275(5303):1102–1106, 1997.

[9] J. Homola, S. S. Yee, and G. Gauglitz. Surface plasmon resonance sensors: review. *Sensors and Actuators B: Chemical*, 54(1):3 – 15, 1999.

[10] J. B. Pendry, A. J. Holden, D. J. Robbins, and W. J. Stewart. Magnetism from conductors and enhanced nonlinear phenomena. *IEEE Transactions on Microwave Theory and Techniques*, 47(11):2075–2084, Nov 1999.

[11] D. R. Smith, W. J. Padilla, D. C. Vier, S. C. Nemat-Nasser, and S. Schultz. Composite medium with simultaneously negative permeability and permittivity. *Phys. Rev. Lett.*, 84:4184–4187, May 2000.

[12] N. Yu, P. Genevet, M. A. Kats, F. Aieta, J. Tetienne, F. Capasso, and Z. Gaburro. Light propagation with phase discontinuities: Generalized laws of reflection and refraction. *Science*, 334(6054):333–337, 2011.

[13] L. Novotny. *Principles of nano-optics*. Cambridge University Press, Cambridge, 2012.

[14] C. M. Soukoulis and M. Wegener. Past achievements and future challenges in the development of three-dimensional photonic metamaterials. *Nat Phot.*, 5(9):523–530, Sep 2011.

[15] P. Markos and C. M. Soukoulis. *Wave Propagation: From Electrons to Photonic Crystals and Left-Handed Materials*. Princeton University Press, 2008.

[16] C.T. Chan, S. Datta, K.M. Ho, and C. M. Soukoulis. A. *Phys. Rev. B*, 50:1988–1991, Jul 1994.

[17] S. Foteinopoulou and C. M. Soukoulis. Negative refraction and left-handed behavior in two-dimensional photonic crystals. *Phys. Rev. B*, 67:235107, Jun 2003.

[18] S. Foteinopoulou, E. N. Economou, and C. M. Soukoulis. Refraction in media with a negative refractive index. *Phys. Rev. Lett.*, 90:107402, Mar 2003.

[19] F. D. M. Haldane and S. Raghu. Possible realization of directional optical waveguides in photonic crystals with broken time-reversal symmetry. *Phys. Rev. Lett.*, 100:013904, Jan 2008.

[20] Z. Wang, Y. Chong, J. D. Joannopoulos, and M. Soljacic. Observation of unidirectional backscattering-immune topological electromagnetic states. *Nature*, 461(7265):772–775, Oct 2009.

[21] X. Zhang. Observing zitterbewegung for photons near the dirac point of a two-dimensional photonic crystal. *Phys. Rev. Lett.*, 100:113903, Mar 2008.

[22] M. Diem, T. Koschny, and C. M. Soukoulis. Transmission in the vicinity of the dirac point in hexagonal photonic crystals. *Physica B: Condensed Matter*, 405(14):2990 – 2995, 2010. Proceedings of the Eighth International Conference on Electrical Transport and Optical Properties of Inhomogeneous Media.

[23] X. Huang, Y. Lai, Z. Hang, H. Zheng, and C. T. Chan. Dirac cones induced by accidental degeneracy in photonic crystals and zero-refractive-index materials. *Nat Mater*, 10(8):582–586, Aug 2011.

[24] K. Sakoda. *Optical Properties of Photonic Crystals*. Springer-Verlag, 2005.

[25] M. Davanço, Y. Urzhumov, and G. Shvets. The complex bloch bands of a 2d plasmonic crystal displaying isotropic negative refraction. *Opt. Express*, 15(15):9681–9691, Jul 2007.

[26] C. Fietz. Absorbing boundary condition for bloch floquet eigenmodes. *J. Opt. Soc. Am. B*, 30(10):2615–2620, Oct 2013.

[27] J. M. Jin. *The Finite Element Method in Electromagnetics*. Wiley-IEEE Press, 2002.

[28] S. G. Johnson, P. Bienstman, M. A. Skorobogatiy, M. Ibanescu, E. Lidorikis, and J. D. Joannopoulos. Adiabatic theorem and continuous coupled-mode theory for efficient taper transitions in photonic crystals. *Physical Review E*, 66(6), Dec 2002.

[29] U. Fano. Effects of configuration interaction on intensities and phase shifts. *Phys. Rev.*, 124:1866–1878, Dec 1961.

[30] L. Novotny, R. X. Bian, and X. S. Xie. Theory of nanometric optical tweezers. *Phys. Rev. Lett.*, 79:645–648, Jul 1997.

[31] G. S. Wiederhecker, L. Chen, A. Gondarenko, and M. Lipson. Controlling photonic structures using optical forces. *Nature*, 462(7273):633–636, Dec 2009.

[32] V. Ginis, P. Tassin, C. M. Soukoulis, and I. Veretennicoff. Enhancing optical gradient forces with metamaterials. *Phys. Rev. Lett.*, 110:057401, Jan 2013.

[33] V. Intaraprasonk and S. Fan. Enhancing the waveguide-resonator optical force with an all-optical on-chip analog of electromagnetically induced transparency. *Phys. Rev. A*, 86:063833, Dec 2012.

[34] C. Huang and L. Zhu. Enhanced optical forces in 2d hybrid and plasmonic waveguides. *Opt. Lett.*, 35(10):1563–1565, May 2010.

[35] J. Chen, J. Ng, Z. Lin, and C. T. Chan. Optical pulling force. *Nat. Photonics*, 5(9):531–534, Sep 2011.

[36] J. Zhang, K. F. MacDonald, and N. I. Zheludev. Optical gecko toe: Optically controlled attractive near-field forces between plasmonic metamaterials and dielectric or metal surfaces. *Phys. Rev. B*, 85:205123, May 2012.

[37] M. Eichenfield, C. P. Michael, R. Perahia, and O. Painter. Actuation of micro-optomechanical systems via cavity-enhanced optical dipole forces. *Nat. Photonics*, 1(7):416–422, Jul 2007.

[38] J. Ma and M. L. Povinelli. Applications of optomechanical effects for on-chip manipulation of light signals. *Curr. Opin. Solid State Mater. Sci.*, 16(2):82 – 90, 2012.

[39] D. Van Thourhout and J. Roels. Optomechanical device actuation through the optical gradient force. *Nat. Photonics*, 4(4):211–217, Apr 2010.

[40] J. Roels, I. De Vlaminck, L. Lagae, B. Maes, D. Van Thourhout, and R. Baets. Tunable optical forces between nanophotonic waveguides. *Nat. Nanotechnol.*, 4(8):510–513, Aug 2009.

[41] M. Li, W. H. Pernice, and H. X. Tang. Tunable bipolar optical interactions between guided lightwaves. *Nat. Photonics*, 3(8):464–468, Aug 2009.

[42] P. T. Rakich, M. A. Popovic, M. Soljacic, and E. P. Ippen. Trapping, corralling and spectral bonding of optical resonances through optically induced potentials. *Nat. Photonics*, 1(11):658–665, Nov 2007.

[43] M. L. Povinelli, M. Lončar, M. Ibanescu, E. J. Smythe, S. G. Johnson, F. Capasso, and J. D. Joannopoulos. Evanescent-wave bonding between optical waveguides. *Opt. Lett.*, 30(22):3042–3044, Nov 2005.

[44] R. Zhao, P. Tassin, T. Koschny, and C. M. Soukoulis. Optical forces in nanowire pairs and metamaterials. *Opt. Express*, 18(25):25665–25676, 2010.

[45] K. S. Novoselov, A. K. Geim, S. V. Morozov, D. Jiang, Y. Zhang, S. V. Dubonos, I. V. Grigorieva, and A. A. Firsov. Electric field effect in atomically thin carbon films. *Science*, 306(5696):666–669, 2004.

[46] A. K. Geim and K. S. Novoselov. The rise of graphene. *Nat. Mater.*, 6(3):183–191, Mar 2007.

[47] M. Jablan, M. Soljacic, and H. Buljan. Plasmons in graphene: Fundamental properties and potential applications. *Proc. IEEE*, 101(7):1689–1704, July 2013.

[48] T. Low and P. Avouris. Graphene plasmonics for terahertz to mid-infrared applications. *ACS Nano*, 8(2):1086–1101, 2014.

[49] P. Tassin, T. Koschny, and C. M. Soukoulis. Graphene for terahertz applications. *Science*, 341(6146):620–621, 2013.

[50] P. Tassin, T. Koschny, M. Kafesaki, and C. M. Soukoulis. A comparison of graphene, superconductors and metals as conductors for metamaterials and plasmonics. *Nat. Photonics*, 6(4):259–264, Apr 2012.

[51] Z. Fang, S. Thongrattanasiri, A. Schlather, Z. Liu, L. Ma, Y. Wang, P. M. Ajayan, P. Nordlander, N. J. Halas, and F. Javier G. de Abajo. Gated tunability and hybridization of localized plasmons in nanostructured graphene. *ACS Nano*, 7(3):2388–2395, 2013. PMID: 23390960.

[52] L. A. Falkovsky. Optical properties of graphene. *J. Phys.: Conf. Ser.*, 129(1):012004, 2008.

[53] W. Gao, J. Shu, C. Qiu, and Q. Xu. Excitation of plasmonic waves in graphene by guided-mode resonances. *ACS Nano*, 6(9):7806–7813, 2012.

[54] J. Stewart. *Calculus: concepts and contexts*. Brooks/Cole Cengage Learning, Belmont, CA, 2010.

[55] C. Lee, X. Wei, J. W. Kysar, and J. Hone. Measurement of the elastic properties and intrinsic strength of monolayer graphene. *Science*, 321(5887):385–388, 2008.

[56] A. Croy, D. Midtvedt, A. Isacsson, and J. M. Kinaret. Nonlinear damping in graphene resonators. *Phys. Rev. B*, 86:235435, Dec 2012.

[57] M. Eichenfield, R. Camacho, J. Chan, K. J. Vahala, and O. Painter. A picogram- and nanometre-scale photonic-crystal optomechanical cavity. *Nature*, 459(7246):550–555, May 2009.

[58] X. Song, M. Oksanen, J. Li, P. J. Hakonen, and M. A. Sillanpää. Graphene optomechanics realized at microwave frequencies. *Phys. Rev. Lett.*, 113:027404, Jul 2014.

[59] V. Singh, S. J. Bosman, B. H. Schneider, Y. M. Blanter, A. Castellanos-Gomez, and G. A. Steele. Optomechanical coupling between a multilayer graphene mechanical resonator and a superconducting microwave cavity. *Nat. Nanotechnol.*, 9(10):820–824, Oct 2014.

[60] S. Timoshenko and S. Woinowsky-Krieger. *Theory of plates and shells*. McGraw-Hill, 1959.

[61] Q. Lu, M. Arroyo, and R. Huang. Elastic bending modulus of monolayer graphene. *J. Phys. D: Appl. Phys.*, 42(10):102002, 2009.

[62] D. Sánchez-Portal, E. Artacho, J. M. Soler, A. Rubio, and P. Ordejón. *Ab initio* structural, elastic, and vibrational properties of carbon nanotubes. *Phys. Rev. B*, 59:12678–12688, May 1999.

[63] R. Nicklow, N. Wakabayashi, and H. G. Smith. Lattice dynamics of pyrolytic graphite. *Phys. Rev. B*, 5:4951–4962, Jun 1972.

[64] A. Fasolino, J. H. Los, and M. I. Katsnelson. Intrinsic ripples in graphene. *Nat. Mater.*, 6(11):858–861, Nov 2007.

[65] J. Atalaya, A. Isacsson, and J. M. Kinaret. Continuum elastic modeling of graphene resonators. *Nano Lett.*, 8(12):4196–4200, 2008.

[66] N. Lindahl, D. Midtvedt, J. Svensson, O. A. Nerushev, A. Isacsson, and E. B. Campbell. Determination of the bending rigidity of graphene via electrostatic actuation of buckled membranes. *Nano Lett.*, 12(7):3526–3531, 2012.

[67] J. Snyman. *Practical mathematical optimization : an introduction to basic optimization theory and classical and new gradient-based algorithms*. Springer, New York, 2005.

[68] S. Enk and G. Nienhuis. Spin and Orbital Angular Momentum of Photons. *Europhys. Lett.*, 25(7):497–501, 1994.

[69] S. M. Barnett. Rotation of Electromagnetic Fields and the Nature of Optical Angular Momentum. *J. Mod. Opt.*, 57(14-15):1339–1343, 2010.

[70] K. Y. Bliokh and F. Nori. Transverse spin of a surface polariton. *Phys. Rev. A - At. Mol. Opt. Phys.*, 85(6):1–5, 2012.

[71] P. C. Chaumet and A. Rahmani. Electromagnetic force and torque on magnetic and negative-index scatterers. *Opt. Express*, 17(4):2224, Feb 2009.

[72] S. B. Wang and C. T. Chan. Lateral optical force on chiral particles near a surface. *Nat. Commun.*, 5:1–8, Mar 2014.

[73] K. Y. Bliokh, A. Y. Bekshaev, and F. Nori. Extraordinary momentum and spin in evanescent waves. *Nat. Commun.*, 5:3300, Mar 2014.

[74] A. Hayat, J. Mueller, and F. Capasso. Lateral chirality-sorting optical forces. *Proc. Natl. Acad. Sci.*, 2015:201516704, 2015.

[75] J. Zhou, T. Koschny, and C. M. Soukoulis. Magnetic and electric excitations in split ring resonators. *Opt. Express*, 15(26):17881–17890, Dec 2007.

[76] A. Zangwill. *Modern Electrodynamics*. Cambridge University Press, 2012.

[77] L. Solymar and E. Shamonina. *Waves in Metamaterials*. Oxford University Press, 2014.

[78] H. Zhang, Q. Wang, N. Shen, R. Li, J. Chen, J. Ding, and H. Wang. Surface plasmon polaritons at interfaces associated with artificial composite materials. *J. Opt. Soc. Am. B*, 22(12):2686–2696, Dec 2005.

APPENDIX A. WEAK EXPRESSION

COMSOL Multiphysics is the commercial package used throughout the thesis work, based on the finite element method. The general process for COMSOL to work is as follows: First it discretizes the continuous domain into small grids. For example, in 2D triangular and rectangular are most commonly used, while in 3D tetrahedral is often taken for the discretization. Then the partial differential equation is transformed into the so-called weakform, and Galerkin's method in which the the original and the test function take the same basis functions is taken. The calculations are done on on a set of element matrix and are assembled into a big linear system. The weakform part is the key in using COMSOL. While COMSOL has offered a lot of built-in modules for common PDEs such as the Helmholtz equation, there are a lot of cases in the state-of-the-art researches that people cannot get what they want in the built-in modules. Thus, one can always focus on the physics model and develop his own weak expression for either the domain or the boundary constraint, but get released from the pure mathematical part of solving PDEs. In this Appendix, we show the derivations of weak expressions for a few photonic systems, such photonic crystals, plasmonics, etc.

Complex-k band for a 2D photonic crystal

Weak form is "weak" in comparison with the "strong" form. In general, a physics equation is a second order PDE, which has strong requirements on the continuity of the variables. By multiplying a test function and performing an integral, one can reduce the

order of the PDE by 1. The reduced form has a weaker continuity requirement and is more numerically preferred. That's why it is called a weak form. Below we show how the eigen-k is calculated in a 2D photonic crystal.

By Bloch theorem, the field function in a periodic photonic structure can be written as the product of a periodic function and a plane wave envelop function:

$$\vec{E}(\vec{r}) = u(\vec{r})e^{-i\vec{k}\cdot\vec{r}}\hat{E}, \qquad u(\vec{r}) = u(\vec{r}+\vec{a}). \tag{A.1}$$

And the weak expression for the TE wave(E field parallel to the rod axis) is:

$$\begin{aligned} 0 &= \int d\Omega[-\frac{k^2}{\mu}vu - \frac{iv}{\mu}\vec{k}\cdot\nabla u + \frac{iu}{\mu}(\nabla v)\cdot\vec{k} - (\nabla v)\cdot\frac{\nabla u}{\mu} + \frac{\epsilon\omega^2}{c^2}vu] \\ &= \int d\Omega \cdot W, \end{aligned} \tag{A.2}$$

where v is the test function of u. Since we only consider the in-plane (xy-plane) wave vector, there are three freedoms in the weak expression, k_x, k_y and ω. To calculate the eigenvalues of k_x, we need to prescribe the other two first. For the boundary, we apply the Floquet-periodic boundary conditions.

Port boundary constraint

Starting from the wave equation:

$$\nabla\times(\frac{1}{\mu}\nabla\times\vec{E}) - \frac{\epsilon\omega^2}{c^2}\vec{E} = 0. \tag{A.3}$$

Multiplied by a test function on both sides, and integrated over the whole domain, we have:

$$\int d\Omega[\nabla\times(\frac{1}{\mu}\nabla\times\vec{E})\cdot\vec{v} - \frac{\epsilon\omega^2}{c^2}\vec{E}\cdot\vec{v}] = 0. \tag{A.4}$$

The first term can be broken into two parts, and applying the divergence theorem:

$$\nabla\times(\frac{1}{\mu}\nabla\times\vec{E})\cdot\vec{v} = \nabla\cdot[(\frac{1}{\mu}\nabla\times\vec{E})\times\vec{v}] + (\frac{1}{\mu}\nabla\times\vec{E})\cdot(\nabla\times\vec{v}). \tag{A.5}$$

$$
\begin{aligned}
0 &= \int d\Omega \nabla \cdot [(\frac{1}{\mu}\nabla \times \vec{E}) \times \vec{v}] + \int d\Omega [(\frac{1}{\mu}\nabla \times \vec{E}) \cdot (\nabla \times \vec{v}) - \frac{\epsilon\omega^2}{c^2}\vec{E} \cdot \vec{v}] \\
&= \oint_{\partial\Omega} d\vec{\Gamma} \cdot [(\frac{1}{\mu}\nabla \times \vec{E}) \times \vec{v})] + \int d\Omega [(\frac{1}{\mu}\nabla \times \vec{E}) \cdot (\nabla \times \vec{v}) - \frac{\epsilon\omega^2}{c^2}\vec{E} \cdot \vec{v}] \\
&= \oint_{\partial\Omega} d\Gamma \cdot W_b + \int d\Omega \cdot W_d,
\end{aligned}
\tag{A.6}
$$

where W_d denotes the weak expression for the whole domain, and W_b means the weak expression for the boundary. In the 2D TE case, W_d and W_b are reduced to simpler forms:

$$
W_d = \frac{1}{\mu}(\partial_y E_z \cdot \partial_y v + \partial_x E_z \cdot \partial_x v) - \frac{\epsilon\omega^2}{c^2} E_z v, \tag{A.7}
$$

and

$$
\begin{aligned}
W_b &= \hat{n} \cdot [(\frac{1}{\mu}\nabla \times \vec{E}) \times \vec{v})] \\
&= \pm i\frac{\omega}{c} v H_y.
\end{aligned}
\tag{A.8}
$$

In our case, we should choose $\hat{n} = -\hat{x}$ at the incident side(left), and $\hat{n} = \hat{x}$ at the output side(right). By correctly defines the expression for H_y, we define a port. More details of the expression of a port can be found in Appendix B.

Modeling graphene as surface current sheet

Graphene is a two dimensional material, without well defined thickness. People sometimes like to use 0.34 nm which is is the average distance between two layers on graphite, as the thickness of graphene for modelling. In this way, one just needs to treat it as a regular bulk material in modelling and simulations. However, it brings complexities numerically. Due to the electronic properties, people are mostly interested in graphene from mid-infrared to visible ranges, which has a featured wavelength from a few micrometers to hundreds of nanometers. The extra small size of graphene makes the mesh (discretization of domains) very difficult. In addition, the experimentalists measures the surface conductivity, so another way is to treat graphene as current sheet, a boundary, where there is surface current flowing on it excited by the electric field present. The surface

current imposes discontinuity of parallel magnetic fields and is constraint by $\vec{J_s} = \sigma_s \vec{E}$, where σ_s is the surface conductivity. Starting from Eqn. (8) from the last section, we can get the weak expression to model graphene as:

$$\begin{aligned} W_s &= -j\omega[(\hat{n} \times \vec{H}) \cdot \vec{v}] \\ &= -j\omega \vec{J_s} \cdot \vec{v} \\ &= -j\omega \vec{E} \cdot \vec{v}, \end{aligned} \tag{A.9}$$

where $\vec{v}$ is the test function for electric fields.

APPENDIX B. ABSORBING BOUNDARY CONDITIONS OF BLOCH MODES

Orthogonality

This part is a supplementary derivation for Ref. [28]. Bloch modes are the eigen modes of a photonic crystals. It can be seen as the superposition of infinite planes waves with different wavenumber. Thus there is no definite "wavelength" for bloch modes and no built-in boundary conditions in COMSOL, such as scattering boundary conditions, perfectly matched layers, can be applied to absorb the Bloch modes. Here we show the principle how to develop self-defined port to absorb Bloch modes.

As we already showed that the weakform expression for the boundary is:

$$W_b = \vec{v} \cdot [\hat{n} \times (\frac{1}{\mu} \nabla \times \vec{E})] = \pm i \frac{\omega}{c} v H_y. \tag{B.1}$$

A port means it tells all information of the modes on the boundary, including the profile of each modes, and the proportion they take out of the whole field. The total field H_y can be written as follows:

$$H_y = h_0 + \sum_n c_n h_n = h_0 + \sum_n |n><n|H_y>, \tag{B.2}$$

where h_0 mean the source, and h_n or $|n>$ is the eigen-mode which hits the boundary. Thus the key of defining a port boundary to excite and absorb Bloch modes lies on the

definition of the orthogonality relation of Bloch modes.

Supposing a wave is propagating along z-direction, we have a set of equations as:

$$\begin{aligned} \partial_z \vec{E}_t + \frac{i\omega\mu}{c}\hat{z} \times \ \vec{H}_t &= \nabla_t E_z, \\ \hat{z} \cdot (\nabla_t \times \vec{H}_t) &= -\frac{i\omega}{c}\epsilon E z. \end{aligned} \tag{B.3}$$

Canceling out E_z, we can get:

$$\beta\vec{E}_t = -\frac{\omega}{c}\mu\hat{z} \times \vec{H}_t + \nabla_t[\frac{c}{\omega\epsilon}\hat{z} \cdot (\nabla_t \times \vec{H}_t)]. \tag{B.4}$$

Similarly we also have:

$$\beta\vec{H}_t = \frac{\omega}{c}\epsilon\hat{z} \times \vec{E}_t - \nabla_t[\frac{c}{\omega\mu}\hat{z} \cdot (\nabla_t \times \vec{E}_t)], \tag{B.5}$$

then we have:

$$\begin{bmatrix} 0 & \frac{\omega}{c}\mu(\hat{z}\times \quad) + \frac{c}{\omega}\nabla_t[\frac{1}{\epsilon}\hat{z} \cdot (\nabla_t \times \quad)] \\ \frac{\omega}{c}\epsilon(\hat{z}\times \quad) - \frac{c}{\omega}\nabla_t[\frac{1}{\mu}\hat{z} \cdot (\nabla_t \times \quad)] & 0 \end{bmatrix} \begin{bmatrix} \vec{E}_t \\ \vec{H}_t \end{bmatrix} = \beta \begin{bmatrix} \vec{E}_t \\ \vec{H}_t \end{bmatrix}. \tag{B.6}$$

However it is not difficult to prove that the matrix on the leftmost side is not Hermitian. In order to get an Hermitian operator, a few transformations need to be made. We multiply $\hat{z}\times$ on both sides resulting in:

$$\hat{A}|\phi>= -i\frac{\partial}{\partial z}\hat{B}|\phi>, \tag{B.7}$$

where

$$\begin{aligned} \hat{A} &= \begin{bmatrix} \frac{\omega}{c}\epsilon - \frac{c}{\omega}\nabla_t \times \{\hat{z}[\frac{1}{\mu}\hat{z} \cdot (\nabla_t \times \quad)]\} & 0 \\ 0 & \frac{\omega}{c}\mu - \frac{c}{\omega}\nabla_t \times \{\hat{z}[\frac{1}{\epsilon}\hat{z} \cdot (\nabla_t \times \quad)]\} \end{bmatrix}, \\ \hat{B} &= \begin{bmatrix} 0 & -\hat{z}\times \\ \hat{z}\times & 0 \end{bmatrix}, \qquad |\phi>= \begin{bmatrix} \vec{E}_t \\ \vec{H}_t \end{bmatrix}, \end{aligned} \tag{B.8}$$

$\hat{A}$ and $\hat{B}$ are Hermitian when ϵ and μ are real (lossless case).

For homogeneous waveguides with tranlational invarience along the propagation direction (z-direction), it becomes:

$$\hat{A}|\psi>=\beta\hat{B}|\psi>, \tag{B.9}$$

while for a periodic structure such as photonic crystals, it reads:

$$\hat{C}|\psi_0>=(\hat{A}+i\frac{\partial}{\partial z}\hat{B})|\psi_0>=\beta\hat{B}|\psi_0>, \tag{B.10}$$

where $\psi=\psi_0\mathrm{exp(i}\beta\mathrm{z)}$ and ψ_0 is a periodic function.

Generalized Hermitian eigenvalue problems

In either the case of homogeneous waveguides or photonic crystals , $\hat{A}$, $\hat{B}$ and $\hat{C}$ are all Hermitian operators. Thus the problem is reduced to a generalized Hermitian eigenvalue equation. Take $\hat{A}|\psi>=\beta\hat{B}|\psi>$ for example,

$$<\psi|\hat{B}|\psi>=2\hat{z}\cdot\int \mathrm{Re}[\tilde{\mathrm{E}}_\mathrm{t}\times\tilde{\mathrm{H}}_\mathrm{t}^*], \tag{B.11}$$

which does not guarrentee a positive definite value. This results in some departures from a regular quantum mechanical eigenvalue problem. Derivations are shown below by taking a standard process. Considering $|i>$ and β_i as eigenvectors and eigenvalues respectively,

$$\hat{A}|i>=\beta_i\hat{B}|i>, \tag{B.12}$$

and take Hermitian conjugate,

$$<j|\hat{A}^\dagger=\beta_j^*<j|\hat{B}^\dagger. \tag{B.13}$$

Multiplying $<j|$ and $|i>$ on each, and doing the substraction, and applying that both $\hat{A}$ and $\hat{B}$ are Hermitian, there is:

$$<j|\hat{A}|i>-<j|\hat{A}^\dagger|i>=\beta_i<j|\hat{B}|i>-\beta_j^*<j|\hat{B}^\dagger|i>. \tag{B.14}$$

$$0 = (\beta_i - \beta_j^*) < j|\hat{B}|i >, \tag{B.15}$$

Therefore, even $\hat{B}$ is not positive definite, as long as $< i|\hat{B}|i > \neq 0$, the eigenvalue β still needs to be real-valued, which is the same as regular quantum mechanics. However in the case that $< i|\hat{B}|i >= 0$, β could be complex, and β and β^* always appear in pair mathematically. They correspond to evanescent waves and a blowing-up counterpart.

In addition, in non-degenerate cases where $\beta_i \neq \beta_j^*$ for $i \neq j$, we have the orthonomal relation $< j|\hat{B}|i >= 0$.

APPENDIX C. ANALYTICAL DERIVATIONS FOR SPP ON DOUBLE GRAPHENE SHEETS

Eigen-modes

Assuming the TM surface mode propagates along the x-direction, and decaying into the z-direction, the magnetic field can be written as:

$$H_z = \begin{cases} Ae^{-\kappa(y-a)}e^{ik_{\text{spp}}x} & \in I \\ [Be^{\kappa(y-a)} + Ce^{-\kappa(y+a)}]e^{ik_{\text{spp}}x} & \in II \\ De^{\kappa(y+a)}e^{ik_{\text{spp}}x} & \in III \end{cases}, \tag{C.1}$$

and the electric field can be derived from the magnetic as:

$$\begin{cases} Ex &= -\frac{1}{i\omega\epsilon_0}\partial_y H_z \\ Ey &= \frac{1}{i\omega\epsilon_0}\partial_x Hz \end{cases}, \tag{C.2}$$

Together with the continuity conditions across the boundaries:

$$\begin{aligned} \hat{n} \times (\vec{H}_2 - \vec{H}_1) &= \vec{J}_s = \sigma_s \vec{E}, \\ \hat{n} \times (\vec{E}_2 - \vec{E}_1) &= 0 \end{aligned} \tag{C.3}$$

where σ_s is the surface conductivity density of graphene which can either be determined by the Kubo formula from single electron approximation, or measured experimentally. We then get a set of four equations:

$$\begin{bmatrix} 1-\frac{\sigma_s\kappa}{i\epsilon_0\omega} & -1 & -1 & -e^{-2\kappa a} \\ 0 & -e^{-2\kappa a} & -1 & 1-\frac{\sigma_s\kappa}{i\epsilon_0\omega} \\ 1 & 1 & -e^{-2\kappa a} & 0 \\ 0 & e^{-2\kappa a} & -1 & -1=0 \end{bmatrix} \begin{bmatrix} A \\ B \\ C \\ D \end{bmatrix} = 0, \tag{C.4}$$

Thus for a non-zero solution to exist, the determinant of the coefficient matrix should be zero, yielding the dispersion relation:

$$\pm\, e^{-2\kappa a} - 1 = -\frac{2i\omega\epsilon_0}{\kappa\sigma_s}, \tag{C.5}$$

and a constraint between the field amplitude:

$$\begin{aligned} A &= -\frac{2i\omega\epsilon_0}{\kappa\sigma_s}, \\ B &== -\frac{2i\omega\epsilon_0}{\kappa\sigma_s}C, \\ C &= \pm B, \end{aligned} \tag{C.6}$$

where a '+' sign denotes the mode with anti-symmetric currents (symmetric magnetic fields), and '-' sign denotes the mode with symmetric currents (anti-symmetric magnetic fields).

'+' mode: B=C, A=D

Force

The time averaged force in terms of the Maxwell stress tensor reads:

$$\begin{aligned} < F_i > &= \oint < T_{ij} > dA_j, \\ < T_{ij} > &= \frac{1}{2}\mathrm{Re}[\epsilon_0(E_i^* E_j - \frac{1}{2}\delta_{ij}E^2) + \mu_0(H_i^* H_j - \frac{1}{2}\delta_{ij}H^2)], \end{aligned} \tag{C.7}$$

In the lossless case, $< F_y >= \oint < T_{yy} > dxdz$.

In area I and III, $< T_{yy} >=0$.

In area II,

$$< T_{yy} >= \frac{1}{4}\mathrm{Re}[\epsilon_0|E_y|^2 - \epsilon_0|E_x|^2 - \mu_0|H_z|^2]. \tag{C.8}$$

By substituting the field expression in the Eigen-modes section, we get:

$$< T_{yy} >= \frac{\kappa^2}{\omega^2\epsilon_0}|B|^2 e^{-2\kappa a}. \tag{C.9}$$

Poynting vector

In order to normalized the total force by power, we calculate the poynting vector:

$$< S_x >= \frac{1}{2}\mathrm{Re}(E_y^* H_z) = \frac{1}{2}\frac{k_{\mathrm{spp}}}{\omega\epsilon_0}|H_z|^2. \tag{C.10}$$

In area I, $H_z = Ae^{-\kappa(y-a)}e^{ik_{\mathrm{spp}}x}$, so

$$\begin{aligned}\int_a^\infty < S_x > dy &= \int_a^\infty |A|^2 e^{-2\kappa(y-a)}\frac{1}{2}\frac{k_{\mathrm{spp}}}{\omega\epsilon_0}dy, \\ &= \frac{k_{\mathrm{spp}}}{\omega\epsilon_0\kappa^3\eta}|B|^2,\end{aligned} \tag{C.11}$$

where $\eta = \sigma_s/i\omega\epsilon_0$.

In area II, $H_z = Be^{ik_{\mathrm{spp}}x}e^{-\kappa a}[e^{\kappa y} + e^{-\kappa y}]$, so

$$\begin{aligned}\int_{-a}^a < S_x > dy &= \frac{1}{2}\frac{k_{\mathrm{spp}}e^{-2\kappa a}}{\omega\epsilon_0}|B|^2\int_{-a}^a (2 + e^{2\kappa y} + e^{-2\kappa y})dy \\ &= \frac{k_{\mathrm{spp}}}{\omega\epsilon_0}|B|^2[2ae^{-2\kappa a} + \frac{1 - e^{-4\kappa a}}{2\kappa}].\end{aligned} \tag{C.12}$$

In area III, $H_z = De^{\kappa(y+a)}e^{ik_{\mathrm{spp}}x}$, then

$$\begin{aligned}\int_{-\infty}^{-a} < S_x > dy &= \int_{-\infty}^{-a} |D|^2 e^{2\kappa(y+a)}\frac{1}{2}\frac{k_{\mathrm{spp}}}{\omega\epsilon_0}dy \\ &= \frac{k_{\mathrm{spp}}}{\omega\epsilon_0\kappa^3\eta}|B|^2.\end{aligned} \tag{C.13}$$

Adding all these up we can get the total power flowing along the x-direction:

$$\int_{-\infty}^{\infty} < S_x > dy = \frac{2k_{\mathrm{spp}}}{\omega\epsilon_0}|B|^2[\frac{1}{\kappa^2\eta} + ae^{-2\kappa a}]. \tag{C.14}$$

Normalized force

The total force normalized by the power read:

$$\begin{aligned} f_y &= \frac{d^2}{dxdz} < F_y >= -\frac{\kappa^2}{\omega^2\epsilon_0}|B|^2 e^{-2\kappa a}, \\ p_x &= \int < S_x > dy = \frac{2k_{\text{spp}}}{\omega\epsilon_0}|B|^2[\frac{1}{\kappa^2\eta} + ae^{-2\kappa a}], \\ \frac{f_y}{p_x} &= -\frac{\kappa^2 e^{-2\kappa a}}{2k_{\text{spp}}\omega[\frac{1}{\kappa^2\eta} + ae^{-2\kappa a}]}. \end{aligned} \tag{C.15}$$

'-' mode: B=-C, A=-D

Derivations for the '-' mode is very similar to the '+' one. And I will just give a summary here:

$$\begin{aligned} f_y &= \frac{d^2}{dxdz} < F_y >= \frac{\kappa^2}{\omega^2\epsilon_0}|B|^2 e^{-2\kappa a}, \\ p_x &= \int < S_x > dy = \frac{2k_{\text{spp}}}{\omega\epsilon_0}|B|^2[\frac{1}{\kappa^2\eta} - ae^{-2\kappa a}], \\ \frac{f_y}{p_x} &= \frac{\kappa^2 e^{-2\kappa a}}{2k_{\text{spp}}\omega[\frac{1}{\kappa^2\eta} - ae^{-2\kappa a}]}. \end{aligned} \tag{C.16}$$

It is worth noting that the '+' mode represents the SPP with anti-symmetric current distribution (symmetric magnetic field distribution), yielding an attractive force between the two sheets, while the '-' mode represents the SPP with symmetric current distribution (anti-symmetric magnetic field distribution), yielding a repulsive force between the two sheets.

APPENDIX D. DEFORMATION OF GRAPHENE SHEETS

The problem of finding the deformation of graphene sheets can be treated as the problem of finding local minimum of mechanical energy under external field. Thus the total mechanical energy can be written as:

$$W[y(x)] = W_b[y(x)] + W_f[y(x)] + W_s[y(x)], \tag{D.1}$$

where W_b is the bending energy, W_f is the work done by the external field, and W_s is the in-plane stretch energy. They are all functional of the deformation y(x):

$$\begin{aligned} W_b[y(x)] &= \frac{1}{2}D\int ds\frac{y''^2}{(1+y'^2)^{-3}} \\ &= \frac{1}{2}D\int dx y''^2(1+y'^2)^{-5/2}, \\ W_f[y(x)] &= -\int f[y(x)](y-y_0)dx, \\ W_s[y(x)] &= \frac{1}{2}K\Delta L^2, \end{aligned} \tag{D.2}$$

where $f[y(x)]$ is the force density along the graphene which will be updated recurringly when deformation changes. The deformation function y(x) is expanded into sum of a few sine- and cosine-basis,

$$\begin{aligned} y(x) &= \sum_n a_n\zeta_n(x) \\ \zeta_n(x) &= \begin{cases} \cos(nkx) & n = 1,3,5... \\ \sin(nkx) & n = 2,4,6... \end{cases}. \end{aligned} \tag{D.3}$$

In our simulations, since the power of input energy is not too large and the graphene sheet only jumps to the second order mechanical state, only first four orders' bases are enough.

It is worth noting that W_s is a very large term, and under our input power, almost no in-plane stretch could happen. By simplifying our numerical process, we remove the W_s term but replaced by imposing a constraint, that the total length does not change. This approximation is good under small input power, but will fail if the force is too strong and obvious in-plane deformation happens. The constraint could be written as:

$$Z(a_n) = \int ds - L_0 = \int dx(1 + y'^2)^{-\frac{1}{2}} - L_0 = 0. \tag{D.4}$$

By applying a Lagrangian multiplier, the final functional to be optimized becomes:

$$F(a_n, \lambda) = W_b(a_n) + W_f(a_n) - \lambda Z(a_n), \tag{D.5}$$

and:

$$\begin{cases} \frac{\partial F}{\partial a_n} & = 0 \\ \frac{\partial F}{\partial \lambda} & = 0 \end{cases}. \tag{D.6}$$

a_n can be updated iteratively by:

$$a_n^{i+1} = a_n^i + \delta \cdot [W'(a_n^i) - \lambda'(a_n^i)], \tag{D.7}$$

where δ is the step we choose for each iteration. A positive number will lead the optimization to a local maximum while a negative one lead to a local minimum.